Structural Health Monitoring of Composite Marine Propellers using Embedded Piezoelectric Sensors

Huijer, A.J.

DOI
10.4233/uuid:9c2c21d3-f80d-4aa4-9e06-39b4b5a11b32

Publication date
2025

Document Version
Final published version

Citation (APA)
Huijer, A. J. (2025). *Structural Health Monitoring of Composite Marine Propellers using Embedded Piezoelectric Sensors*. [Dissertation (TU Delft), Delft University of Technology]. https://doi.org/10.4233/uuid:9c2c21d3-f80d-4aa4-9e06-39b4b5a11b32

Structural health monitoring of composite marine propellers using embedded piezoelectric sensors

Arnaud Jan Huijer

Structural Health Monitoring

of Composite Marine Propellers

using Embedded Piezoelectric Sensors

Dissertation

For the purpose of obtaining the degree of doctor

at Delft University of Technology

by the authority of the Rector Magnificus prof.dr.ir. T.H.J.J. van der Hagen

chair of the Board of Directors

to be defended publicly on

Wednesday 19th of March 2025 at 10:00 o'clock

by

Arnaud Jan HUIJER

Master of Science in Maritime Technology

Delft University of Technology, the Netherlands

born in Hendrik-Ido-Ambacht, the Netherlands

This dissertation has been approved by the promotors.

Composition of the doctoral committee:

Rector Magnificus, chairperson

Prof. dr. C. Kassapoglou	Delft University of Technology, *promotor*
Dr. L. Pahlavan	Delft University of Technology, *promotor*

Independent members:

Prof. dr. P. Steeneken	Delft University of Technology
Prof. dr. ir. T. van Terwisga	Delft University of Technology
Prof. dr. Z. Sharif Khodaei	Imperial College London
Prof. dr. Z. Gürdal	University of South Carolina
S. Paboeuf	Bureau Veritas

Reserve independent members:

Prof. dr. G. Weymouth	Delft University of Technology

Printed by Ridderprint, Alblassserdam

This research was funded by ECoProp Open Technology Programme (OTP), and has been made possible by financial contribution of the Netherlands Organisation for Scientific Research (NWO)

ECoProp OTP partners: Bureau Veritas, COMMIT, EMHA Noise & Vibration, MARIN, Oceanco, Solico Engineering, Wärtsilä.

Contents

SUMMARY

Society increasingly demands that ships become more sustainable and quieter, given their significant share of global fuel consumption and green-house gas emissions. Fiber-reinforced composite marine propellers can contribute meaningfully to these goals. As a promising alternative to the conventional rigid metallic propellers, flexible composite propellers can offer improved underwater radiated noise (URN) and propulsion efficiency. Furthermore, manufacturing propellers from fibre-reinforced composite materials makes them lighter and reduces their electromagnetic signature.

Despite the significant potential of composite propellers for marine propulsion systems, uncertainties in their fatigue behaviour have so far hindered their wide-spread adoption. These uncertainties can arise from imperfections during the manufacturing process, operational conditions different than the ones considered in the design, coating deterioration leading to water ingress, impact events, and more. Such factors can have significant impact on the lifetime of the propeller, which is typically expected to endure billions of cycles. Structural health monitoring (SHM) has the potential to mitigate this issue by real-time recording and assessing the structural response and integrity of the propeller. Such an SHM system should neither affect the propeller performance nor its load-bearing capacity. In addition to providing insights into the current structural integrity of the propeller, an SHM system may also enable enhanced estimation of the remaining lifetime, thereby minimizing the risk of unexpected failures and downtime.

This thesis investigates the feasibility of developing composite marine propellers with an embedded SHM system based on piezoelectric sensors. These sensors are capable of performing strain monitoring (with application in load/response estimation) and acoustic emission monitoring (with application in damage identification). Three main topics have been studied; (i) the feasibility of measuring dynamic strains in the propeller blade using the embedded sensors, (ii) the effect of embedding piezoelectric sensors on the structural integrity, and (iii) the feasibility of measuring and assessing damage-induced acoustic emissions using the embedded sensors. An analysis framework has been proposed for the identification, classification, and localisation of acoustic emissions in thick composite structures.

Considering a glass-epoxy marine propeller blade as case study, it was found from experiments and numerical simulations that the dynamic strains can be measured in more than 92% of the blade area by the embedded piezoelectric sensors, from the first to the fifth blade passing frequency. In this investigation, the numerical simulations provided insights into the expected range of mechanical strains in the design conditions of the blade, while the coupon experiments provided insights into the measurable range of amplitudes and frequencies by the embedded sensors. The results suggest that the proposed SHM method is feasible.

Regarding the effect of embedding piezoelectric sensors on the structural integrity of the host specimen, four-point bending tests were performed on carbon-epoxy specimens with embedded piezoelectric sensors. The main finding was that stiffness and strength were affected to a very limited extent, however there was a stronger reduction in maximum strain and toughness. When embedding piezoelectric sensors, it is therefore recommended to not place them in critical areas.

Acoustic emissions (AE) were measured in the same four-point bending setup using the embedded piezoelectric sensors and surface-mounted sensors. The embedded sensors were generally able to measure damage-related AE up until near final failure. The AE signals from this test were clustered using a hierarchical method and correlated with the specimen type. The analysis based on reference surface-mounted AE sensors showed that one of AE clusters occurred only in specimens with embedded sensors and not in the specimens without sensor. This suggests that the damage behaviour in the composite may differ due to the presence of the embedded sensor.

A full-scale glass-epoxy marine propeller blade was manufactured with 24 embedded piezoelectric sensors. The manufacturing method was resin transfer molding. Nearly all the sensors survived the manufacturing process, with the exception of two. The feasibility of measuring AE throughout the blade using the embedded sensors was assessed. This was assessed by placement of the blade into a salt water tank. AE sources was simulated through standardized pencil lead breaks. The results indicated that the embedded sensors in the blade had a measurable range of around 216mm for a 90dB source signal with a noise level of 40dB, with a peak frequencies around 100kHz and 250kHz. Given that the noise during propulsion is expected to be of a similar order of magnitude in the frequency range of interest, i.e. hundreds of kHz, the proposed SHM approach is considered feasible.

Investigations were also conducted on damage-induced AE waveforms. In composite propeller blades, the AE waves typically propagate as multi-modal dispersive guided waves. This means that the waveform shape at the source and the receiving points may differ. Correction of the wave propagation effects can enhance the accuracy of the damage identification process. To address this, a back-propagation method with dispersion compensation was formulated. The method was assessed numerically and experimentally on a thick glass-vinyl ester panel. Satisfactory results were obtained for narrow-band AE signals. To identify the damage location in the blade, a source localisation method was developed as well, capable of dispersion compensation for multiple wave modes. Experiments were performed on the glass-vinyl ester panel using controlled AE sources with 200kHz and 300kHz centre frequencies. Analysis of the results revealed that the proposed multimodal localisation method can be an improvement over single-mode localisation, in the case that the measured signal has a comparable contribution of different wave modes. However, when a dominant wave mode in the signal is known a priori, the single-mode reconstruction approach can lead to better results.

To conclude, the research demonstrates the potential of using embedded piezoelectric sensors for SHM of composite marine propellers. The results provide various insights into both the opportunities and limitations of the developed methods. Recommended future research directions include further development of AE localisation and classification techniques, as well as conducting full-scale fatigue testing to assess the performance of the proposed methods at full scale prior to sea trials. The findings of this research are also believed to pave the way for data-driven estimation of the remaining lifetime of composite marine propeller blades.

SAMENVATTING

Er is een toenemende vraag vanuit de samenleving om schepen duurzamer en stiller te maken, gegeven hun significante bijdrage aan de opwarming van de aarde en de verslechtering van het onderwatermilieu. Het gebruik van vezelversterkte kunststof composieten scheepsschroeven kan een betekenisvolle oplossing zijn om deze problemen te verminderen. Ten opzichte van de stijve metalen scheepsschroeven die nu gebruikelijk zijn, wordt verwacht dat flexibele composieten scheepsschroeven een lager geluidsniveau hebben voor onderwater-verspreide ruis, alsook een beter brandstofverbruik. Andere voordelen voor composieten scheepsschroeven zijn het lagere gewicht en een kleinere elektromagnetische signatuur.

Ondanks deze voordelen is het gebruik van composieten scheepsschroeven niet wijdverspreid. Dit wordt geweten aan onzekerheden in het vermoeiingsgedrag van het gebruikte materiaal. Deze onzekerheden vinden hun oorzaak in imperfecties in het maakproces, omstandigheden tijdens het gebruik die niet meegenomen zijn tijdens het ontwerp, wateropname van het composiet door verlies van coating, impacts enzovoorts. Dergelijke factoren kunnen een relatief grote invloed hebben op de levensduur van de schroef, waarbij er vanuit wordt gegaan dat deze in de orde van miljarden cycli dient te zijn. Om beter inzicht te krijgen in de structurele integriteit van de scheepsschroef wordt *Structural health monitoring* (SHM) voorgesteld. Dit houdt in dat een systeem direct het mechanische gedrag en integriteit van de propeller beluistert en analyseert. Het SHM systeem dient geen effect te hebben op de hydrodynamische prestatie van de scheepsschroef, noch op de sterkte. Naast het verbeteren van de kennis over de huidige toestand van de scheepsschroef is er ook de mogelijkheid om het SHM systeem te gebruiken voor het inschatten van de resterende levensduur. Dit kan vervolgens het risico op onverwacht falen en uitval verminderen.

Dit proefschrift onderzoekt de haalbaarheid van de ontwikkeling van composieten scheepsschroeven met een ingebed SHM systeem op basis van piëzo-elektrische sensors. Deze sensors zijn in staat om zowel laagfrequente rekken te meten (voor inschatting van belasting en dynamische reactie van het schroefblad) alsook akoestische emissies (voor identificatie van schade). Drie thema's zijn onderzocht; (i) de haalbaarheid van het meten van dynamische rekken in het propellerblad door de ingebedde sensors, (ii) het effect van het inbedden van piëzo-elektrische sensors op de structurele integriteit, en (iii) de haalbaarheid van het meten en analyseren van schadegerelateerde akoestische emissies met behulp van de ingebedde sensors. Een framewerk is voorgesteld voor de identificatie, classificatie en bronlokalisatie van akoestische emissies in dikwandige composiet.

Bij een glasvezel-epoxy scheepsschroef als testcase is bevonden vanuit experimenten en simulatie dat dynamische rekken met betrekking tot de eerste tot en met vijfde bladpasseerfrequentie gemeten kunnen worden over meer dan 92% van het bladoppervlak met het gebruik van ingebedde piëzo-elektrische sensors. Hierbij gaf de simulatie inzicht in de amplitude van mechanische rekken in het blad onder gebruikelijke belasting terwijl de experimenten duidelijk maakten hoe gevoelig de ingebedde sensors waren voor rek bij verschillende frequenties. De resultaten bevestigen de haalbaarheid van deze toepassing van het SHM systeem.

Met betrekking tot de invloed van de ingebedde sensors op de structurele integriteit van het composiet zijn er vierpuntsbuigtesten uitgevoerd. Hierbij is een vergelijking gemaakt tussen koolstofvezel-epoxy proefstukken met en zonder ingebedde piëzo-elektrische sensor. De bevindingen geven aan dat in dit geval de stijfheid en sterkte nauwelijks verandert, hoewel er een sterkere afname is in maximale rek en taaiheid. Vanuit dit inzicht is het aan te raden om de piëzo-elektrische sensors niet in te bedden in kritieke regio's in het blad.

Tijdens de vierpuntsbuigtest zijn ook akoestische emissies (AE) gemeten door de ingebedde piëzo-elektrische sensors alsook door sensors gemonteerd op het proefstukoppervlak. Over het algemeen waren de ingebedde sensors in staat schadegerelateerde AE te meten tot aan het uiteindelijke falen van de proefstukken. De AE signalen uit deze test werden geclusterd met behulp van een hiërarchische methode en gecorreleerd aan het type proefstuk. Uit analyse van AE signalen van de sensors gemonteerd op het oppervlak bleek dat een specifiek AE cluster alleen voorkwam in proefstukken met ingebedde sensor, maar niet in de proefstukken zonder sensor. Dit impliceert een ander schadeverloop van het composiet in het geval van de aanwezigheid van een ingebedde sensor.

Hierna is een glasvezel-epoxy schroefblad op ware grootte geproduceerd met hierin 24 ingebedde piëzo-elektrische sensors. De productiemethode was vacuüminfusie. Op twee na overleefden alle sensors het productieproces. De haalbaarheid van het meten van schadegerelateerde akoestische emissies over het schroefbladoppervlak is onderzocht. Hierbij is het schroefblad in een zoutwatertank geplaatst en zijn AE bronnen gesimuleerd via het gestandaardiseerd breken van vulpotloodpunten. De resultaten stellen vast dat de ingebedde sensors een meetbereik hadden van ongeveer 216mm voor een AE signaal met een bronamplitude van 90dB, een ruisniveau van 40dB en piekfrequenties bij 100kHz en 250kHz. Met het uitgangspunt dat het ruisniveau tijdens het varen een vergelijkbare ordegrootte heeft (bij de doelfrequenties, i.e. honderden kHz), kan gezegd worden dat deze toepassing van SHM haalbaar is.

Algemener onderzoek is uitgevoerd over de golfvormen van schadegerelateerde AE. Met betrekking tot composieten scheepsschroeven kan gesteld worden dat AE golven zich voortbewegen in de vorm van multimodale geleide (elastische) golven. Dit houdt in dat de golf bij de bron er anders uitziet dan bij de sensorlocatie. Correctie van deze golfvoortbewegingseffecten kan de identificatie van schade verbeteren. Met dit doel is een achterwaartse voortbewegingsmethode geformuleerd door gebruik te maken van dispersiecompensatie. Deze methode is numeriek en experimenteel toegepast op een dikke glasvezel-vinylester composieten plaat. Voor relatief smalband AE signalen geeft dit adequate resultaten. Verder is voor lokalisatie van schade in het schroefblad een methode ontwikkeld die gebruik maakt die in staat is dispersiecompensatie uit te voeren voor meerdere modes van geleide golven. Hiervoor zijn experimenten uitgevoerd op de glasvezel-vinylester composieten plaat, gebruikmakend van gecontroleerde AE excitaties met een 200kHz en 300kHz middenfrequentie. Analyse van de resultaten geeft aan dat de multimodale lokalisatie een verbetering kan zijn op enkelmodale lokalisatie in het geval dat het gemeten AE signaal een gebalanceerde contributie heeft van de meerdere golfmodes. Daar staat tegenover dat wanneer er een dominante golfmode aanwezig is en deze a priori bekend is, de enkelmodale lokalisatie een beter resultaat geeft.

Ter conclusie kan gesteld worden dat het onderzoek een demonstratie geeft van de potenties van het gebruik van piëzo-elektrische sensors voor SHM toepassingen in composieten scheepsschroeven. De resultaten geven gevarieerde inzichten in zowel de mogelijkheden als beperkingen van de ontwikkelde methodes. Voorgestelde richtingen in het vervolgonderzoek zijn onder meer het verder ontwikkelen van AE lokalisatie- en classificatie- technieken, alsook het uitvoeren van vermoeiingstesten op schroefbladen in ware grootte ter vaststelling van de ontwikkelde methodes, voorafgaand op eventuele proefvaarten. De bevindingen van dit onderzoek zijn ook voorgesteld als voorbereiding voor data-gedreven inschatting van resterende levensduur van composieten scheepsschroeven.

1

INTRODUCTION

1.1 MOTIVATION

In recent years, there has been a growing interest in the maritime sector regarding the use of composite marine propellers. Composite propellers are made of fibre-reinforced plastic materials while propellers conventionally are made out of nickel-aluminium bronze alloys (Figure 1.1). Composite propellers can have various advantages over conventional propellers. They can improve ship propulsion efficiency by increasing the propeller diameter. The expected increase of underwater-radiated noise (URN) is mitigated by flexibility of the composite at the tip. This flexibility can locally reduce loading and subsequently, cavitation and URN [1–3]. Furthermore, composite propellers provide benefits such as reduced electromagnetic visibility and lower weight [4,5].

Figure 1.1: Marine propellers. (Left) a metal propeller with four blades [6]. *(Right) a glass-fibre epoxy composite propeller blade.*

Marine propeller blades are subject to fatigue, abrasion, and impact from particles in the water. As such, the material of the blades degrades over time. This degradation causes a finite lifetime, manifested by a drop in stiffness and strength. For composite marine propeller blades, there is less experience and knowledge in this behaviour than for marine propeller blades made from metals. To partly increase this knowledge, there have been, and currently are, research activities performed on understanding the fatigue behaviour of composite marine propellers [7–9] and hydrofoils [10,11]. These investigations have been performed with numerical simulations, coupon experiments, as well as large-scale fatigue experiments (Figure 1.2). Such investigations help in gaining preliminary knowledge about fatigue performance and to improve the design. However, when in operation, the propeller can experience a myriad of load cases and environments that were not accounted for beforehand or would be difficult to mimic in experiments. In this case, it would be beneficial to have a real-time structural health monitoring system. Note that for a composite marine propeller blade, the monitoring system would either be remotely-installed or embedded into the blade, as not to obstruct hydrodynamics of the blade.

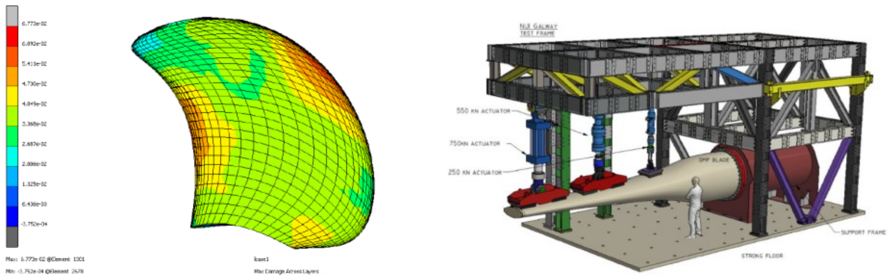

Figure 1.2: Assessment of fatigue in composite hydrofoils: (Left) a numerical simulation of fatigue of composite marine propeller blade, showing a damage parameter from 0-1 after 10^6 cycles [12]. *(Right) a large-scale fatigue setup of a composite hydrofoil* [11].

1.2 STRUCTURAL HEALTH MONITORING OF PROPELLERS

There have been recent research initiatives on the placement of monitoring systems in or surrounding composite marine propellers. Measurements of the structural response have so far primarily been performed in cavitation tunnel, for example by Maljaars et al. [5] (Section 3.7.) and Garg et al. [13]. A notable progress is the work of Maljaars et al. [14] wherein a full-scale propeller, driving a ship in calm water, was monitored using Digital Image Correlation (DIC) (Figure 1.3). However, open-water application of this method is hindered by the reduced visibility and increased scattering of light. Alternative measurement methods are highly desirable in this regard.

The layered nature of fibre-reinforced composite materials provides a unique opportunity to embed measurement devices such as Fibre-Bragg Gratings (FBG) and thin piezoelectric sensors [15–17]. Measurement of hydrodynamic loads, deformations, vibrations, and structural integrity with embedded sensors can lead to improvement in the design and assessment of future propellers, as well as in the maintenance of the in-service propeller.

Application of FBGs has shown promising outlook for strain and vibration measurement in composites. For embedding, FBGs are small in diameter and therefore their influence on the structural integrity of the host can be limited [18]. Seaver et al. [19] investigated measuring strains near the surface of a rotating carbon-fibre reinforced plastic composite (abbreviated as CFRP) marine propeller in a water tunnel using FBGs. On stationary blades, progress is shown for alloy marine propeller blades [20], composite aeronautic propeller blades [21] and composite wind turbine blades [22]. Tian et al. [23] placed strain gauges on marine propeller models and were able to retrieve dynamic strains through a data acquisition system (DAQ) integrated in the hub. Zetterlind et al. [21] compared their FBG results to readouts of strain gauges placed on the blade and noted broad agreement between the two methods. Ding et al. (2022) [24] measured strains on a model of a propeller blade using surface-mounted FBGs. Reconstructed deformations of the blade were created using an inverse finite element method. Error between reconstructions and deformation measurements was below 7%. Maung et al. (2017) [25] embedded distributed optical fibres into a carbon-fibre composite hydrofoil. It was noted that the measured strains were in reasonable accordance with simulations. This research was continued by Shamsuddoha et al. (2022) [10] who embedded distributed optical fibres into a full-scale composite hydrofoil loaded under fatigue. In that work, also piezoelectric accelerometers were placed to perform modal analysis. No notable change in modal properties was measured during the fatigue loading.

For more complex shapes, such as propeller blades, additional challenges with embedding optical fibres due to the large curvatures have been reported by Seaver et al. [26]. Also it is reported the directionality of FBGs might restrict guided wave capture [27]. With conventional strain gauges, the maximum recordable frequency is limited [28]. Piezoelectric sensors are a promising alternative. They can support a wider range of sampling frequencies [27], are less challenging to handle than optical fibres during the embedding process, and therefore are highly suitable for both dynamic strain measurement and ultrasonic-based structural health monitoring.

Song et al. [29] embedded piezoelectric sensors inside a scaled wind turbine blade. During a wind tunnel test and via a wireless DAQ, the attenuating effect of damage on guided waves was successfully detected. With thin piezoelectric polyvinylidene difluoride (PVDF) sensors, Sullivan and Mueller [30,31] measured aerodynamic pressures on an aluminium marine propeller and noted the need to correct the sensors for possible thermal effects in their application. Hamada et al. (2023) [32] placed piezoelectric line sensors on flexible propeller blades in operation. Degradation of the propeller blade was correlated with the changes in the vibration measured by the sensors.

On small-scale coupon specimens, dynamic strain measurements using piezoelectric sensors were performed by Shin et al. [33] and Lin et al. [34] on vibrating composite specimens. In their research, experimental results were compared to analytic models to reconstruct dynamic strains. Their approach to model sensor response relies on predetermined strains, which is also the case in the works of Gopalakrishnan et al. [35] and Erturk et al. [36], [37]. Ultrasonic elastic waves originating from fatigue damage have been passively recorded by Masmoudi et al. [38,39] in glass fibre specimens with piezoelectric sensors embedded inside. Multiple embedded sensors allow the localisation of damage, demonstrated by Dziendzikowski et al. [40], Yang et al. [41], Zamorano et al. [42] and Osmont et al. [43]. It should also be mentioned that piezoelectric sensors do not directly lend themselves for static strain measurement due to electrical discharge effects. Also, when embedding piezoelectric sensors, structural integrity of the composite is of concern since the sensor forms an inclusion between composite plies [38,40,41,44–51] or within plies [46–48,52], causing stress concentrations. In both glass-fibre reinforced plastics (GFRP) and CFRP specimens, the reported experimental results are case-specific due to variations in fibre lay-up, sensor geometry, insulation material (in the case of CFRP) and the type of loading applied. Therefore when other materials, lay-ups and loadings are considered, the effect on structural integrity is to be assessed.

Given the abovementioned advantages of piezoelectric wafer sensors in terms of embedding procedure and ability to measure at both low- and high-frequency regimes, they are believed to have great potential for application in composite marine propellers.

Figure 1.3: Deformation monitoring on a composite marine propeller blade in the GreenProp project. Digital Image Correlation is used, where a speckle pattern is added to the propeller blade, and cameras are mounted on the rudder. [14]

The measurement and analyses of quasi-static strains, as described in the methods above, are not capable of early-stage detection and localisation of early damage in the blade. Alternative methods have been proposed for early detection of damage. For composite materials, the use of active guided wave testing is broadly researched [53–55]. In this method, transducers emit ultrasonic mechanical pulses that are recorded by the same or other transducers. In post-processing, certain changes in recording are then related to the creation of damage. Note that active guided wave testing necessitates high-power equipment for excitation.

A method to passively measure ongoing degradation in materials, without the need for high-power equipment, is to record acoustic emissions. Acoustic emissions are small-amplitude, ultrasonic waves that emanate from the occurrence of material degradation [56]. They can be measured in the degradation of a multitude of materials and structures [57,58], including composites [59–61]. Here, a distinction can be made in the type of degradation and specifics of the acoustic emissions. Conventionally, these acoustic emissions are measured by piezoelectric sensors which may be integrated into composite materials. More elaborate descriptions of these methods, together with their strengths and limitations, are provided in chapters 2 to 5.

In this thesis, it is investigated how a structural health monitoring approach based on embedded piezoelectric sensors can be developed and assessed for the detection of degradation in composite marine propeller blades. This is motivated by posing the research questions that are introduced next section.

1.3 RESEARCH QUESTIONS

The main question is as follows:

How can a structural health monitoring system with embedded piezoelectric sensors be developed for composite marine propeller blades?

This is accompanied by a few sub-questions as listed below:

1. Is it feasible to embed piezoelectric sensors into composite marine propeller blades?
2. To what extent can acoustic emissions emanating from composite damage and dynamic strains be measured with the embedded piezoelectric sensors in a submerged composite marine propeller blade?
3. How do the embedded piezoelectric sensors influence the structural integrity of the composite marine propeller?
4. How can acoustic emissions emanating from damage in composite marine propeller blades be identified and localised?

1.4 ORGANISATION OF THE THESIS

The structure of the thesis is as follows: In this chapter, the motivation, research aim, and structure of the thesis were introduced. Chapter 2 investigates the feasibility of measuring acoustic emissions in small-scale coupon specimens using embedded piezoelectric sensors as well as the effect of the sensors embedment on the coupon structural integrity. Furthermore, the use of these sensors for the measurement of dynamic strains within a composite blade is evaluated. Chapter 2 therefore deals with research sub-questions 1,2, and 3. In Chapter 3 a data processing approach for distinguishing different sources of acoustic emissions is provided and assessed using composite coupon specimens with embedded piezoelectric sensors. Chapter 3 accordingly provides insights regarding research sub-questions 2, 3, and 4. Chapter 4 explains the manufacture and testing of a full-scale composite marine propeller blade with embedded piezoelectric sensors. This includes the measurement of acoustic emissions throughout the blade using the embedded piezoelectric sensors. Chapter 4 concerns research sub-questions 1 and 2. In Chapter 5, it is described how methodologies for acoustic emission signal reconstruction and localisation can be adapted and applied to thick composite structures for use in composite marine propeller blades. Chapter 5 hence relates to research sub-question 4. In Chapter 6, the thesis is concluded with a summary of main findings, and recommendations are given for the future research.

2

FEASIBILITY EVALUATION FOR DEVELOPMENT OF COMPOSITE PROPELLERS WITH EMBEDDED PIEZOELECTRIC SENSORS

This chapter is an adaptation of the journal paper titled "Feasibility Evaluation for Development of Composite Propellers with Embedded Piezoelectric Sensors" published in Marine Structures in 2022. The chapter provides details on initial investigations on measuring acoustic emissions and dynamic strains using embedded piezoelectric sensors. This chapter mostly contributes to answering research sub-questions one and three.

2.1 INTRODUCTION

This chapter aims to evaluate the feasibility of this concept with focus on measurement of strains and passive ultrasound. Here, the passive ultrasound measurement will be used to monitor the increase of damage. The dynamic strain measurements is to indicate increase in propeller vibration and underwater radiated noise. To the authors' knowledge, investigations with similar methods and application have not been published before. The ability of embedded piezoelectric sensors to measure dynamic strains acting on a real propeller blade is evaluated. The strain field is estimated from finite element simulation of a rotating composite marine propeller blade. An electro-mechanically-coupled model of the piezoelectric sensors has been constructed for translation of the input strain field to output voltage. Furthermore, coupon CFRP specimens with embedded piezoelectric sensors were designed and manufactured. These coupons are considered as the start of a step-by-step approach towards full-scale propeller assessment. The measured and modelled output voltage of the sensors are compared to load cell results and strain gauge results. To additionally evaluate the sensors effect on the composite structural integrity and to detect damage-related guided waves, the same specimens were subjected to four-point bending up to failure. The differences in flexural stiffness, strength, maximum strain and toughness of the specimens compared to specimens without sensors are presented. Also the amount and nature of damage-related guided waves recorded by the embedded sensor are compared to those recorded by surface-bonded piezoelectric sensors.

Regarding the organization of the chapter, section 2.2 covers the modelling of a composite marine propeller blade in operation. Section 2.3 includes piezoelectric sensor modelling. In section 2.4 the experiments related to the dynamic strain measurements, damage-related guided waves, and structural integrity assessment are described. Results of the experiments and simulations are presented and discussed in section 2.5. The chapter ends with conclusions and recommendations for the future work.

2.2 MODELLING DEFORMATION OF COMPOSITE MARINE PROPELLERS

The dynamic behaviour of a composite marine propeller is simulated based on Maljaars et al. [5]. The deformation and strain behaviour is considered prospective for a flexible marine propeller, irrespective of fibre material. First the propeller material and geometry are described, followed by the load case and the method to retrieve a strain field.

2.2.1 Propeller description

The composite marine propeller presented and considered in this chapter is a four-blade propeller with a diameter of 1m. The blades are of sandwich construction and a section is shown in Figure 2.1. Detailed specifics on the propeller blade may be found in Table 6.2. of the work of Maljaars [5].The blade faces on the pressure and suction sides are made of composite laminates, and the core between the blade laminates is a polymat/resin rich material. The blade laminate consists of one ply of woven GFRP fabric and multiple unidirectional (UD) GFRP laminae. The woven fabric protects the blade surface against impact loads. The load carrying laminae consist out of E-glass fibres with a 600 gm^{-2} specific mass, infused with epoxy resin. Average lamina thickness is 0.5mm. For the blade to attain a tapered thickness ply drops were introduced at regular intervals. It is considered that the strain behaviour of this propeller is representative for a typical flexible composite propeller blade, regardless of fibre material.

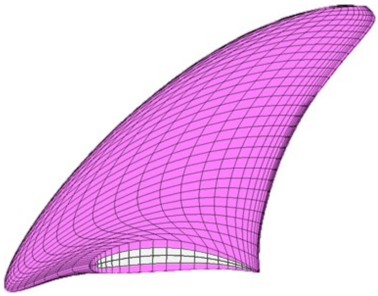

Figure 2.1: Cross-section of the composite marine propeller blade: blade faces (magenta) and core (white).

Elastic moduli E, Poisson ratios ν and shear moduli G of the isotropic core material, the woven GFRP fabric, and the UD GFRP lamina are listed in Table 2.1 [5]. The subscripts L, T and H in the elastic constants denote the longitudinal, the transverse and the thickness direction relative to the fibre direction, respectively.

Elastic properties	polymat/resin rich material	woven GFRP fabric	UD GFRP lamina
E_L, E_T, E_H [MPa]	4000	21584, 21584, 3500	34624, 5000, 3500
$\nu_{TL}, \nu_{LH}, \nu_{HT}$ [-]	0.3	0.192, 0.1, 0.1	0.0426, 0.1, 0.1
G_{TL}, G_{LH}, G_{HT} [MPa]	1538	3000, 2200, 2200	3100, 2200, 2200

Table 2.1: Elastic properties of the polymath/resin rich material, the woven GFRP fabric, and the UD GFRP lamina [5].

2.2.2 Propeller load case

A non-uniform wake field is considered. The wake field is based on the Nautilus diving support vessel sailing a straight path in calm water at 10.4 knots (5.35 m/s) [5]. The propeller experiences the wake field with a rotational speed of 600 rpm.

2.2.3 Discretisation and solving

A single blade is modelled using a finite element (FE) method with isotropic three-dimensional (3D) 20-node solid elements (type 21) for the core, and 3D 20-node composite brick elements (type 150) for the blade faces. The latter elements accommodate for the different fibre directions of the laminae and the varying amount of laminae. Marc/Mentat software was used for implementation of the model.

The different colours of the face element in Figure 2.2 represent the different zones of the blade laminate, due to the regular ply drops, with the layups proposed by Maljaars [5]. The layup can be described as symmetric and unbalanced and has main fibre directions of 20º, -15º,-60º,-105º with respect to the radial direction of the blade. For doubly curved composite structures, proper definition of material orientations is a key aspect in the modelling process [62]. A user-developed approach has been implemented to define the element-dependent (local) material orientations in the blade model (Figure 2.3): direction 3 is the normal to the element surface tangent plane, direction 2 is the intersection between the element surface tangent plane and the (global) x-y plane, and direction 1 is therefore defined as the outer product of directions 1 and 2. In the FE model, the fibre orientation is defined as the angle with respect to direction 2 [63].

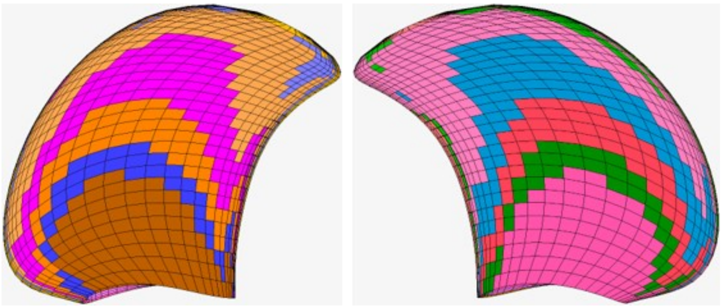

Figure 2.2:The solid FE model of the composite blade: pressure side (left), suction side (right). The colours indicate the different zones of the blade laminate because of ply drops.

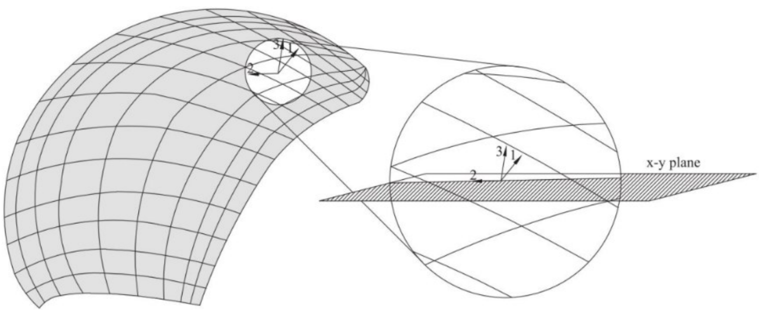

Figure 2.3: Defining material orientations. (Image taken from [5] *with permission of the author)*

For spatial discretization of the entire blade, a mesh density of 29×30×4 was applied. As shown in Figures 2.1 and 2.2, 29 elements were placed along the chord, 30 elements in radial direction, and 4 elements in through-thickness direction. In through-thickness direction, the outer elements represent the face sheets of the blade on pressure and suction side, while the inner two elements describe the core material. From the perspective of convergence it was shown that this mesh density can provide an accurate estimation [63]. Considering that the stiffness of the hub is much higher than the blade, the blade model is fully clamped at the blade-hub interface (Figure 2.4). Note that at this stage, no piezoelectric sensors are modelled into this discretization. Hence potential changes in local stiffness in the blade due to the embedded piezoelectric sensor are not taken into account.

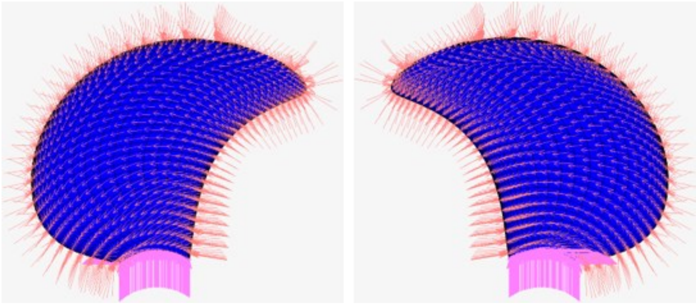

Figure 2.4: *The boundary condition and the loads: pressure side (left), suction side (right). The clamped boundary condition is given in pink, whereas the nodal loads are orange-coloured. The direction of the arrow implies the direction of the constraint and load. The length of the arrows is unitary and not related to load magnitude.*

For temporal discretization, a full revolution of the propeller in the non-uniform wake field is divided into 60 time steps, and the fluid pressures have been computed for each step. This computation contains a nonlinear hydro-elastic analysis that includes effects of potential flow, viscosity, centrifugal forces and hydrostatic pressure. Each pressure distribution snapshot was then transformed to nodal forces, and applied to the centroid of elements at blade faces (Figure 2.4). The resulting loads were employed in the FE analysis.

For every time step individually, a linear static analysis was performed. After solving, stresses were extracted for each ply at each time step. Using the stiffness matrix, these were converted to strains. The obtained strains were used in the feasibility analysis in the results. In Figure 2.5, the normal strains in the local axis system is shown for the 30th time step.

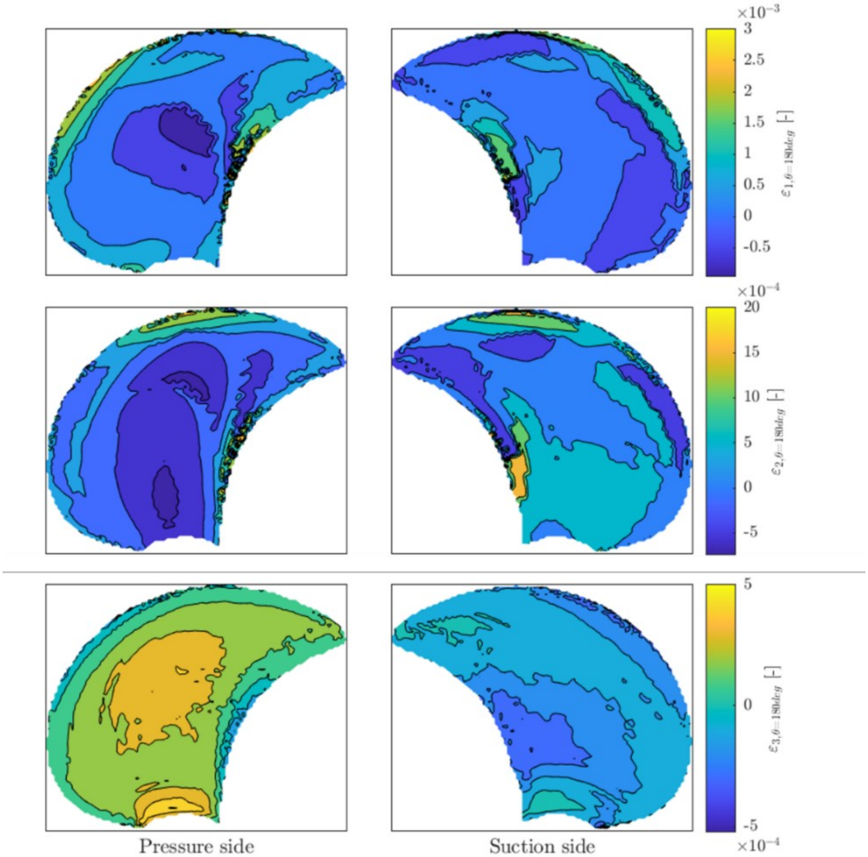

Figure 2.5: Normal strains in the local axis system for the 30th time step. The normal strains have the biggest contribution to the sensor voltage amplitude.

2.3 MODELLING PIEZOELECTRIC SENSOR BEHAVIOUR

The sensors considered in this research are piezoelectric wafers. In piezoelectric material, mechanical deformation of a crystal results in physical separation of positively-charged and negatively-charged parts. When a group of crystals are correctly structured, a macroscopic electric field is generated. Next to piezoelectric properties, the sensor material has elastic and dielectric properties as well. Taking these properties into account gives a set of constitutive equations, given in Equation 2.1 [64]. Note that temperature effects (pyroelectricity) are neglected here.

$$\boldsymbol{S} = \boldsymbol{s}^{\boldsymbol{E}}\boldsymbol{T} + \boldsymbol{dE}$$

$$\boldsymbol{D} = \boldsymbol{d}^{t}\boldsymbol{T} + \boldsymbol{\varepsilon E} \qquad (2.1)$$

Here, $\boldsymbol{s}^{\boldsymbol{E}}$ denotes the mechanical compliance matrix relating stress tensor $\boldsymbol{T}$ to strain tensor $\boldsymbol{S}$. Dielectric properties are represented by $\boldsymbol{\varepsilon}$, relating electric field intensity $\boldsymbol{E}$ to electric flux intensity $\boldsymbol{D}$. Piezoelectric behaviour is modeled by $\boldsymbol{d}$ and $\boldsymbol{d^t}$ relating electric field intensity to strain and stress to electric flux intensity respectively. Full tensors in Voigt notation are used in the calculation. Material properties of the considered piezoelectric material are given in Table 2.2.

The performance of the sensor can be represented by the circuit laid out in Figure 2.6 and obeys Kirchhoff's current law [36] given in Equation 2.2.

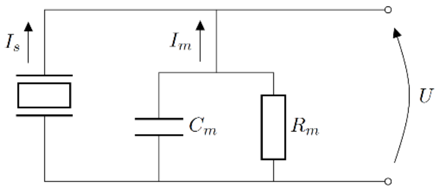

Figure 2.6: Circuit representation of a piezoelectric sensor with current I_s and measurement system with current I_m.

Elements of this circuit are the piezoelectric sensor (with current I_s, Equation 2.3), an external capacitator and an external resistor (I_m, Equation 2.4), all placed in parallel to each other. The latter two indicate capacitive and resistive effects originating from wiring and the measurement device.

$$\sum I = 0 \rightarrow I_s + I_m = 0 \tag{2.2}$$

$$I_s = \frac{d}{dt}\int \boldsymbol{D}\, d\boldsymbol{A} \rightarrow I_s = \frac{d}{dt}\int \left(\boldsymbol{d}^t \boldsymbol{s}^{E^{-1}}\boldsymbol{S} - \boldsymbol{d}^t \boldsymbol{s}^{E^{-1}}\boldsymbol{dE} + \boldsymbol{\varepsilon E}\right) d\boldsymbol{A} \tag{2.3}$$

$$I_m = \frac{U}{R_m} + C_m \frac{dU}{dt} \tag{2.4}$$

In Equation 2.3 electric flux density $\boldsymbol{D}$ is substituted by the piezoelectric constitutive relations from Equation 2.1. Electrode surface area is defined by $\boldsymbol{A}$, in the form of $[0\ 0\ A_{el}]$ and $\frac{d}{dt}$ represents differentiation with respect to time. Electric field intensity is related to voltage U, assuming a linear distribution over sensor thickness h, through $\boldsymbol{E} = [E_1\ E_2\ \ U/h]^t$ [35]. Electrical resistance and capacitance are denoted by R_m and C_m respectively. Solving the differential equation resulting from Equation 2.2, sensor voltage U can be recovered from a known strain field $\boldsymbol{S}$.

For low-frequency excitation, the terms dependent on a time derivative become relatively small compared to the resistance term. This leads to a leakage in voltage compared to the strain field amplitude and is known as electrical discharge [36,65]. In higher frequencies, electromechanical resonance occurs as well, which is linked to the integration of the strain field over the electrode area. With proper description of the strain field as a function of the driving voltage electromechanical resonance and antiresonance behaviour can be reproduced by the method presented [15].

name	d_{31}, d_{33}, d_{15} [$\times 10^{-9}$ C/m]	$s^E_{11}, s^E_{12}, s^E_{13}, s^E_{33}, s^E_{44=55}, s^E_{66}$ [$\times 10^{-12}$m^2/N]	$\varepsilon^T_{11,r}, \varepsilon^T_{33,r}$ [$\times 10^3$]
PZ27	-17,42.5,50.6	17, -6.6, -8.61, 23.2, 43.5, 47.1	1.8, 1.8

Table 2.2: Electromechanical, mechanical and electrical material properties of PZ27 piezoceramic. Taken from [66]. *Permittivity ε^T_r is relative to the permittivity of vacuum and determined at zero stress T. Subscript 1 relates to both in-plane directions, while subscript 3 refers to the out-of-plane direction.*

2.4 EXPERIMENTS

2.4.1 Manufacturing of test samples

It is anticipated that many future flexible marine propeller blades would be manufactured out of CFRP. Hence, twenty-five beam-shaped specimens were made out of this material. In twelve specimens, small sensors of 7mm diameter and 0.24mm thickness were embedded. Six specimens contained larger sensors, with a diameter and thickness of 20mm and 0.29mm. As a baseline, seven specimens did not host sensors. The number of specimens and sensor specifics are elaborated in Table 2.3. Views of the specimen and its manufacture are given in Figures 2.7 and 2.8 [67,68].

Amount of specimens	Specimen name	Sensor material	Sensor diameter [mm]	Sensor thickness [mm]
12	S	PZ-27	7	0.24
6	L	PZ-27	20	0.29
7	N	-	-	-

Table 2.3: Specifics of the test samples produced.

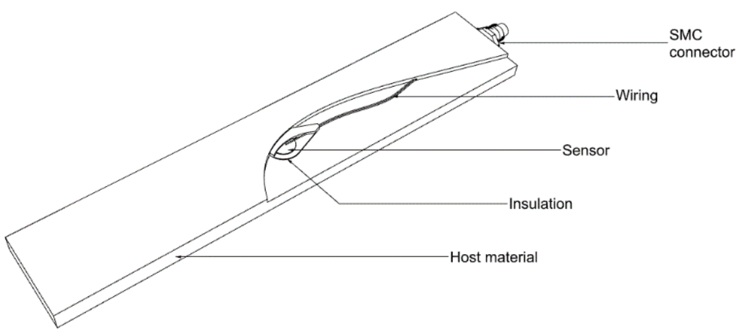

Figure 2.7: Cut-through drawing of the test sample, showing different components.

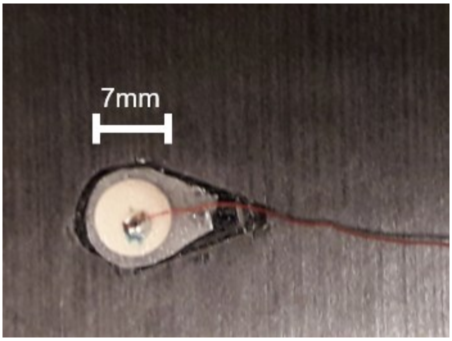

Figure 2.8: The embedding of piezoelectric sensor 4s. Note the drop-shaped cut-out in the CFRP and the lighter coloured glass fibre insulation [67].

The piezoelectric material used for the sensors were of the PZ-27 type, which has a depolarisation and maximum working temperature (350°C and 250°C) higher than the curing temperature of the host material (180°C) [66,69]. To achieve an omnidirectional sensitivity, the sensor was circular in shape. The thicknesses of 0.24mm and 0.29mm were chosen such that the host material would be affected minimally by the sensor's presence.

As the host material is electrically conductive, an insulation layer is applied between the piezoelectric sensor and the host. It is opted to use a thin layer of glass-fibre with epoxy resin (HexForce 00106 and Araldite LY 5052), following similar designs of [45,70]. The sensor was covered with insulation using a wet lay-up method, leading to a total thickness between 0.7mm and 1.2mm.

Bifilar enamelled copper wiring of 0.15mm diameter was used, connected to an SMC connector to link the sensor to the data acquisition system. The sensor, wiring and connector were embedded parallel to the plane of the host material layers. The connector was further insulated using thin Kapton tape.

The host material was an AS4/8552 carbon fibre epoxy resin prepreg, laid-up in a $[[0,90]_7,0]_s$ symmetric cross-ply sequence. Resulting specimen thickness was 5.4mm $\pm$ 0.1mm. From the 20th to the 25th layer, up to five drop shaped cut-outs were made to accommodate sensors. This thickness location was considered representative for a future propeller blade. The sensors would not be placed inside the uppermost or lowest plies as any stress concentrations could have a detrimental effect on failure. However, when placed at the neutral axis, the piezoelectric sensor would not be able to measure linear bending behaviour. Placing the sensors at ¾ of the laminate thickness, or between the 20th and 25th plies of the 30 plies in total, is considered a representative trade-off.

Plies were cut from a roll with 150mm width, giving square plates. The plates, with sensors and wiring embedded, were cured according to the manufacturers recommended procedure [69]. Afterwards, from these plates specimens were cut with a length of 150mm and a width of 27mm.

2.4.2 Description of experiments

Low-frequency strain measurements were performed by exciting the described specimens under four-point bending by means of a Zwick/Roell 1455 universal testing machine. Details of the set-up can be seen in Figure 2.9 and Figure 2.10. Piezoelectric sensor response, measured through a NI-USB6002 data acquisition system, was compared to the load measured by the testing machine itself, as well as by strain gauges (5mm gauge length and 120.2Ω resistance [71] connected to a Peekel Picas processing system) placed on the top and bottom of the specimens, at the location of the sensor. The load applied F_{LC} had a mean of 10.25N, an amplitude of 9.75N and was recorded using the load cell of the testing machine. The loading generated a strain amplitude in the same order of magnitude as anticipated inside a propeller blade. For each specimen, the load was applied with three crosshead velocities v_m: 10mm/min, 1mm/min and 0.1mm/min and with 20,20 and 5 cycles respectively. This approximately corresponds to 0.018Hz, 0.18Hz and 1.8Hz respectively and is used to define a lower bound for measurable frequencies. The sample rate for the piezoelectric sensor was 100Hz and no additional filters were applied.

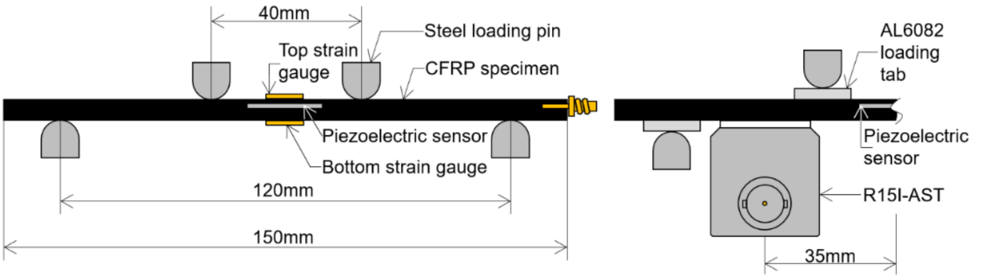

Figure 2.9: Details of the four-point bending set-up, showing specimen, piezoelectric sensor on the compression side, strain gauges on top and bottom of the specimen and the loading pins. The left Figure shows the set-up during low-frequency experiments, while the right Figure shows (half of) the additions made for the destructive tests.

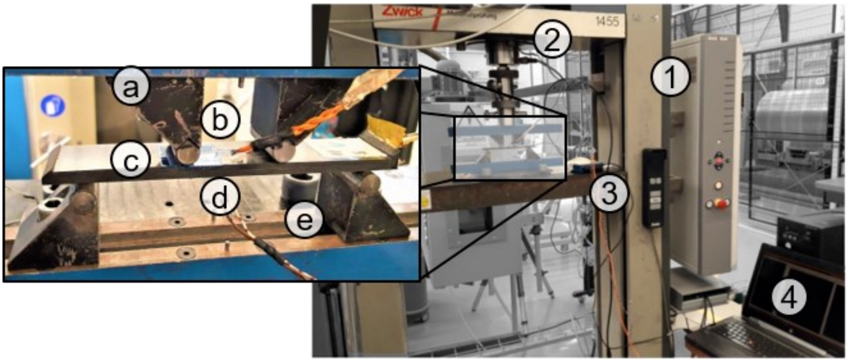

Figure 2.10: General arrangement of the specimen in the testing machine during low-frequency data acquisition. Numbers 1 to 4 mark the Zwick/Roell 1455 universal testing machine, load cell, NI-USB6002 data acquisition system and the measurement laptop respectively. Letters 'a' to 'e' denote respectively a loading pin, the upper strain gauge location, lower strain gauge location and a support pin.

To both measure damage-related acoustic emissions as well as to determine the influence of embedded sensors on flexural properties and mechanical strength of the specimen, the same bending set-up was used and the specimen was monotonically loaded up to failure (v_m=1mm/min). Failure was defined as the moment the reaction force at each reaction point is less than half the maximum force encountered. To prevent local transverse matrix cracking at the loading pins, which was expected through analytical formulations [72] given the material properties [69], AL6082 tabs of 15mm width and 3mm thickness were placed between the specimen and the loading pins (steel ø10mm). The piezoelectric sensor read-out was amplified by 40dB with a AEP5H preamplifier and connected to a Vallen AMSY6 data acquisition system. Furthermore, two commercial sensors, Mistras R15I-AST, were attached to the bottom side of the specimen, 35mm away from the centre of the specimen, to compare results, as shown in Figure 2.9. Signals were recorded when their amplitude exceeded a threshold set by the AMSY6 system. This threshold was set at 70dB for the embedded sensor and 35dB for the commercial sensors. Acquired signals were stored at a sampling rate of 10MHz and included a pre trigger and post duration time of 200μs and 100μs respectively. Signals were digitally filtered using a band pass filter to a domain of 20kHz to 960kHz. In total, four baseline specimens were tested, together with two specimens with small sensors embedded on the compression side of the specimen, two specimens with large sensors on the compression side and two specimens with small sensors on the tension side.

2.5 RESULTS

2.5.1 Feasibility of measuring dynamic strains on a propeller blade

As a case study the strains of a full propeller blade, derived in Section 2.2, were considered for the determining feasibility of measuring dynamic strains. The objective of this is to investigate to what extent the embedded sensors will be able to reliably measure vibrations in the blade due to blade-hull interactions and associated harmonics. This is relevant, as the propeller vibration can influence the hydrodynamic performance as well as the amount of underwater radiated noise.

The geometry and material properties of the piezoelectric sensor used in experiments (Section 2.4) were adopted. Using the theory of Section 2.3 and the material properties of the sensor manufacturer [66], voltage amplitude $U(f,\mathbf{x})$ at frequency f and location $\mathbf{x}$ was obtained. Location $\mathbf{x}$ is based on the lamina closest to the core for both pressure and suction side of the blade. Each nodal location $\mathbf{x}$ is treated as to contain a piezoelectric sensor, with the size and properties equal to the 'small' sensor in the experiments (Table 2.2, Table 2.3). Strains acting in the nodal location are then regarded uniform over the sensor area.

In order to assess the feasibility of measuring the dynamic strains, the amplitude of the voltage at a certain frequency is compared to a threshold amplitude, signifying a conservative value for the electromagnetic noise that may be encountered during operation.

A reference threshold amplitude U_{ref} is defined as 0.1V, based on Wheeler et al. [73]. In laboratory experiments using the blade that is also presented in Chapter 4, the noise level was considerably lower (Figure 5.4. of de Bles [74]). This suggests that this is a good starting value in setting up equipment and measurements. The threshold is subject to later updates as measurements from the field become available. A feasibility index for measuring dynamic strains is introduced as follows (Equation 2.5):

$$FI_f(f, \mathbf{x}) = \frac{|U(f, \mathbf{x})|}{|U_{\mathrm{ref}}|}. \tag{2.5}$$

Here, performing a measurement is considered feasible if $FI_f \geq 1$. This indicates the signal having an amplitude higher than the noise amplitude and represents a minimum required value. No upper limit in voltage amplitude is introduced since it is expected issues with high voltage measurements can be mitigated with a proper design of a data acquisition system.

Ten periods, or one second, were modelled using the midpoint method to solve Equation 2.2. A resistance of $R_m = 10^9\Omega$ was applied. No external capacitance C_m is applied. These values are representative for what was observed during the experiments described in Section 2.4. Resulting sensor voltages U for each location were evaluated for base frequency $f = 10$Hz (established by the 600rpm rotational speed) and its harmonics 20, 30, 40 to 50Hz by means of a fast Fourier transform. The harmonics are assessed to provide a full view of the measurability of dynamic strains experienced by the propeller blade. Figure 2.11 shows FI_f for the smaller sensor. For an overview of the coverage over the propeller blade, in Table 2.4 the percentage is given of evaluated area that passed the failure criterion $FI_f \geq 1$, as well as a mean value of FI_f.

f [Hz]	Small sensor coverage				Large sensor coverage			
	Pressure side		Suction side		Pressure side		Suction side	
	Area [%]	Mean FI_f [-]	Area [%]	Mean FI_f [-]	Area [%]	Mean FI_f [-]	Area [%]	Mean FI_f [-]
10	98.7	70.1	98.3	68.3	99.1	77.7	98.8	74.8
20	96.7	27.6	94.3	29.5	96.9	34.1	95.0	37.0
30	96.1	18.9	93.5	19.0	96.5	24.4	94.1	24.9
40	95.4	13.2	92.6	13.2	95.8	17.4	93.3	17.5
50	94.5	10.8	92.1	11.1	95.3	14.2	93.2	14.6

Table 2.4: Coverage of the feasibility criterion over the propeller blade in per cents, for two types of sensors

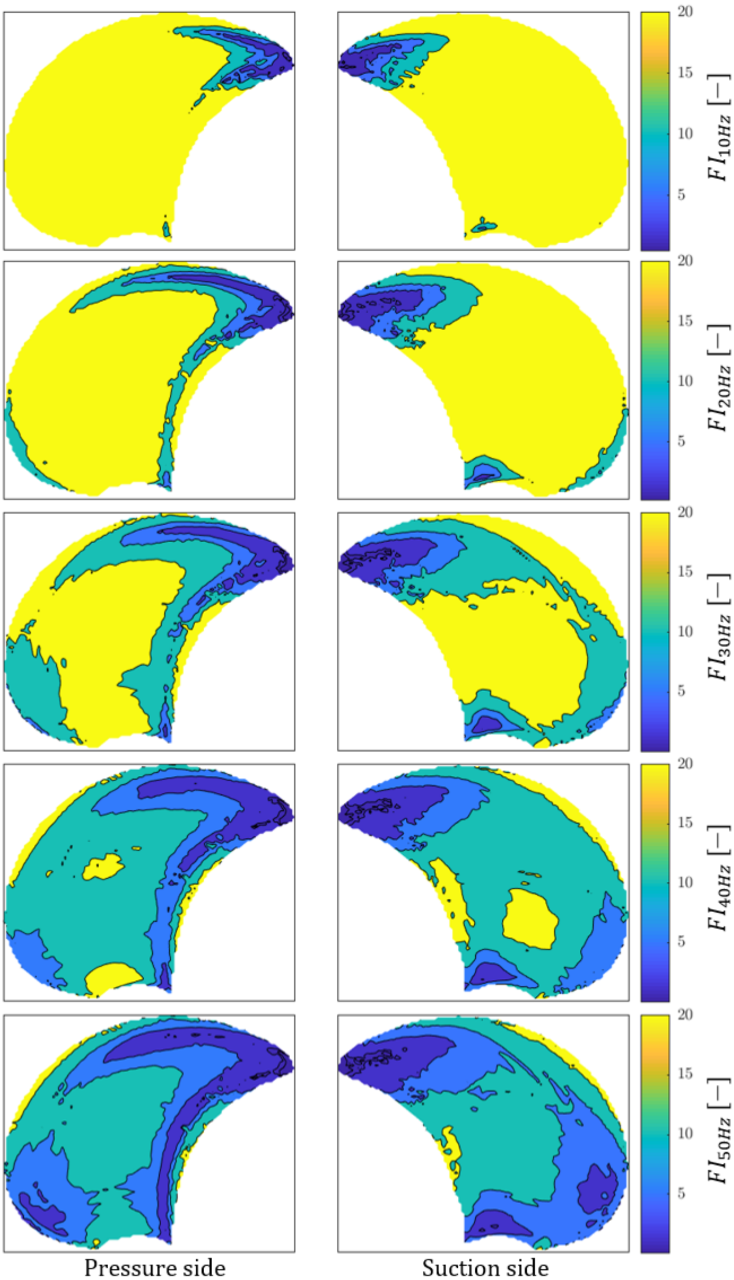

Figure 2.11: Feasibility index for the smaller sensor on both the pressure and suction side of the marine propeller from 10, 20, 30,40 to 50Hz from top to bottom. Note that the feasibility index is displayed from a value of one and is cut off at twenty.

The table shows that the base frequency is well captured, with a slight descend over the harmonics. The pressure side is better covered than the suction side, which can be attributed to higher strain magnitudes of the former respective to the latter. Analogous to the experimental observations, the larger sensor returns a higher coverage, which is due to the larger sensor thickness.

In Figure 2.11 it is visible that particularly the tip of the propeller has a low feasibility index. The dominant strain components, being in-plane normal strain S_{xx} and S_{yy}, in this region are not of notably low magnitude but they appear of opposite sign. This local behaviour of compression in one direction and expansion in the other direction counteracts the build-up of voltage in the sensor, resulting in a relatively low feasibility index. In this context, it is relevant to note that the piezoelectric material (Table 2.2) has in-plane isotropic electromechanical properties.

Altogether, at least 92% of the propeller blade allows for dynamic strain measurement up to the fourth harmonic with sufficient quality, given the sensors used in the experiment.

Note that in this investigation, a typical value for electrical noise is used for reference. Further effects of noise, and then mainly from underwater radiated noise (URN), are not taken into account. For the lower frequencies, the URN is associated with the blade passing motion. In that sense, the measurement of low-frequency strains is not expected to be hampered by the URN, as both URN and strains come predominantly from the same source. The URN shows a decreasing trend in amplitude (-6dB/octave) for higher frequencies [75]. At these higher frequencies, the noise is mostly related to cavitation implosion events. In theory, if measured, these URN events do not necessarily limit the measurement of damage-related acoustic emissions. This is under the premise that the waveform and localisation of the URN event is sufficiently distinct from those of damage-related acoustic emissions.

2.5.2 Experimental measurement of dynamic strains

To evaluate the capability of the manufactured embedded piezoelectric sensors to measure low-frequency dynamic strains, as well as to compare measurements to the modelling presented in Section 2.3, low-frequency strains measurements were performed as described in Section 2.4. Results are shown here.

Out of 18 embedded piezoelectric sensors, 10 were able to detect low-frequency strains (Table 2.6). Other sensors either were short-circuited or had a broken connection. The results for specimen 3L, in terms of applied force F_{LC}, strain gauge strain S_{SG} and piezoelectric sensor output voltage U_{PZT} are given in for v_m =10mm/min, 1mm/min and 0.1mm/min.

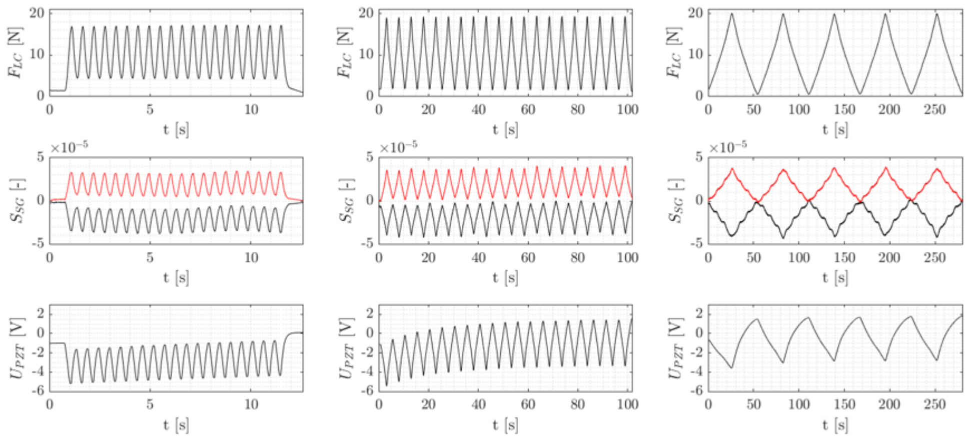

Figure 2.12: Applied force F_{LC}, strain gauge read-out strain S_{SG} and piezoelectric sensor voltage U_{PZT} for v_m =10mm/min, 1mm/min and 0.1mm/min from left to right. In the strain gauge results, the black line denotes the topside strain gauge (in compression) and the red line gives the bottom-side strain result.

A number of observations are made from Figure 2.12. Firstly, at higher crosshead velocities v_m = 10mm/min and 1mm/min, the applied load does not perfectly follow the imposed minimum and maximum of 0.5N and 20N. Secondly, the strain gauge results show instability, which is possibly due to the quarter Wheatstone bridge used [76]. Thirdly, with the piezoelectric sensor, the offset characterised by the other results decreases over time. Also, for v_m=0.1mm/min, the signal is more distorted and generally of a lower amplitude. These last three anomalies are related to electrical discharge, as described in Section 2.3.

To accurately compare sensors and results, the peak values (subscript $,a$) of the sensor voltage $U_{PZT,a}$ were divided by the peak values of the applied force $F_{LC,a}$ for each period. For a measure of comparison, the coefficient of variance is used. This is defined as the standard deviation of a dataset divided by its mean. When comparing results between different sensors, it turns out that for small sensors, the coefficient of variation of $U_{PZT,a}/F_{LC,a}$ for v_m=10mm/min, 1mm/min and 0.1mm/min is 25%, 21% and 42%. The corresponding coefficients of variation for large sensors are 14%, 14% and 19%, respectively. For analogy, the variation in specimen thickness alone would create a coefficient of variation of 1.6%, based on a quadratic relation between specimen thickness and $U_{PZT,a}/F_{LC,a}$. The seemingly-large coefficients of variation may firstly be attributed to local differences in embedding the sensor: Variation in the height location of the sensor, variation in glass-fibre insulation geometry and fibre-volume content and variation in cut-out size cause a variation in the strain field that is experience by the sensor. Secondly, variations in resistance and the small mean value of the output voltage at low velocities can be further sources of variation.

To simulate the strains encountered during the experiment, a 3D FEM model of a quarter of the specimen, including insulation, sensor and applied load was made in ANSYS [77]. Solid elements of type SOLID 186 and average length and thickness of 1mm and 0.18mm were used to model each lamina separately. To prevent skewing elements in thickness direction, all model thicknesses were chosen to match single or multiple lamina thicknesses. The small sensor was modelled with a thickness of one ply, whereas the large sensor had a two-ply thickness. The chosen thicknesses for the sensors closely approximate the values given in Table 2.3. The sensor was placed into five ply thicknesses of glass fibre. This corresponds to measured thicknesses from Section 2.4.1. The diameters of the small and large modelled sensors match exactly with the values in Table 2.3. Around the circumference of the sensor, the glass fibre insulation and a region of neat resin were modelled as elliptical in shape, each adding 1.5mm and 3mm in the width and length of the inset respectively. These dimensions may be compared to Figure 2.8. A view of the discretised model is given in Figure 2.13. The material properties were based on the data provided by Hexcel, Huntsman and Meggit [66,69,78,79] and are given in Table 2.5. The parameters related to the CFRP were updated to match the experimental results of the baseline specimens. More details on this approach may be found in Zhang et al. [77]. The Poisson's ratio and shear modulus of the GFRP were unknown and estimated. A load of 20N was distributed over the contact location of the top loading pins. The lower support pins were modeled as a boundary condition allowing no deflection in the out-of-plane and transverse directions. A linear static analysis was performed. Figure 2.14 shows the resulting strain in longitudinal direction (along the length of the specimen) for the larger sensor. Averaged over the sensor thickness and surface, values for the longitudinal strain were 16.5μm/m and 16.7μm/m for the small and large simulated sensor. Interpolating strain gauge measurements suggested a value of ≈20μm/m, which would be similar to the extreme value of what may be seen in Figure 2.14.

Elastic properties	CFRP AS4/8552 [69,77]	PZ 27 sensor [66,79]	GFRP insulation [78]	Neat resin [69,77]
E_L, E_T, E_H [GPa]	138.2, 9.8, 9.8	66, 66, 84	21, 21, 11.8	4.67
ν_{TL}, ν_{LH}, ν_{HT} [-]	0.35, 0.35, 0.4	0.389, 0.371, 0.371	0.17, 0.07, 0.07	0.35
G_{TL}, G_{LH}, G_{HT} [MPa]	4.1, 4.1, 1.96	41, 41, 41	3.5, 3.5, 3.5	1.73

Table 2.5: Elastic properties of the CFRP, sensor, insulation GFRP and neat resin, as used in the linear elastic modelling of the low-frequency experiment.

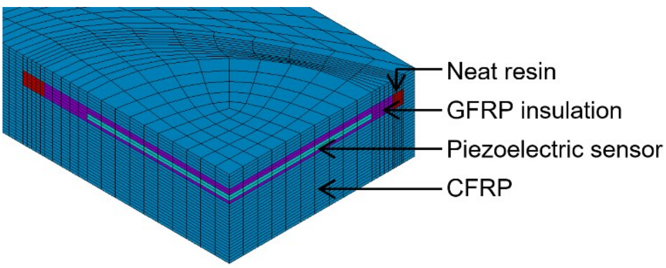

Figure 2.13: Discretisation of the sensor region for the larger embedded sensor. Note the circular shape of the sensor and the elliptical shapes of the glass insulation and neat resin.

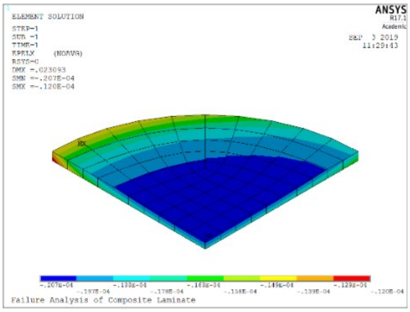

Figure 2.14: Strain in longitudinal direction for the larger sensor at a load of 20N on the specimen.

The strains obtained on the sensor elements were averaged over the sensor thickness and subsequently used as input for the theory of Section 2.3, wherein the true sensor thickness and the material properties of the manufacturer [66] were applied. Evaluation of Equation 2.2 gives a voltage signal dependent on the frequency of the applied load and resistance R_m in the system. Comparisons of experimentally-obtained $U_{PZT,a}/F_{LC,a}$ data to simulated results with R_m=$10^8\Omega$ and R_m=$10^{10}\Omega$ are shown in Figure 2.15 for the small and large sensor respectively. From the loading velocity v_m, representative frequencies are derived and shown on the logarithmic axis of Figure 2.15. Relative voltage amplitude $U_{PZT,a}/F_{LC,a}$ is shown in boxplots for these frequencies. For low frequencies and low resistance R_m, voltage amplitude becomes low. For higher frequencies and higher resistance R_m, voltage amplitude reaches a constant value. In the experimental boxplots and the simulated lines alike, increase and stabilisation behaviour in voltage amplitude over frequency may be seen.

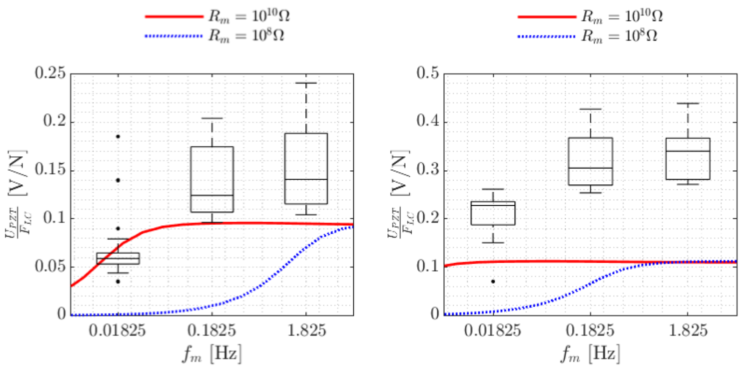

Figure 2.15: $U_{PZT,a}/F_{LC,a}$ of the experimental results in the boxplot, the simulation is given in red for R_m=$10^{10}\Omega$ and in blue for R_m=$10^{8}\Omega$.The left Figure shows the results for the small sensor, and the right Figure shows results for the large sensor.

The absolute voltage values from the simulation are 40% to 65% lower than the experimental values for the small and large sensors, respectively. It is considered that sources of variation can also be sources of this discrepancy. A discrepancy in material properties may occur between the experimental reality and the finite element model of the specimen. The material properties expected would be resin and glass fibre insulation stiffness and local CFRP stiffness. These discrepancies, in combination with differences in geometry of the cut-out and resin insulation and the height of the sensor location in the laminate may lead to an underestimation of the strains experienced by the sensor and will be the subject of further research.

2.5.3 Experimental measurement of damage-related guided waves

As described in Section 2.4, during failure testing, damage-related acoustic emissions were monitored by the embedded piezoelectric sensor in the specimen as well as by two attached R15I-AST sensors. With one specimen, the embedded piezoelectric sensor was able to record direct acoustic emissions, even up to the point of gross failure of the specimen. In Figure 2.16 one of the signals of a damage-related acoustic emission is given, which are measured by both the embedded piezoelectric sensor (3L, black) and the two commercial sensors (red and blue). In the Figure the voltages U are corrected for their pre-amplification.

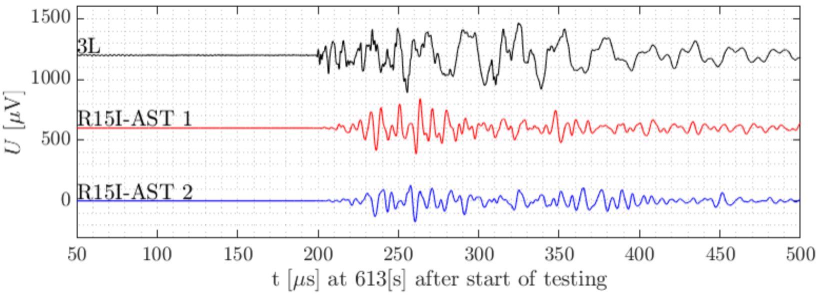

Figure 2.16: Acoustic emission signal captured by all three sensors at time t *=596s since the start of the test* [67].

From the bulk of recorded signals, a hit rate analysis is defined, where the amount of signals recorded per sensor was accumulated in a window five seconds before and after a one second timestep. To remove bias from burst-type noise, only hits were taken into account that were measured near-simultaneously (within 10 μs) by at least two sensors. Results are shown relative to the applied load F_{LC} and for signals that were recorded by either the embedded piezoelectric sensor and at least a single commercial sensor (Figure 2.17), or by at least the two commercial sensors. The hit rate of signals recorded by the embedded sensor is approximately an order of magnitude lower than the hit rate of the R15I-AST sensors. Nevertheless, it is visible that the trend in the rate of signals recorded by the embedded piezoelectric sensor is in line with that of the commercial sensors, up to around F_{LC}=7500N, after which the commercial sensors show a sudden increase in signals that is not covered by the embedded piezoelectric sensor. This might indicate a failure in the sensor or around the embedded sensor, blocking the propagation of elastic waves towards or through the sensor.

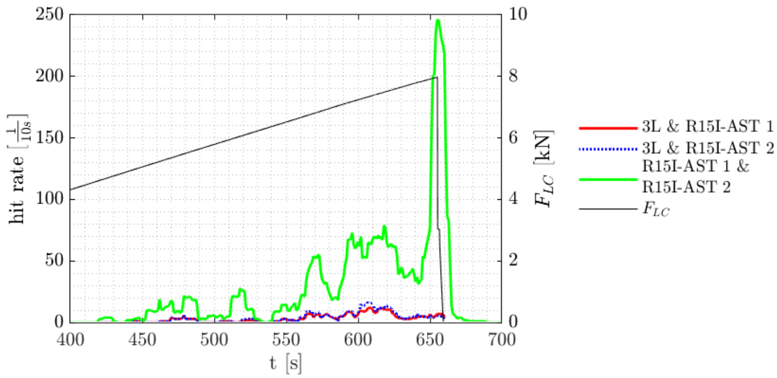

Figure 2.17: Hit rate of signals measured by the embedded piezoelectric sensor (3L) and a commercial sensor, and measured by both commercial sensors.

During the measurement of passive damage-related acoustic emissions, the transient signal is measured, as well as a pretrigger signal, being the reference signal acquired prior to the incoming of the acoustic emission. The signal to noise ratio SNR in dB, given in Equation 2.6, is used as feasibility index FI_{AE} for measuring acoustic emissions.

$$FI_{AE} = SNR = 10\log_{10}\frac{\sum_{t_{signal}} U^2}{\sum_{t_{pretrigger}} U^2} \tag{2.6}$$

To demonstrate feasibility in measuring acoustic emissions, a minimum value of 1dB is envisaged, based on comparable values from Horowitz et al. and Zhang et al. [80,81]. Figure 2.18 shows boxplots of the SNR for signals captured by embedded sensor 3L and by at least one of the commercial sensors. From these plots, it may be read the mean SNR of embedded sensor 3L is at 17dB, whereas the commercial sensors have a mean around 42dB for the same hits. Hits that were captured by the commercial sensor but not necessarily by 3L, show a mean SNR of 22dB. This may be attributed to the lower threshold given to the commercial sensor compared to the embedded sensor. It can be said the embedded piezoelectric sensor 3L is less sensitive than the commercial sensors. Nevertheless the SNR of the embedded piezoelectric sensor is considered sufficient, given the guideline of 1dB as described.

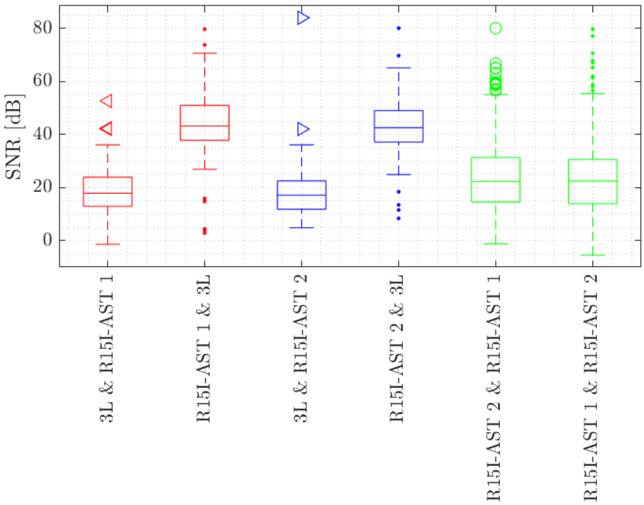

Figure 2.18: Boxplots showing the SNR values captured by either both embedded piezoelectric sensor 3L, in the first and third boxplots, and a commercial R15-AST sensor (second and fourth boxplot, red and blue for the two different commercial sensors) or by both commercial sensors, in green.

In a marine propeller in operation sources of ultrasonic elastic waves may not be limited to fatigue or failure related acoustic emissions. Cavitation implosion may create shock waves [82]. It is envisioned that readings from different source types have distinct waveform characteristics. In that situation, classification or clustering methods could be used to distinguish between cavitation-related ultrasonic waves and multiple types of damage-related acoustic emissions. These methods may use specific key parameters [39] or treat the waveform as a whole [67].

2.5.4 Influence of embedding sensors on structural integrity

In all specimens tested (Table 2.6), failure was first noticed between F_{LC} ≈6000N and 7000N at parts of the upper lamina, which was loaded in compression. Above F_{LC} ≈7000N, for baseline (N) specimens, the failure extended up to the four uppermost laminae and led to gross failure in one specimen. The other three baseline specimens experienced final tensile rupture, between 8mm and 21mm from the specimen centerline. Final tensile failure can be seen in the top photograph of Figure 2.19 [67].

For specimens with sensors embedded in the compressive side the failure in the compressive upper laminae continued towards the cut-out laminae, typically near the interface between the sensor and glass fibre insulation or more towards the centre of the sensor (Figure 2.19, middle picture).

Failure similar to the baseline specimens occurred for the specimens with sensors embedded on the tensile side, albeit 4.5mm to 8mm from the centerline. This corresponds to failure through the sensor or through the insulating glass fibre (Figure 2.19, bottom picture).

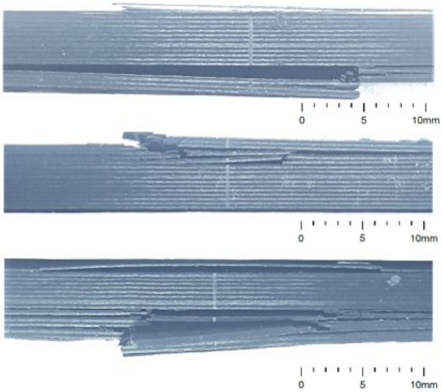

Figure 2.19: Failed specimens, from top to bottom: 4N, 2L, 5s(T) [68].

During the tests, both crosshead displacement w_m and load F_{LC} were monitored, giving the load-displacement data shown in Figure 2.20. Maximum load is also presented in Table 2.7. Based on these measurement data, specimen geometry and the procedure given by ASTM standard D6272[83], specimen flexural stiffness E, maximum strain S_{max}, strength T and toughness W values were retrieved, given in Table 2.7. What stands out is that, on average, the stiffness of specimens with embedded sensors is 8% lower than their baseline counterparts, with an average of 6.6% for small sensors and 11% for large sensors. Ultimate strain dropped on average 11% (20% in small sensors on compressive side, 3.3% for small sensors on tensile side and 9.3% in large sensors) whereas flexural strength remained largely similar. Taking the entire load-displacement history into account, toughness decreased on average 20% due to embedding a sensor, with a 34% drop for small sensors on the compressive side, 8.1% in small sensors on the tensile side and 19% for large sensors. From these values, it seems embedding a piezoelectric sensor in the tensile side of a specimen loaded in bending is less damaging than when placed in the compressive side. The size of the sensor appears to be of minor influence, when placed in the compressive side. However it should be noted that the variation in the data is relatively large and the sample size is relatively small, making it premature to reach a general conclusion on the matter.

In application to the composite propeller, this preliminary data may hint towards further consideration on the locations inside the blade for the embedded sensors to be placed in view of structurally critical areas.

Specimen	small sensor (12 total)													large sensor (6 total)							
	1S	2S	3S	4S	5S	6S	7S	8S	9S	10S	11S	12S	total	1L	2L	3L	4L	5L	6L	total	total
Low-frequency excitation	x	v	x	x	v	v	x	v	v	x	v	v	7	x	v	v	x	v	x	3	10
Elastic wave emission	x	v	v	v	v	v	x	v	v	x	v	v	9	x	v	v	x	v	x	3	12
Used in low-frequency test		v			v	v		v	v		v	v	7		v	v		v		3	10
Used for failure test		v		v	v				v				4		v	v				2	6

Table 2.6: Summary table of the measurement range and types of experiment performed by each specimen. Working is implied by 'v' while disfunction is denoted by 'x'. In total 25 specimens were made, 7 pristine, 12 with small sensor embedded and 6 with a large sensor embedded.

Specimen		without sensor					small sensor			small sensor tens.			large sensor		
		1N	2N	4N	7N	mean	2S	9S	mean	4S(T)	5S(T)	mean	2L	3L	mean
E	[GPa]	84.7	78.2	80.5	87.1	82.6	76.1	78.2	77.2	74.0	80.5	77.3	74.8	72.1	73.5
$F_{LC,max}$	[kN]	7.97	8.07	7.66	7.46	7.79	7.45	7.33	7.39	8.65	7.52	8.09	7.61	7.98	7.80
S_{max}	[mm/m]	20.5	22.0	18.0	19.8	20.1	16.3	15.8	16.1	19.2	19.6	19.4	17.5	18.9	18.2
T	[GPa]	1.19	1.16	1.12	1.10	1.14	1.10	1.09	1.10	1.28	1.12	1.20	1.16	1.21	1.19
W	[MPa]	13.7	15.9	10.8	12.5	13.2	8.92	8.52	8.72	12.4	11.9	12.2	10.1	11.3	10.7

Table 2.7: Stiffness, ultimate load, ultimate strain, strength and toughness, derived from the force-displacement data and specimen dimensions using ASTM D6272. In total, 4 pristine specimens (N) were tested, along with 2 specimens with a small embedded sensor loaded on the compressive side of the bending test (S), 2 specimens with a small embedded sensor loaded on the tensile side of the bending

test (S(T)) and 2 specimens with a large embedded sensor loaded on the compressive side of the bending test (L).

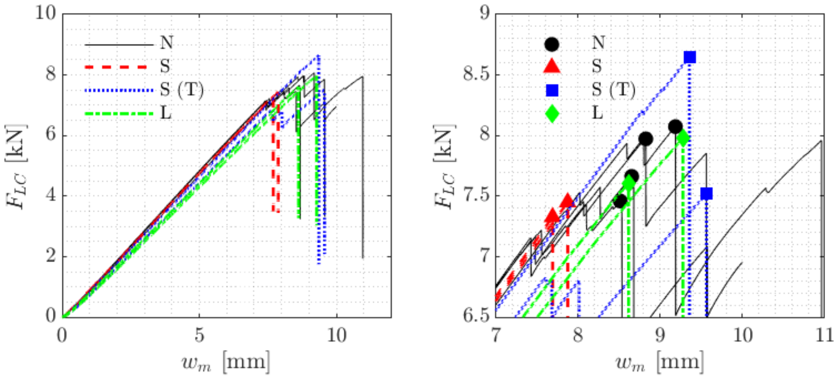

Figure 2.20: Force-displacement results during failure testing. In the more focussed right Figure, the markers indicate the maximum load resisted by the specimens.

2.6 CONCLUSIONS

Feasibility of measuring dynamic strains and damage-induced ultrasound signals in composite marine propellers was investigated. By combining finite element simulation of a specific composite marine propeller in operation and electromechanically-coupled modelling of piezoelectric wafer sensors, the study suggests that 92% of the propeller blade area allows for measurements of dynamic strains with sufficient quality up to the fourth harmonic (50Hz) of the blade using the considered embedded sensors.

It is furthermore confirmed experimentally that piezoelectric sensors embedded in a CFRP laminate are able to recover dynamic strains. With the set-up used, small-amplitude strains in the order of 20με were measured at frequencies as low as 0.018Hz. Variation in signal amplitude between the utilized sensors was relatively large (14% to 42%) and is mainly attributed to dissimilarities obtained during embedding. To be used in an independent dynamic strain measurement, an improvement in embedding procedure is considered for the future research. Among these are the use of automated soldering equipment for the joint between the sensor and the wiring as well as the use of glass-fibre prepreg instead of hand lay-up for electrical insulation prior to embedding, for example in the manner shown in Figure 2.21. This helps improve the overall geometry consistency of the sensors, reducing stress peaks during embedding as well as generating a more controllable electrical insulation.

In another experiment, damage-induced ultrasonic guided waves were successfully recorded using an embedded piezoelectric wafer sensor almost all the way up to final failure of the CFRP laminate. This was verified by comparison with two surface-bonded commercial sensors. The achieved signal-to-noise ratio of 17dB shows the capability of the embedded sensor in recording the ultrasound guided-wave signals.

The influence of embedded piezoelectric sensors on the structural integrity of the CFRP laminate when loaded under four-point bending was preparatorily investigated as well. On average, the effect turned out to be limited to 3.3% drop in ultimate strain and 8.1% drop in toughness when the sensor was embedded on the tensile side. When embedded on the compressive side, ultimate strain and toughness were on average reduced further to ranges of 9.3% to 20% and 19% to 34% respectively, depending on the sensor size. It should be mentioned that the sample size demands further experimental research. The presented research may be seen as a preliminary work for the further development of self-sensing composite marine propellers using piezoelectric sensors.

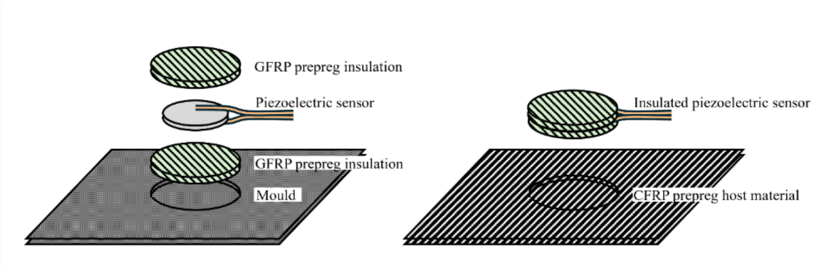

Figure 2.21: Proposed improved method for insulation of piezoelectric sensors using GFRP prepreg. Firstly the insulation is cured into a mould, with the sensor in between. Secondly, the sensor with cured insulation is placed into a conductive host material.

3

ACOUSTIC EMISSION MONITORING OF CARBON FIBRE REINFORCED COMPOSITES WITH EMBEDDED SENSORS FOR IN-SITU DAMAGE IDENTIFICATION

This chapter is based on the paper "Acoustic Emission Monitoring of Carbon Fibre Reinforced Composites with Embedded Sensors for In-Situ Damage Identification" published in 2022 in Sensors. In the context of this thesis, this chapter mostly relates to the 2nd and 3rd research sub-questions.

3.1 INTRODUCTION

As explained in the introduction chapter, the layered nature of fibre-reinforced plastic (FRP) materials allows the incorporation of sensors, such as piezoelectric disc sensors [84] or fibre-Bragg gratings (FBGs) [22]. Placing sensors within the structure gives the possibility of monitoring the structure continuously without adversely affecting the hydro- or aerodynamics nor having the sensors exposed to harsh environments [41]. From the 1980's [85] to present, a multitude of applications for embedded piezoelectric disc sensor were proposed and investigated, ranging from strain measurement [33,86], energy harvesting [36], vibration control [87], and excitation and measurement of guided waves [44,45,88,89], measurement of electromechanical impedance [90] and acoustic emissions (AE) [39,91]. The latter is the focus of the present chapter for application to structural health monitoring (SHM).

Functioning of the embedded piezoelectric disc sensor can be assessed through static capacitance measurements [40,52], impedance measurement [40] and Hsu-Nielsen tests [39]. The measurement of AE, when using piezoelectric sensors, is influenced by the spectral characteristics of the sensor [92] through the sensor's electromechanical transfer function. This influence may skew interpretations on whether certain damage mechanisms are occurring, or on the frequency content that a certain damage mechanism may emit. For embedded piezoelectric disc sensors, various models to simulate sensor behaviour exist [93–95]. Nonetheless experimental assessment of the performance and sensitivity of the sensors for AE measurement has not been sufficiently researched and needs further development.

Embedding piezoelectric disc sensors in a composite structure may also influence structural integrity and possibly, damage mechanisms [45,52,89,96,97]. Huang et al. [98] and Ghezzo et al. [99] compared specimens with and without an embedded device. AE in GFRP specimens loaded under tension with embedded devices were observed to have higher peak frequencies (up to 350 kHz) compared to baseline specimens (up to 180 kHz, depending on lay-up). Such signals were attributed to debonding and matrix cracking at the embedded device location. Xiao et al. [100] noted significant effects in AE energy and cumulative energy between CFRP specimens with and without embedded devices when loaded under tension. Early high-energy signals from the specimens with the embedded device were ascribed to CFRP-device interface delamination. This interface delamination is mentioned to cause further AE to be of relatively low energy, as compared to the energy of AE captured in baseline specimens. At the failure stage, lack of differences in the AE energy between specimens with and without embedded devices is associated with mutually occurring failure modes, such as fibre-breakage. The studies mentioned present case-specific results and it is uncertain to what extent the conclusions are applicable in situations with different loading conditions or different embedded devices. Further a method for clustering of AE signals in specimens with and without embedded sensors can provide a rigorous basis for assessment of observations, however to date it does not seem to have been reported.

Classification methods have been employed to relate AE to damage mechanisms in baseline FRPs [101]. Typically these methods rely on seeking similarities in certain key features of the AE, such as signal rise time, energy, amplitude, counts and duration in the case of Masmoudi et al. [39] and rise angle and average frequency in the case of Friedrich et al. [102]. In other research, in conjunction with assessment of aforementioned key features, the full waveforms are used [103]. For characterisation of damage in reinforced concrete structures, Kurz [104] and van Steen et al. [105,106] proposed clustering via similarity matrices. In such an approach, all waveforms are compared to each other using cross-correlation. Highly correlated waveforms are then clustered together. This method is well established in seismics to identify specific seismic emissions [107] and is expected to be greatly useful in other fields as well.

This research is aimed at providing insight into (i) qualitative assessment of the response of embedded piezoelectric sensors to damage-induced AE in CFRPs, and (ii) identification of clusters of AE that can be related to the possible damage induced by sensor embedment. To be able to assess these, CFRP beam specimens are manufactured by prepreg materials in three categories: no sensors, a smaller sensor embedded, and larger sensor embedded. Experimental sensitivity assessment of the embedded sensor mainly revolves around mirroring the response of the small piezoelectric disc sensor to that of the large piezoelectric disc sensor during four-point bending of CFRP specimens up to failure. Concurrently, surface-mounted sensors monitored the AE behaviour in all specimens. A clustering method based on waveform similarity is employed to discern AE that can be related to a damage mechanism related to the embedment of piezoelectric disc sensors.

The manufacture of the specimens, the experimental procedure, and the clustering method are explained in Section 3.2. Results are presented in Section 3.3, including observations related to the characterisation of the piezoelectric disc sensor and findings from the AE waveform clustering. Further discussions and conclusions are presented in Section 3.4.

3.2 METHODOLOGY AND EXPERIMENTS

3.2.1 Experimental Procedure

The specimens under investigation are coupons made from AS4/8552 unidirectional prepreg CFRP panels stacked in a $[[0°, 90°]_7,0°]_s$ symmetrical cross-ply lay-up. On predefined locations along the midline of the panel (in the length and width directions) and from the 21st to 25th laminae, drop-shaped cut-outs were made to accommodate the piezoelectric disc sensor. The sensor lead wire was embedded between the 22nd and 23rd laminae. A close-up view of the 22nd lamina including embedded sensor is given in Figure 3.1a. After embedding the sensor system and placing the top laminae, the CFRP laminate was debulked and autoclave-cured following the procedure recommended by the supplier [69]. A C-scan of the cured panels is shown in Figure 3.1b. After curing, the panels, with a thickness of 5.4 ± 0.1 mm, were cut into coupons of 150 mm length and 27 mm width using a Proth diamond saw.

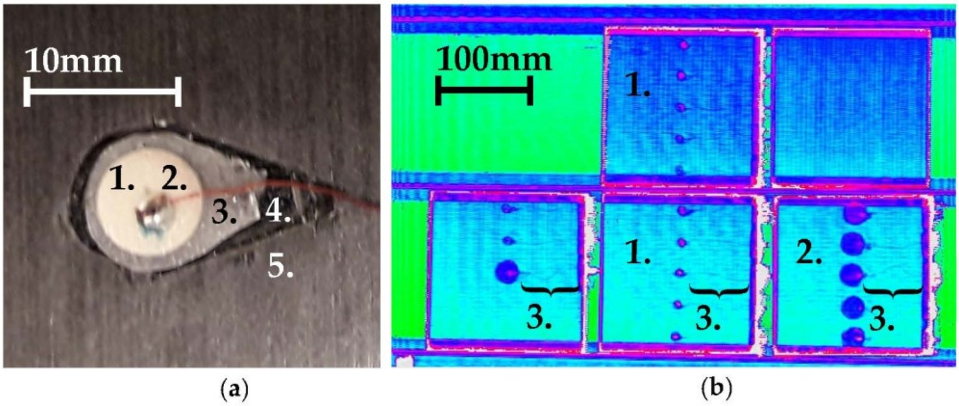

Figure 3.1: Manufacture of the specimens: (a) Close-up view of a 'small' sensor being embedded. Numbers 1 to 5 relate to the piezoelectric disc sensor, solder and wiring, GFRP insulation, CFRP cut out and CFRP host material respectively. (b) C-scan after curing of CFRP panels with embedded sensors. Specimens were cut to width afterwards. Numbers 1 to 3 refer to panels with small embedded sensors, panels with larger embedded sensors and embedded wiring.

The piezoelectric disc sensor is made of PZ27 soft composite PZT material [66] poled in thickness direction with silver electrodes on the top and bottom surfaces. This material has a recommended maximum temperature of 250 °C, which is 70 °C higher than the CFRP curing temperature. Two sizes of piezoelectric disc sensor are considered; a 'large' type with a 20 mm diameter and 0.29 mm thickness, and a 'small' type, with 7 mm diameter and 0.24 mm thickness.

Sensor lead wiring, made from bifilar urethane-enamelled copper with a 0.15 mm diameter, was soldered to the sensor using silver solder (S-Sn95Ag4Cu1). To prevent the wiring from getting damaged at the edge of the laminate due to the prepreg curing procedure, SMC style connectors were located at the laminate edge.

The conductivity of CFRP demands the sensor and connector to be electrically insulated. The piezoelectric disc sensor is laminated between two single layers of woven GFRP (HexForce 00106 with Araldite LY5052) resulting in a total sensor thickness varying between 0.7 mm and 1.2 mm. After curing, the sensor assembly was trimmed to shape. No processing of the GFRP surface has taken place. The connector was placed at one of the specimen ends during embedding between two layers of polyimide tape. Prior to and after embedding, the static capacitance of the sensor was evaluated to assess its post-manufacturing integrity.

In total 25 specimens were manufactured, among in which 18 piezoelectric disc sensors were embedded.

Non-destructive and destructive tests have been carried out to assess the sensitivity and performance of the embedded sensor in AE measurement of damage in CFRP laminate. In a preliminary non-destructive test, the performance of the embedded piezoelectric disc sensor is assessed by exciting the specimen at least five times with a Hsu-Nielsen source at a distance of 60 mm from the specimen centreline using a mechanical pencil with 0.5 mm H lead. At the top centre of the specimen, a reference R15I-AST sensor was also mounted using adhesive putty as couplant. The setup can be seen in Figure 3.2. In the destructive flexural test, two R15I-AST were placed at the bottom of the specimen, as shown in Figures 3.3b and 3.4 the piezoelectric disc sensor response is amplified with a 40 dB AEPH5 preamplifier, while the R15I-AST sensors had a 40 dB built-in preamplifier. Data was acquired using a Vallen AMSY6 system, which is able to record the full waveform based on hit definition. A digital filter was applied, allowing measurement only between 20 kHz and 960 kHz. Amplitude thresholds were set at 40 dB in all cases, with the exception for one embedded piezoelectric disc sensor where a 70 dB threshold was used due to the experienced high background noise. The full waveforms were recorded with a sample frequency of 10 MHz, which in the analysis was resampled to 2.5 MHz. A 200 µs pretrigger time is used to get an indication of the signal-to-noise ratio as well as to allow appropriate time picking for low-amplitude signals. The measurement length of the waveform was adaptive and ranged between 250 µs and 1000 µs. A rearm time (hit lockout time) and duration discrimination time (hit definition time) of both 250 µs were applied. No peak definition time was specified. Hit definition settings were identical for embedded and surface-mounted sensors.

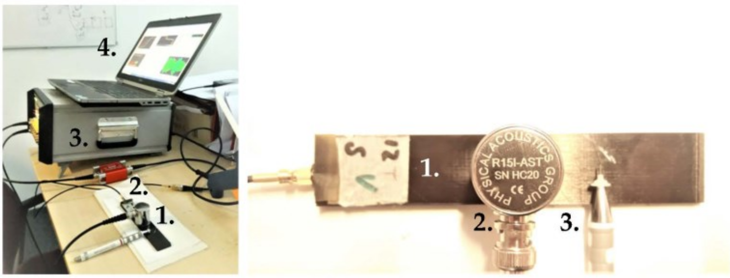

(a) (b)

Figure 3.2 Set-up for exciting and measuring a Hsu-Nielsen source [68]*: (a) Overview of the set-up, with the numbers 1 to 4 corresponding to the specimen, AEP-5H preamplifier, AMSY6 data acquisition system and a measurement computer. (b) Close-up showing the specimen (1.), AE sensor R15I-AST (2.) and a mechanical pencil with Nielsen shoe (3.). Note that in the final assessment a pencil with 0.5 mm diameter lead was used at a distance of 60 mm from the centre of the sensors.*

In the destructive tests, four types of specimens were subject to a four-point bending loading. Next to four baseline specimens (named N), two specimens with small embedded sensor on the compressively loaded side of bending set-up (S), two specimens with large embedded sensor loaded on the compressive side (L), as well as two specimens with small embedded sensors placed on the tensile side of the bending setup (ST). The different specimen types are visualised in Figure 3.3a. Further on one L-type and two of each S and ST specimens were tested to determine the ability of the embedded piezoelectric disc sensor to measure damage-related AE. The embedded sensor is placed in the centre of the specimens, facilitating that the four-point bending creates a uniform strain field over the sensor region. A schematic of the four-point bending set-up can be seen in Figure 3.4. The set-up consists of four steel loading pins of 10 mm diameter that are placed within a Zwick/Roell 20 kN universal testing machine. To prevent the loading pins from crushing the CFRP, AL6082 loading tabs with 3 mm thickness and 15 mm width were placed between the CFRP and loading pins. In the second stage of experiments, the loading tabs were electrically insulated using polyester film tape to avert interference between the sensor, CFRP and test set-up. A loading force F_{LC} was monotonically applied with a crosshead velocity of 1 mm/min. The experiment was halted when the specimen had failed, i.e., when instantaneous F_{LC} dropped to half or less of the maximum F_{LC} measured. A picture of specimen L3 with a large embedded piezoelectric disc sensor close to final failure can be seen in Figure 3.4.

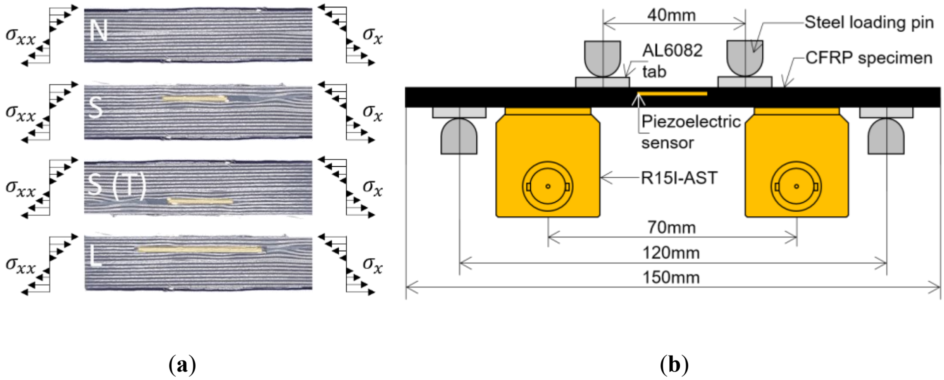

Figure 3.3: Four point bending experiment. In (a) the different types of specimens that are tested are visualised, with specimen abbreviation, sensor location and loading condition. (b) shows the dimensions and items involved in performing the four-point bending test

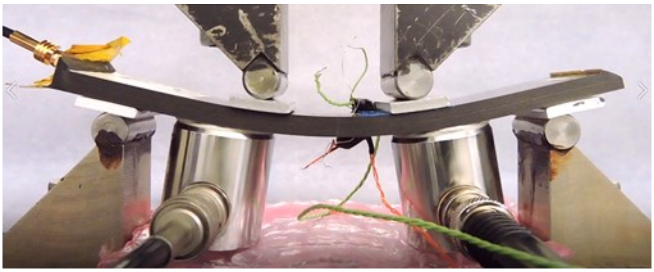

Figure 3.4: Specimen L3 with large embedded sensor in the four-point bending set-up close to failure.

3.2.2 Clustering Procedure

To relate AE waveforms to specific degradation modes, a hierarchical clustering approach employing similarity measures is used, as described by Van Steen et. al. [105]. Waveforms recorded during the testing of specimens were compared to each other using normalised cross-correlation. For a pair of waveforms $f(\tau)$ and $g(\tau)$, as function of time (τ), the cross-correlation is defined as (Equation 3.1):

$$(f \star g)(t) = \int_{-\infty}^{+\infty} f(\tau)g(\tau - t)d\tau \tag{3.1}$$

Here, t represents a time shift between the waveforms. The resulting signal is normalised with respect to the autocorrelations of the two initial waveforms (Equation 3.2).

$$\overline{R_{fg}}(t) = \frac{(f \star g)(t)}{\sqrt{(f \star f)(0)(g \star g)(0)}} \tag{3.2}$$

Waveforms should be of equal length in this procedure. This is ensured by imposing a maximum signal length of 250 μs or if shorter, the length of the shorter signal. The start of the waveform is defined by the first minimum of the Akaike Information Criterion (AIC) [108,109]. In Equation 3.3, the AIC varies over signal index n, and is dependent on the signal up to n (U_{n-}), the signal after n (U_{n+}) and signal length N [110].

$$AIC_n = n \log_{10} var(U_{n-}) + (N - n - 1) \log_{10} var(U_{n+}) \tag{3.3}$$

The normalisation from Equation (2) yields a cross-correlation parameter $\overline{R_{fg}}(t)$ varying over time shift with a value between -1 and 1. The maximum value may be seen as a measure of similarity, or similarity index (Equation 3.4), between the waveforms, with 1 and -1 indicating a perfect replication of the waveforms of the same or opposite sign while 0 is indicative for two very dissimilar waveforms.

$$similarity = 1 - dissimilarity = \max\left(\overline{R_{fg}}(t)\right) \tag{3.4}$$

By comparing all waveforms to each other, a matrix is acquired containing the similarity indices. Waveforms are grouped through average linkage, using the difference in mutual dissimilarity indices as a measure of inter-cluster distance [105]. The result is a dendrogram with similar waveforms sorted and linked to other waveforms at the value of their shared dissimilarity. Clusters are obtained by setting a threshold to the dissimilarity value, thereby dividing a group of waveforms from another group of waveforms.

3.3 RESULTS

3.3.1 Measuring AE with Embedded Sensors

In order to compare the sensitivity of the different piezoelectric sensors in use in the experiment, Hsu-Nielsen tests with the procedure described in Section 3.2 were performed. Results of specimens S11 and S12, with small (7 mm diameter) piezoelectric sensors, and L5, with a larger (20 mm diameter) piezoelectric sensor embedded were analysed. Amplitude spectra are shown in Figure 3.5.

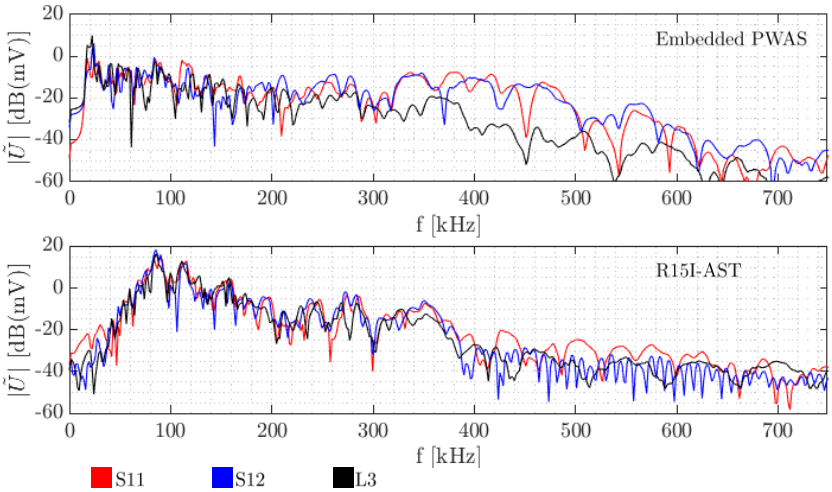

Figure 3.5: Typical amplitude spectrum of Hsu-Nielsen sources as recorded by the small and large embedded piezoelectric disc sensor and the surface-mounted sensor.

When comparing the embedded sensors, it stands out that up to 300 kHz, results are fairly similar. Beyond 380 kHz, sensitivity of the larger sensor declines. This can be partly attributed to an aperture effect, as the sensor integrates displacement over the contact area. For wavelengths that are increasingly smaller than the sensor diameter, the full wavelengths enclosed by the contact area increasingly cancel out.

For the same experiments (under the same conditions), this decreasing trend is also visible in the R15I-AST sensors from 350 kHz. Furthermore, the embedded sensors seem to be more sensitive than the R15I-AST to lower frequencies (<80 kHz), which can be partly attributed to the heavier reliance of the latter on resonant behaviour.

During the experiments outlined in Section 3.2 AE waveforms were acquired by both the embedded sensors and the surface-mounted R15I-asts. This is exemplified in Figure 3.6.

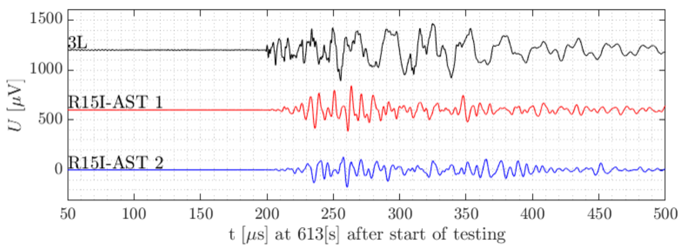

Figure 3.6: A single AE hit as measured by the embedded sensor L3 and the two R15I-AST sensors [36].

For the specimens tested, it stands out the embedded sensor is able to receive AE signals up to failure, either when loaded under compression or in tension. This may be seen in Figures 3.7 and 3.8. The frequency content acquired in the destructive tests seems generally higher than the frequencies in the preliminary tests with Hsu-Nielsen, possibly due to the different spectrum of the damage-induced source signals. The larger embedded sensor recorded AE signals with centroid frequencies mostly between 200 kHz and 300 kHz. For the smaller embedded sensor, this range was pronounced between 350 kHz and 450 kHz. For the R15I-AST sensors on all specimens, centroid frequencies tend to be between 150 kHz and 350 kHz, conforming to the transfer function of the sensor [111].

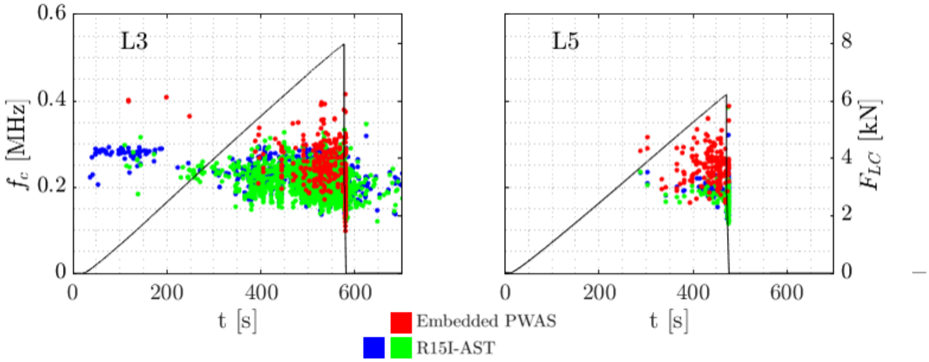

Figure 3.7: Centroid frequency f_c of all measured signals over time and load cell force F_{LC} for the large 'L' embedded sensors and the two R15I-ASTs. Note L3 has been subject to noise removal as is explained in Section 3.2.2. The final outcome is shown here.

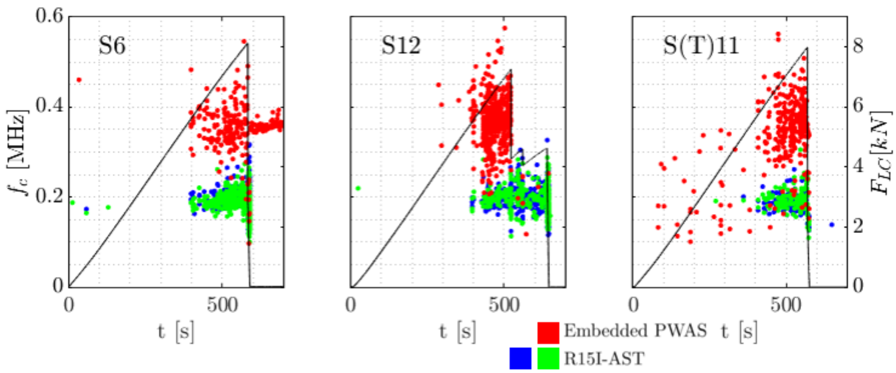

Figure 3.8: Centroid frequency f_c of all measured signals over time and load cell force F_{LC} for the small 'S' and 'ST' embedded sensors and the two R15I-ASTs.

3.3.2 Embedded Sensor Noise Mitigation during Four-Point Bending Experiments

In the first stage of testing it was noted that the embedded sensor tended to pick up extensive amounts of continuous noise. Based on the preliminary tests, this was not expected. In one case, specimen L3, no continuous-type noise but burst-type signals were acquired. A large amount were amassed continuously from the start of the testing. In Figure 3.9a three waveforms measured by the embedded sensor in early stage of testing are shown. Next to that the accumulation of signals, represented by their centroid frequency f_c, over time is illustrated.

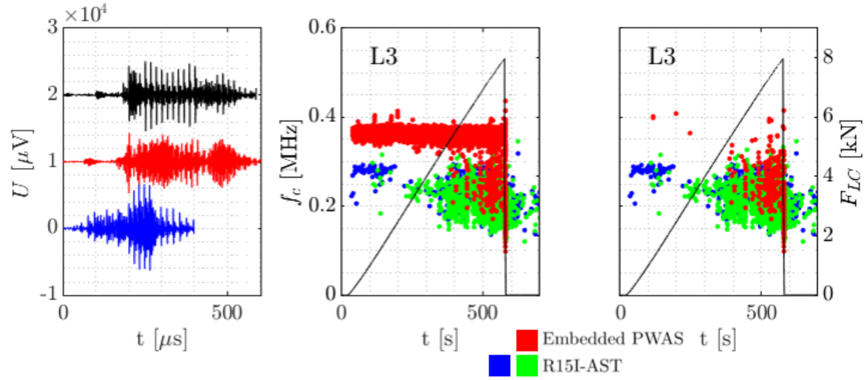

(a) *(b)* *(c)*

Figure 3.9: Noise mitigation on specimen L3: (a) Three waveforms measured in the reference timeslot between 162 s and 242 s after the start of test. They are translated in time and voltage to fit in the same image. The dissimilarity between the waveforms is between 0.65 and 0.79. (b) Centroid frequency f_c of all measured signals over time and load cell force F_{LC} for the embedded sensor and the two R15I-ASTs. (c) Equivalent to (b), but with noise removed.

Due to their early and repeating appearance (burst repetition frequency around 50 kHz), in the wave forms, these signals are considered noise. In a second batch of experiments it was identified that the continuous noise related to a metal-to-CFRP contact in the four-point bending setup. After insulating the aluminium loading tabs with polyester film tape, no such behaviour occurred anymore. Therefore this effect is not directly attributed to possible triboelectricity effects due to the external wiring [112]. Further detailed investigation of triboelectricity effects will be considered in the future research.

Measures were taken to prevent the noise from interfering with the analysis. In assessing the performance and features of the embedded AE sensor, a waveform similarity approach as described in Section 3.2 is utilised to distinguish signals of interest from noise.

For specimen L3, a total of 598 waveforms measured by the embedded sensor between 162 s and 242 s after the start of loading were used as a reference and compared to all 3939 waveforms from the embedded sensor. The resulting similarity matrix with the waveforms in chronological order is shown in Figure 3.10.

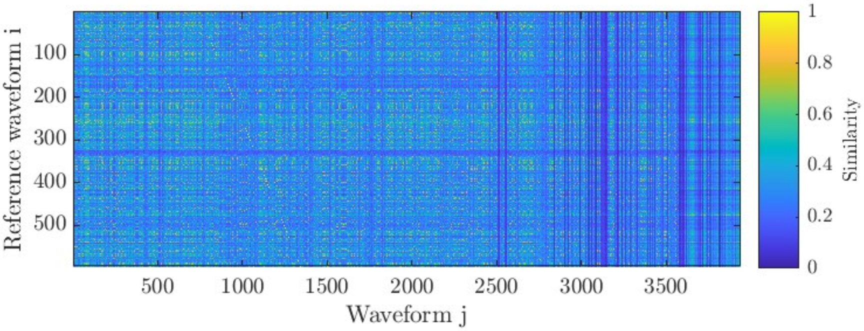

Figure 3.10: Similarity matrix with reference 'noise' waveforms correlated with the rest of data. Note the faint diagonal line between j = 800 to j = 1300, indicating autocorrelation.

The Figure shows that waveforms j (sorted in chronological order) became increasingly dissimilar from the reference waveforms (up to j = 2500 this was not the case). Regarding reference waveforms i, the different lighter and darker shades imply variations within the reference waveforms. As such, deviating waveforms may contain useful information. The criterion for defining noise was defined such that the waveform under investigation should be akin to at least 5 of the reference waveforms. In this context, 'akin' implies a dissimilarity of at most 0.65.

In Figure 3.9 the waveforms shown on the left have a dissimilarity between 0.65 and 0.79, visualising the boundaries of the criterion. In the middle and right, the effect of removing the noise signals may be seen. Although waveforms similarity inherently takes into account similarity in frequency content, the comparison shows the noise mitigation is sensitive enough to retain dissimilar signals with a similar frequency content, as exemplified by the waveforms in the 350–400 kHz band.

In the identification of waveforms related to embedded sensor-induced damage, measurements from the embedded sensor were not included in the analysis to prevent possible influence of damage to the sensor during the experiments. Only waveforms measured near-simultaneously (within 10 µs) by the two surface-mounted R15I-ASTs were examined.

3.3.3 Identification of Damage Mechanisms Occurring Due to the Embedding of a Piezoelectric Sensor

During the four-point bending experiment, a number of damage mechanisms were registered. In general from F_{Lc} = 6 kN and beyond the upper laminae between the loading tabs showed signs of damage, in the form of delamination and fibre fracture on the top surface. Failed specimens are depicted in Figure 3.11[68].

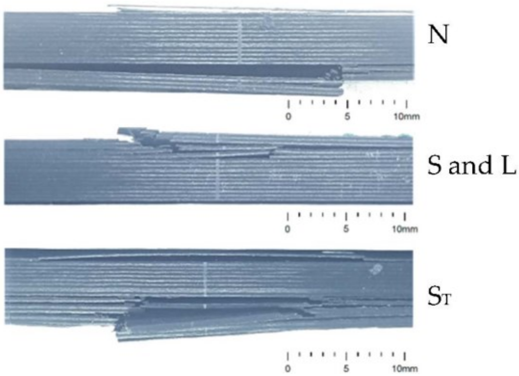

Figure 3.11: A side view showing damage occurring in different types of specimens [68].

For baseline specimens that had no sensor embedded (N) this damage on the compressive side is protracted up to near the fourth lamina before gross failing in the tension side, including delamination and fibre breakage in three of the specimens. In one of the specimens of type N, failure occurred solely on the compressive side close to the loading tabs. For specimens failing on the tension side, this location was between 8 mm and 21 mm from the centre of the specimen.

In specimens where a sensor was embedded on the compressive side (S and L type specimens) of the beam final failure occurred on the compressive side in an instantaneous manner reaching from the top surface to the laminae that contained the embedded sensor. Generally the location of rupture seemed to coincide with the interface between the CFRP and the embedded sensor. In one specimen however, failure was near the centre. The rupture can be considered as a combination between delamination and compressive fibre failure. Furthermore, the sensors did fail together with the GFRP insulation. This can be regarded as an extra damage mechanism, due to a combined in-plane compression and out-of plane shear stress (related to the bending setup).

Like in the baseline specimens, for the specimens with sensors embedded on the tension side of the beam (S_T) the initial damage on the compressive side did not extend beyond the top laminae. At increasing loads, acute failure occurred on the tension side of the specimens, approximately 4.5 mm to 8 mm off-centre up to the laminae with embedded sensors. Similar to the s and L specimens, degradation modes relate to delamination and tensile fibre failure. Failure of the sensor itself and insulation is caused by combined in-plane tension and out-of plane shear stress.

In short, the different damage mechanisms are given in Table 3.1.

Table 3.1: Damage mechanisms as registered during four-point bending. The numbers signify that the mechanism is found in that amount of specimens. Note that for "N" type, there were 4 specimens, the other types had 2 specimens.

Damage Mechanism	N	S	S_T	L
Preliminary delamination on compressive side	4	2	2	2
Preliminary fibre breakage on compressive side	4	2	2	2
Extensive fibre breakage on compressive side	1	2	0	2
Extensive fibre breakage on tensile side	3	0	2	0
Sensor system failure on compressive side	0	2	0	2
Sensor system failure on tensile side	0	0	2	0

During the failure of specimens as described in Section 3.3.2 two R15I-AST surface-mounted transducers were continuously recording AE. Next to the registration of the waveforms, features such as waveform energy E_{AE} were directly extracted. As stated in Section 3.3.1, to prevent the background noise contaminating the assessment, only AE recorded simultaneously (first threshold crossings within 10 µs from each other) by both sensors is considered. Waveform energy (E_{AE}) and cumulative energy (ΣE_{AE}) over time are shown for the different specimens in Figure 3.12.

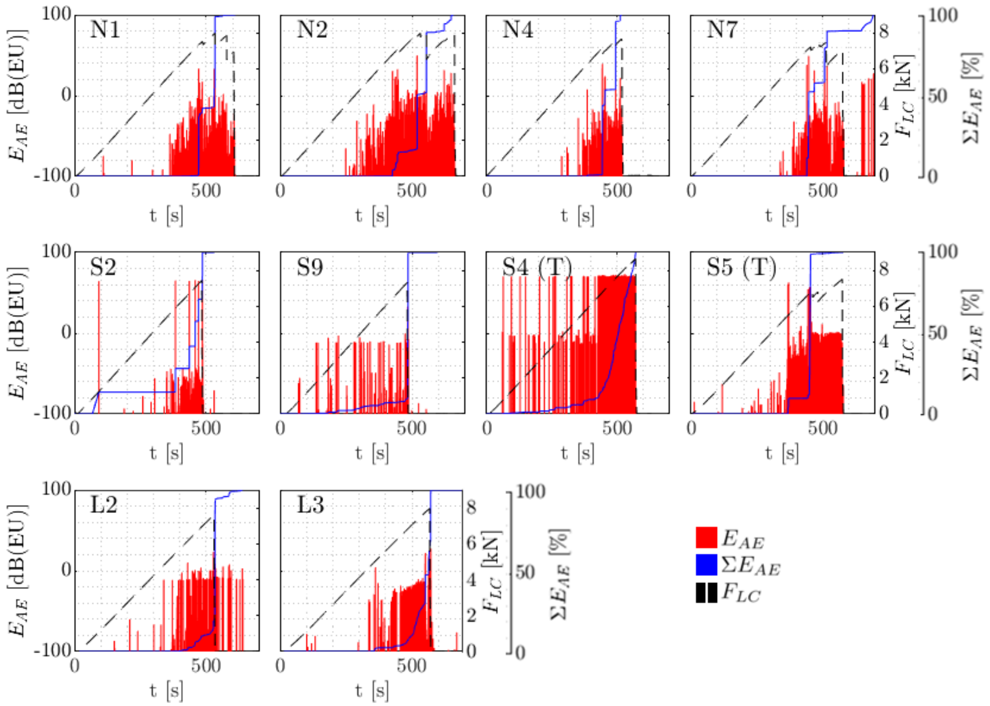

Figure 3.12: Energy per hit E_{AE} and cumulative energy [% of total] over time and crosshead force F_{LC}.

From the Figure it can be noted that in baseline (N) specimens, energy-rich AE started to occur from 6000 N onwards and increased in energy around the failure load of the specimens. For specimens with large embedded sensors on the compression side of the specimen (L2 and L3), energy content seems to be fairly comparable to the baseline specimens. For their counterparts with smaller piezoelectric disc sensors, AE in specimens S2 and S9 seem to commence relatively early, around 1–1.5 kN. For specimens with embedded piezoelectric disc sensors on the tensile side (S_T4 and S_T5) it appears that the recorded energy is larger than with the other specimens throughout the testing. This can be seen in Table 3.2 as well, with the cumulative energy of S_T specimens being higher than in other specimens (with reasonable statistically significance). When considering specimen S_T5, high-energy AE around 5000 kN is observed, followed by lower-energy AE. This reminisces of the observations from Xiao et al. [100]. The lower-energy AE after 5000 kN however is not generally lower than experienced in baseline specimens.

Table 3.2: Cumulative energy ΣE_{AE}.

	N	S	S_T	L
ΣE_{AE} [$\times 10^6$EU]	4.0×10^2	1.3×10^4	1.1×10^6	3.1×10^2
	9.0×10^2	1.2×10^2	2.5×10^4	8.1×10^1
	3.5×10^2			
	7.0×10^2			

Building further on the measurement of AE as explained in Section 3.2, effort is made to identify AE that is characteristic to failure related to the embedding of a piezoelectric sensor. Interpretation relies on the comparison between clusters of AE measured in the sensor-less baseline specimens, and those from the specimens with sensors embedded.

Using the method described in Section 3.2, a similarity matrix is constructed, containing similarity information of AE waveforms captured during the loading and failure of all specimens. The obtained similarity matrix can be seen in Figure 3.13. In this Figure the waveforms are ordered chronologically. Near the diagonal in Figure 3.13, lighter colours with a similarity between 0.8 to 1 are visible. This suggests that similar waveforms are grouped in time and may be attributed to similar damage mechanisms in the same specimen. Further from the diagonal similarity values overall seem to be somewhat lower, but the extent thereof is mostly waveform-specific. Also there are recurring patterns of higher similarity as well as waveforms that do not tend to relate to the others.

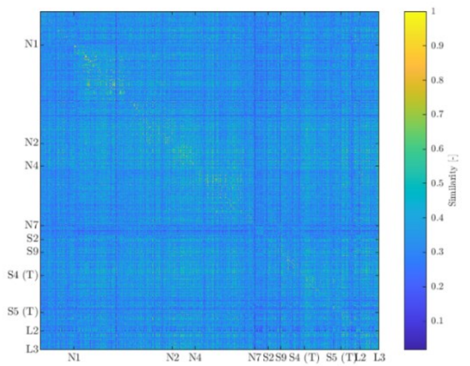

Figure 3.13: Similarity matrix containing all 15081 waveforms measured during loading and failure of the ten specimens. Indices relate to the last wave form from the specimen.

To further elaborate on above observations and in the pursuit of clustering the waveforms, a dendrogram (Figure 3.14) is formed using the dissimilarity as explained in Section 3.2. It is noticeable from the dendrogram that there are few groups of waveforms that have a high mutual similarity (or low dissimilarity, <0.3) while the bulk of waveforms tend to distinguish themselves in the 0.3–0.7 dissimilarity range.

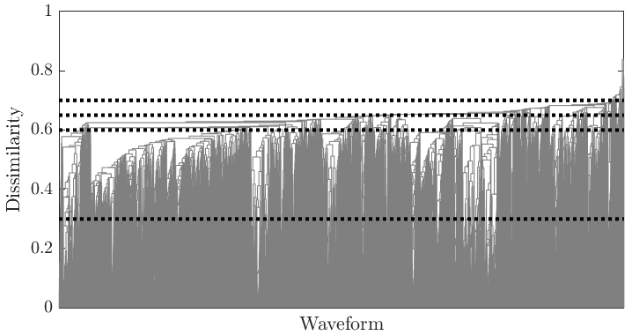

Figure 3.14: Dendrogram linking the data from the similarity matrix in Figure 3.13. The dashed lines represent the thresholds considered in the definition of clusters. Note that along the horizontal axis the waveforms are no longer ordered sequentially.

For the purpose of clustering a similarity threshold is defined. This threshold separates waveforms along a maximum value of dissimilarity. The value for this threshold is not trivial: a low dissimilarity threshold can result in highly similar clusters, but those may be excessively specific to individual specimens and not relate to global phenomena across multiple specimens. On the other hand, a high dissimilarity threshold may overlook relevant clusters. Variations in local FRP fibre volume fraction and direction, the initiation of damage, the placement of the sensor and the thickness of the couplant can cause variations in wave propagation details between different specimens. This results in AE from similar damage that may have relatively high levels of dissimilarity. To ensure variations between specimens (of the same type) do not influence the identification process, the threshold is selected such that major clusters contain waveforms from multiple specimens of the same type. It should be noted this selection relies on the assumption that the dissimilarity between different damage mechanisms is larger than the dissimilarity between multiple specimens given the same damage mechanism.

For a dissimilarity threshold of 0.65, in total 154 clusters were formed, with the bulk of waveforms (92%) found within 8 clusters. Table 3.3 describes the distribution of clusters over the specimen types. In Figure 3.15, the clusters are visualised as centroid frequency over time. In Figure 3.16 three normalised waveforms are shown belonging to clusters 103, 109 and 126.

Table 3.3: Major clusters formed using a threshold of 0.65. For each type of specimen, the percentage of waveforms caught in the clusters is given.

Cluster Number	N [%]	S [%]	S_T [%]	L [%]
5	3	3	3	5
11	19	12	13	8
21	2	0	3	1
102	0	1	4	0
103	61	37	53	70
104	3	4	0	1
109	0	1	12	0
126	4	19	1	6
Total	92	77	89	91

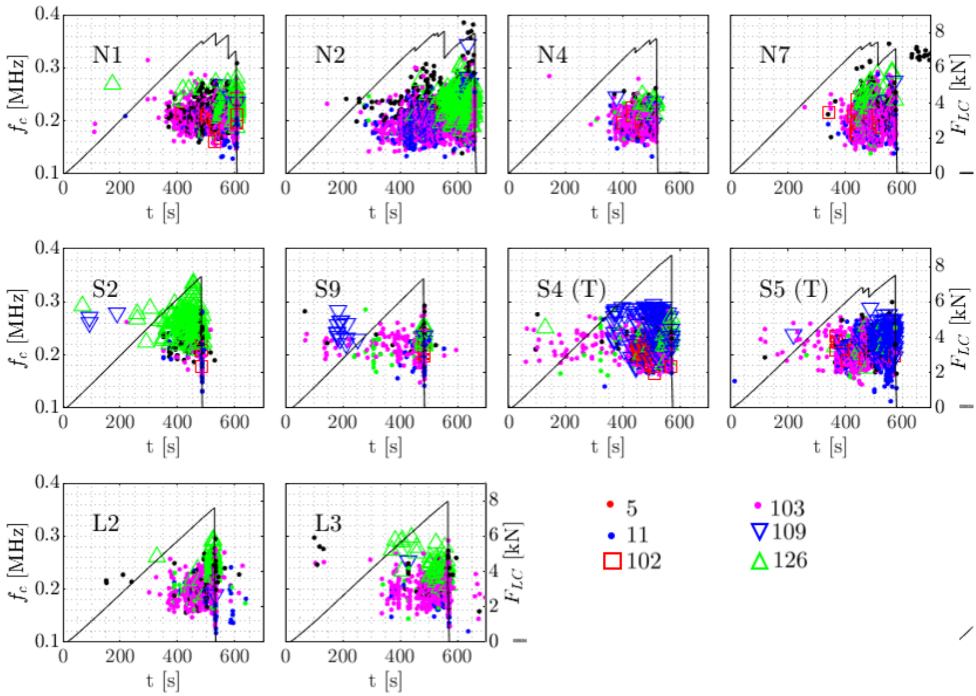

Figure 3.15: The AE clusters for each specimen, centroid frequency f_c of the waveforms in the clusters and the applied load F_{LC}.

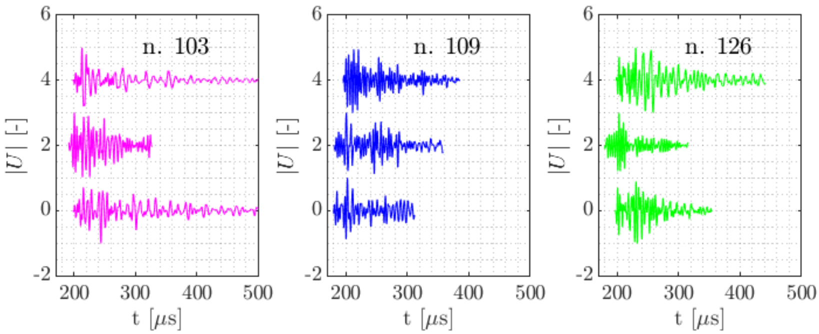

Figure 3.16: Normalised examples of waveforms from cluster numbers 103, 109 and 126.

From the table and Figure 3.15 L specimens appear to show behaviour most alike to baseline N specimens, with a comparable distribution of clusters in number and over testing time. Note that this can be mirrored to the failure load of the L specimens, which compared to S specimens is relatively similar to N specimens. AE from S specimens are slightly less represented by the proposed clusters (77% of all waveforms) with the remaining waveforms being placed in smaller clusters with high reciprocal dissimilarity. Cluster 126, with a relatively high centroid frequency, occurs in S2 from around F_{LC} =2 kN whereas in baseline (N) specimens, this cluster is far more limited in number and associated with final failure. In S_T specimens most distinct is the abundance of cluster 109, including 325 waveforms uniformly divided over the two specimens. In the other specimens the occurrence is almost negligible (40 waveforms in all other specimens combined). The high repeatability of the cluster possibly allows attribution to damage mechanisms related to the specific embedding procedure and the combined in-plane tension stress and out-of-plane shear stress that is experienced in S_T.

In Figures 3.16 and 3.17 similarity of the waveforms within clusters and between clusters can be visually assessed. In these Figures the waveforms per cluster are coming from different specimens and are picked randomly. In the time domain, it may be seen there are similarities around the onset of some of the waveforms per cluster. In frequency domain it appears that cluster 103 has most frequency content below 200 kHz. In cluster 109 the low frequency content around 200 kHz and a large frequency content around 220 kHz show to be the uniting factors. In cluster 126 such relations are less apparent.

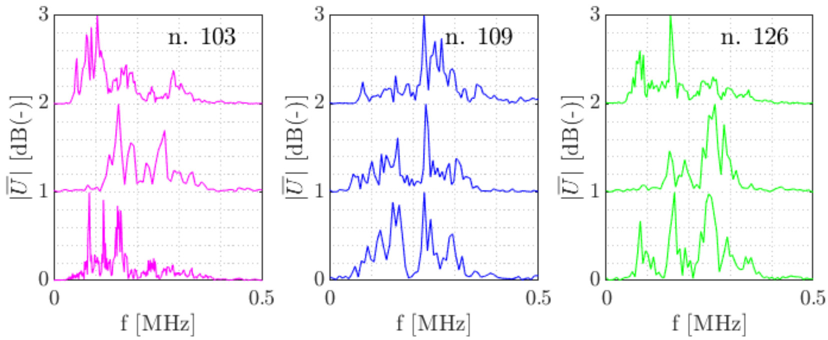

Figure 3.17: Normalised amplitude spectra belonging to the waveforms from Figure 3.16.

To summarise, clusters are formed using waveform dissimilarity. This clustering generally represents AE behaviour that is repeatable over different specimens with the same embedded sensor type. Furthermore AE cluster distribution in specimens with embedded sensor is compared to that in the baseline specimens. It may be noted that specimens with a large (L type, 20 mm diameter) sensor embedded on the compressive side of the bending setup exhibit comparable AE behaviour to that of the baseline specimens. Conversely in specimens with smaller sensors embedded on the same side (S type, 7 mm diameter) AE tends to be relatively dissimilar in general, but clusters with high frequency content seem to occur earlier than in baseline specimens. For specimens with the embedded sensor loaded in tension (S_T, 7 mm diameter), a cluster (cluster 126) is noted that appears to be specific to this type of specimen. This suggests the presence of a possible damage mechanism related to the embedded sensor experiencing combined in-plane tension stress and out-of-plane shear stress.

3.4 DISCUSSION

3.4.1 Measuring AE with Embedded Sensors

Acoustic emissions originating from mechanical degradation sources were measured in CFRP specimens with embedded piezoelectric disc sensors and standard surface-mounted piezoelectric sensors. Two sizes of embedded piezoelectric disc sensor (20 mm and 7 mm diameter) were compared in terms of performance and sensitivity. Typically, embedded piezoelectric disc sensors were able to acquire AE up to final failure. In the measurement of damage-related AE from a flexural strength test, the smaller embedded piezoelectric disc sensor (7 mm diameter) recorded AE with a centroid frequency typically ranging between 350 kHz and 450 kHz. For the larger embedded piezoelectric disc sensor (20 mm diameter) centroid frequencies were determined to be generally between 200 kHz and 300 kHz. In all cases, the reference R15I-AST sensors measured centroid frequencies between 150 kHz and 350 kHz. The variation in sensitivity between the larger and smaller embedded piezoelectric disc sensor is partly attributed to an aperture effect by taking into account the wavelength of the propagating wave of interest. This implies that embedded sensor dimensions and FRP wave propagation properties should be carefully assessed in the design and analysis of an FRP structure with embedded piezoelectric disc sensors.

3.4.2 Waveform Similarity Assessment for Identification of Noise and Damage Mechanisms

A waveform similarity approach was used for defining AE clusters and in the processing of noise. It was shown using average linkage and a dissimilarity threshold that clusters of AE can be formed that are overarching different specimens while being specific enough to accentuate the effects found in different specimen types. This confirms the assertion that the dissimilarity of AE between different types of specimens is larger than the dissimilarity between multiple same-type specimens. As is seen in Figures 3.14, 3.16 and 3.17 differences in dissimilarity within clusters are relatively large while between the clusters the differences in dissimilarity are relatively low. This indicates that for a small difference in dissimilarity threshold, large differences in the formation of clusters are obtained. Cluster 109, that is assigned to be specific to specimens with embedded piezoelectric disc sensors on the tensile side of the bending test, is considered of note due to its occurrence being almost exclusive to this type of specimens as well as its distribution being comparable over the two specimens of this type.

3.4.3 Identification of Damage Mechanisms Occurring Due to the Embedding of a Piezoelectric Sensor

From the combination of waveform similarity and AE energy assessment it may be concluded that the AE behaviour of the two specimens with embedded piezoelectric disc sensor on the tensile side of the bending load are distinctly different from the baseline and other specimens. The identified AE phenomena are envisioned to be associated to a tensile cohesion-related failure, since the strength of the GFRP-resin-CFRP interface is subject to large uncertainty. Tensile fracture of the piezoelectric disc sensor is not expected as a likely source given the low stiffness of GFRP and resin insulation, as confirmed by the embedded piezoelectric disc sensor in specimen S_T11 that recorded up to gross failure. Given the inaccessibility of the location of damage for detailed inspection during the test, further validation related to the degradation mode is needed.

Between baseline specimens and specimens with embedded piezoelectric disc sensor on the compressive side under the bending load, no clear relation in terms of AE can be established. Although visually the damage mechanisms in these specimens are different compared to baseline specimens, this did not translate to sufficiently consistent trends in AE.

3.4.4 Outlook and Future Research

From a wider perspective, the ability to relate AE to embedded sensor-affiliated and non-affiliated degradation mechanisms allows for the monitoring of a structure with embedded piezoelectric disc sensors with respect to the health of the structure. Further, the monitoring for embedded sensor-induced degradation facilitates the development of design criteria for structures with embedded piezoelectric disc sensors. In this regard, the observation that AE from piezoelectric disc sensor-induced damage is distinguishable from other sources, prior to specimen gross failure and depending on loading direction, is of value. It is considered that this work will also pave the way for more widespread use of embedded piezoelectric disc sensors, such as in larger-scale FRP structures with embedded arrays or distributed configurations.

This research can be seen as a preliminary step towards assessing the influence of embedded piezoelectric disc sensor size and location on their measurement capabilities and on the structural integrity of the host structure. As such, it is acknowledged that the topics and outcomes presented in this research can be elaborated upon, by means of extended experiments and numerical simulations. Measuring different wave modes with different wave lengths and the effect on the sensitivity of embedded piezoelectric disc sensor deserves further research. Evaluation with respect to the sensitivity of the embedded piezoelectric disc sensor is envisioned on different host materials, such as GFRP and sandwich structures. The clustering method used may be compared to other clustering procedures that are used typically in the classification of FRP damage mechanisms. In this context, the respective qualities of the formed clusters may be assessed. Moreover, it is recognised that increasing the population size of the specimens will help drawing more accurate and definite conclusions on the formation of AE clusters related to embedded piezoelectric disc sensor-induced damage. Also, this will allow specimens in the destructive testing to be stopped prematurely so that they can be inspected microscopically for the initiation of damage mechanisms. The premature inspection will facilitate attributing clusters to damage mechanisms. In a further stage, a database of clusters of waveforms with identified damage mechanisms may be used to quantify the nature and extent of damage in similar structures. The features of AE signals from identified damage mechanisms can also be used to develop possible damage indices to better estimate the remaining load bearing capacity or remaining lifetime.

3.5 CONCLUSIONS

Using data from destructive four-point bending tests performed on thick CFRP specimens with embedded piezoelectric disc sensor the performance of the piezoelectric disc sensor in terms of endurance and spectral sensitivity for AE measurement was investigated. Furthermore, a waveform similarity assessment method was employed to identify clusters of AE signals that relate to embedded piezoelectric disc sensor-induced failure mechanisms. It was found that:

(1) The size of the embedded piezoelectric disc sensor has an effect on the frequency content of the measurement of AE signals; Damage-related AE signals in CFRP specimens were measured with a centroid frequency between 350 kHz and 450 kHz by the 7 mm diameter embedded piezoelectric disc sensor, while for the 20 mm embedded piezoelectric disc sensor the range was between 200 kHz and 300 kHz. For comparison, no change in frequency content in the AE signals was measured by a reference surface-mounted sensor for the different specimens.

(2) Damage mechanisms in the CFRP laminates due to embedded piezoelectric disc sensor when placed in the tension side in the bending experiment exhibited AE that were reasonably distinguishable from other sources of AE. This was confirmed when assessing waveform similarity and AE energy in specimens with and without embedded sensors. When loaded under compression, no major additional degradation AE due to the embedment process was identified.

4

ACOUSTIC EMISSION MONITORING OF COMPOSITE MARINE PROPELLERS IN SUBMERGED CONDITIONS USING EMBEDDED PIEZOELECTRIC SENSORS

This chapter is based on the journal paper "Acoustic emission monitoring of composite marine propellers in submerged conditions using embedded piezoelectric sensors" published in 2024 in Smart Materials and Structures. The focus of this chapter is on answering research sub-questions 1 and 2.

4.1 INTRODUCTION

The marine industry is in the process of improving its environmental footprint. This involves reduction of carbon emissions as well as reduction of underwater radiated noise (URN) for the protection of marine mammals [113,114]. The use of flexible composite marine propellers is envisioned to help in obtaining these reductions. The directed flexibility of such propellers enables the blade shape to be adaptable to different loading conditions [115,116]. This can improve efficiency [117]. Furthermore, pressure peaks on the blade are reduced due to blade-tip flexibility. This can lead to reduced URN [118]. Additional advantages of composite propeller blades are a reduced electromagnetic signature, lower weight, and the ability to have sensors incorporated [1].

The development of flexible composite marine propeller blades has encountered uncertainties regarding their behaviour in fatigue and failure. This matters as unanticipated failure of a propeller blade will considerably limit a vessel's manoeuvrability. Prominent causes to the uncertainties are deviations and imperfections during fabrication, the varying loading of the blade, and a complex internal stress state imposed by the thick intricate geometry and spatially-varying material layup [9,10]. Additionally, depending on their location and load history, different damage types may grow to gross failure or cause a stress redistribution that leads to different failure [12]. Given the complexities and the involved risk, there is a need for structural health monitoring (SHM) of flexible composite propeller blades.

In an advanced state of damage, the changes in material properties lead to global effects, such as an increased deformation or changes in vibrational response. This could be measured using externally mounted measurement devices such as cameras and hydrophones. Deformation behaviour of flexible propeller blades was measured in-situ by Maljaars et al. (2018) [14] using digital image correlation. The cameras were installed on a ship rudder. This method was similarly used in a cavitation tunnel for flexible propeller blades by Su et al. (2022) [119]. Using laser beam irradiation and an image registration method, Shiraishi, Sawada and Arakawa (2023) [120] were able to estimate the full-blade deformation shape of a flexible propeller in a cavitation tunnel. Kluczyk, Grządziela and Batur (2022) [121] described damage identification in flexible propeller blades by monitoring of hydroacoustic behaviour using hull-mounted hydrophones. Sensors mounted onto or embedded into the blade can be used for the same purpose. Here, there is a strong preference to have the sensors embedded into the composite laminate. This is because the rotating underwater blade presents a harsh environment for surface-mounted sensors. Furthermore, surface-mounted sensors can obstruct hydrodynamic performance. Investigations relating to composite hydrofoils include the use of embedded strain gauges, fibre-Bragg gratings and distributed optical fibres for strain measurements and accelerometers and piezoelectric sensors for modal assessments. Strain gauges were placed on flexible and metal model propeller blades by Tian et al. (2016) [23]. They were able to measure vibratory responses. Zetterlind, Watkins and Spoltman (2003) [21] compared the use of surface-mounted strain gauges and fibre-optic sensors for strain monitoring during fatigue assessment of composite aerospace propeller blades. The research described increased survivability of fibre-optic sensors compared to strain gauges. For a composite marine propeller blade, Seaver, Trickey and Nichols (2006) [19], embedded fibre-bragg gratings (FBGs) during manufacturing and demonstrated the feasibility of measuring strains in a water tunnel. Complexities were noted regarding the embedding procedure. FBGs were also used by Javdani et al. (2016) [20], who placed these on the surface of a full-scale metal propeller. Modal analysis with the propeller submerged showed a good agreement with simulated results. Ding et al. (2022) [24] measured strains on a model of a propeller blade using surface-mounted FBGs. Reconstructed deformations of the blade were created using an inverse finite element method. Error between reconstructions and deformation measurements was below 7%. Maung et al. (2017) [25] embedded distributed optical fibres into a carbon-fibre composite hydrofoil. It was noted that the measured strains were in reasonable accordance with simulations. This research was continued by Shamsuddoha et al. (2022) [10] who embedded distributed optical fibres into a full-scale composite hydrofoil loaded under fatigue. In that work, also piezoelectric accelerometers were placed to perform modal analysis. No notable change in modal properties was measured during the fatigue loading. The use of embedded piezoelectric sensors for the use of dynamic strain measurement of composite marine propeller blades was assessed by the authors [122] and demonstrated by de Bles (2022) [74]. Hamada et al. (2023) [32] placed piezoelectric line sensors on flexible propeller blades in operation. Degradation of the propeller blade was correlated with the changes in the vibration measured by the sensors.

In early stages of damage the global effects become less pronounced and other methods for SHM in composite propellers become relevant. One promising method is the measurement and processing of acoustic emissions (AE). An AE signal is an ultrasound elastic burst emanating from material degradation. Fibre-reinforced composite materials have a multitude of damage mechanisms such as matrix cracking, fibre-matrix interface debonding, fibre breakage and fibre pullout. Each of these mechanisms have distinct AE characteristics, such as specific frequency content and amplitude [67,103,123]. Conventionally, AE has been measured using piezoelectric sensors. These sensors allow for a high enough sample rate for measuring AE. Additionally, they are more easily embedded into complex composite structures than optical methods .

In marine applications, simulated AE signals have previously been measured on a submerged steel half rudder blade. Measurement and localisation of an AE source was performed while comparing different sensor types [124]. Furthermore, AE investigations on composite tidal turbine blades are emerging [125]. Next to a preliminary feasibility study by the authors [122], no published research on AE in full-scale composite marine propeller blades is known to date.

The localisation of the AE and the characterisation of the damage mechanism can be fundamental in the assessment of the structural health and in the estimation of remaining lifetime of the structure. To enable localisation and characterisation, the measured signals need to be of sufficient signal to noise ratio. The evaluation for the signal to noise ratio requires estimations of the expected noise level and the AE source signal amplitude, and indication of the location of the degradation with respect to the sensor location. Further, the knowledge of the attenuation behaviour of AE for different degradation mechanisms is instrumental for this assessment.

The localisation of the AE and characterisation of the damage mechanism can be fundamental in the assessment of structural health and the estimation of the remaining lifetime of a structure. To enable localisation and characterisation, the measured signals must be of sufficient signal-to-noise ratio. The evaluation for the signal-to-noise ratio requires estimations of the expected noise level and the AE source signal amplitude, and an indication of the drop in signal amplitude over the propagation path from source to sensor. The drop in signal amplitude depends on the propagation distance and attenuation due to material behaviour and geometry.

Hence, wave propagation attenuation will influence the quality of the measured signal and the maximum measurable distance between a sensor and an AE source. This implies that wave propagation attenuation over the blade is of profound relevance for the assessment of the feasibility of localisation and characterisation of AE.

This chapter investigates the measurement and attenuation of AE signals in a submerged composite marine propeller blade using embedded piezoelectric sensors. This encompasses the experimental excitation, measurement and assessment of AE signals on a full-scale submerged propeller blade. A glass-fibre reinforced polymer blade has been manufactured using vacuum-assisted resin transfer moulding. During the production, 24 piezoelectric wafer sensors have been embedded into the blade. AE signals have been simulated by applying pencil lead break (PLB) excitations at several locations on the propeller blade. This has been done while the propeller was submerged in artificial seawater. For each PLB, the AE signal is measured for each connected sensor and assessed for their spectral content. The spectral content and the change in spectral content over excitation locations are used to obtain a measure of amplitude drop throughout the blade. These values can be used to assess the feasibility of measuring specific types of AE signals relating to specific types of damage mechanisms.

Regarding the organisation of the chapter, firstly a description of the measurement and assessment of an AE signal is given. This includes the definition of an amplitude drop and the assumptions that are associated with that. Secondly, the experimental procedure is explained. This provides details on the manufactured propeller blade and measurement specifics. Next, results of the measurements are presented, combined with an assessment of the amplitude drop throughout the blade. Finally, conclusions are drawn and recommendations are given for future research.

4.2 METHODOLOGY

The measurement of an AE signal can be described as an AE source signal that has been distorted by wave propagation effects, sensor transfer function, and noise. For plate-like structures, the AE can propagate in the form of guided waves. These waves appear in a multitude of through-thickness deformation (wave) modes and propagate in in-plane direction. In a mathematical sense, the measurement $P(\mathbf{x}_R,\mathbf{x}_S,\omega)$ can be written as the convolution of AE source signal $\mathcal{S}_i(\mathbf{x}_S,\omega)$ with wave propagation transfer function $W_i(\mathbf{x}_R,\mathbf{x}_S,\omega)$ and sensor transfer function $D_i(\mathbf{x}_R,\omega)$, and the addition of noise $P_N(\mathbf{x}_R,\omega)$ [57,126]. When propagating in the form of guided waves, each component can be dependent on the wave mode $i=[1..n]$ for n modes, the source location $\mathbf{x}_S$, sensor location $\mathbf{x}_R$ and frequency ω. For the source signal $\mathcal{S}_i(\mathbf{x}_S,\omega)$, multi-modal contributions are captured by modal amplitude $\varsigma_i(\mathbf{x}_S)$. The frequency and phase content of the source is represented by $S(\mathbf{x}_S,\omega)$. This is elaborated in Equation 4.1 and Equation 4.2.

$$\mathcal{S}_i(\mathbf{x}_S,\omega)=\varsigma_i(\mathbf{x}_S)S(\mathbf{x}_S,\omega). \tag{4.1}$$

$$P(\mathbf{x}_R,\mathbf{x}_S,\omega)=\sum_{i=1}^{n}D_i(\mathbf{x}_R,\omega)W_i(\mathbf{x}_R,\mathbf{x}_S,\omega)\varsigma_i(\mathbf{x}_S)S(\mathbf{x}_S,\omega)+P_N(\mathbf{x}_R,\omega). \tag{4.2}$$

Here, the wave propagation transfer function $W_i(\mathbf{x}_R,\mathbf{x}_S,\omega)$ includes attenuation, dispersion, cut-off of higher modes ($\omega_{cut,i}$) and skewing of waves as a function of location, distance and direction. Sensor transfer function $D_i(\mathbf{x}_R,\omega)$ includes electromechanical behaviour relevant to embedded piezoelectric sensors, such as the aperture effect [56,127].

Assessment can be performed regarding the components $W_i(\mathbf{x}_R,\mathbf{x}_S,\omega)$ using measurements $P(\mathbf{x}_R,\mathbf{x}_S,\omega)$ from different known source locations to different measurement locations over the blade. Further, assessment of $P_N(\mathbf{x}_R,\omega)$ is used to examine the quality of $P(\mathbf{x}_R,\mathbf{x}_S,\omega)$.

Assessment of wave propagation

For a given sensor layout and an arbitrary source location, the drop in amplitude for specific frequency components from a sensor adjacent to the source to a sensor further away can be considered as a measure of frequency-dependent attenuation along the blade. This drop can be calculated as per Equation 4.3.

$$\begin{aligned}A(\mathbf{x}_R,\mathbf{x}_S,\omega_l)&=\frac{P(\mathbf{x}_R,\mathbf{x}_S,\omega_l)}{P(\mathbf{x}_{Rref},\mathbf{x}_{Sref},\omega_l)}\\&=\frac{\sum_{i=1}^{n}D_i(\mathbf{x}_R,\omega_l)W_i(\mathbf{x}_R,\mathbf{x}_S,\omega_l)\varsigma_i(\mathbf{x}_S)S(\mathbf{x}_S,\omega_l)+P_N(\mathbf{x}_R,\omega)}{\sum_{i=1}^{n}D_i(\mathbf{x}_{Rref},\omega_l)W_i(\mathbf{x}_{Rref},\mathbf{x}_{Sref},\omega_l)\varsigma_i(\mathbf{x}_{Sref})S(\mathbf{x}_{Sref},\omega_l)+P_N(\mathbf{x}_{Rref},\omega)}.\end{aligned} \tag{4.3}$$

In this equation, for each relevant frequency ω_l the amplitude drop in $dB_{\mu V}$ $A(\mathbf{x}_R,\mathbf{x}_S,\omega_l)$ is calculated for a sensor at location $\mathbf{x}_R$ with respect to a reference sensor at $\mathbf{x}_{Rref}$ that was adjacent to a reference source $\mathbf{x}_{Sref}$. Amplitude drop $A(\mathbf{x}_R,\mathbf{x}_S,\omega)$ can be seen as an approximation for wave propagation transfer function $W_i(\mathbf{x}_R,\mathbf{x}_S,\omega)$ (Equation 4.10). This is considered valid under five assumptions.

As a first assumption, wave propagation effects from source to reference can be regarded negligible (Equation 4.4)) when the considered wave mode exists ($\omega>\omega_{cut,i}$).

$$W_i(\mathbf{x}_{Rref},\mathbf{x}_{Sref},\omega)\approx\begin{cases}0 & \text{for} \quad \omega\le\omega_{cut,i}\\1 & \text{for} \quad \omega>\omega_{cut,i}\end{cases}. \tag{4.4}$$

For the second assumption, the sources of both the reference and the other signals are considered similar (Equation 4.5).

$$\varsigma_i(\mathbf{x}_S)S(\mathbf{x}_S,\omega_l) \approx \varsigma_i(\mathbf{x}_{Sref})S(\mathbf{x}_{Sref},\omega_l)\,. \quad (4.5)$$

The third assumption is that at frequency ω_l there is one dominant wave mode m. Here, the description of the wave propagation transfer functions simplify (Equation 4.6 and 4.7) and summation over wave modes $i=[1..n]$ is eliminated.

$$W_i(\mathbf{x}_{Rref},\mathbf{x}_{Sref},\omega_l) \approx \begin{cases} 0 & \text{for} \quad i \neq m \\ 1 & \text{for} \quad i = m \end{cases}. \quad (4.6)$$

$$W_i(\mathbf{x}_R,\mathbf{x}_S,\omega_l) \approx \begin{cases} 0 & \text{for} \quad i \neq m \\ W_m(\mathbf{x}_R,\mathbf{x}_S,\omega_l) & \text{for} \quad i = m \end{cases}. \quad (4.7)$$

The fourth assumption is that the sensor transfer function of the measurement is the same as that for the reference (Equation. 4.8).

$$D_i(\mathbf{x}_R,\omega_l) \approx D_i(\mathbf{x}_{Rref},\omega_l)\,. \quad (4.8)$$

As a fifth assumption, the noise amplitude is regarded significantly smaller than the measurement signals (Equation 4.9)).

$$P_N(\mathbf{x}_R,\omega) \approx P_N(\mathbf{x}_{Rref},\omega) \ll \sum_{i=1}^{n} D_i(\mathbf{x}_R,\omega)W_i(\mathbf{x}_R,\mathbf{x}_S,\omega)\varsigma_i(\mathbf{x}_S)S(\mathbf{x}_S,\omega)\,. \quad (4.9)$$

Given these assumptions, Equation 4.3 is reduced to Equation 4.10:

$$\begin{aligned} A(\mathbf{x}_R,\mathbf{x}_S,\omega_l) &\approx \frac{D_m(\mathbf{x}_R,\omega_l)W_m(\mathbf{x}_R,\mathbf{x}_S,\omega_l)\varsigma_m(\mathbf{x}_S)S(\mathbf{x}_S,\omega_l)}{D_m(\mathbf{x}_{Rref},\omega_l)W_m(\mathbf{x}_{Rref},\mathbf{x}_{Sref},\omega_l)\varsigma_m(\mathbf{x}_{Sref})S(\mathbf{x}_{Sref},\omega_l)} \\ &\approx W_m(\mathbf{x}_R,\mathbf{x}_S,\omega_l) \end{aligned}\,. \quad (4.10)$$

4.2.1 Assessment of noise level

The noise level can be used to define the minimum measurable signal amplitude as a reference. In the current work, the pre-trigger period $P_N^*(\mathbf{x}_R,\omega_l)$ of a measurement is regarded as an indication of the noise level. Values of $P(\mathbf{x}_R,\mathbf{x}_S,\omega_l)$ are used in the assessment when they are complying with Equation 4.11, given a positive value for criterion A_N.

$$\frac{P(\mathbf{x}_R,\mathbf{x}_S,\omega_l)}{P_N^*(\mathbf{x}_R,\omega_l)} > A_N\,. \quad (4.11)$$

4.2.2 Comparison between measurement and reference AE signals

The attenuation $A(\mathbf{x}_R,\mathbf{x}_S,\omega)$, in conjunction with a noise level $P_N^*(\mathbf{x}_R,\omega_l)$, can then be compared to reference amplitude levels and frequency content of types of AE from literature that are associated with different damage mechanisms. This comparison gives insight in the maximum distance between AE signal source location and sensor location for different regions of the blade. This is in general relevant for the placement of embedded sensors with respect to the location and type of damage-induced AE signal to be measured.

4.2.3 Experimental procedure

For the experimental procedure, first the manufacturing of a composite marine propeller blade with embedded piezoelectric sensors is described. This followed by a description of the experiment itself, including AE signal excitation and measurement specifics.

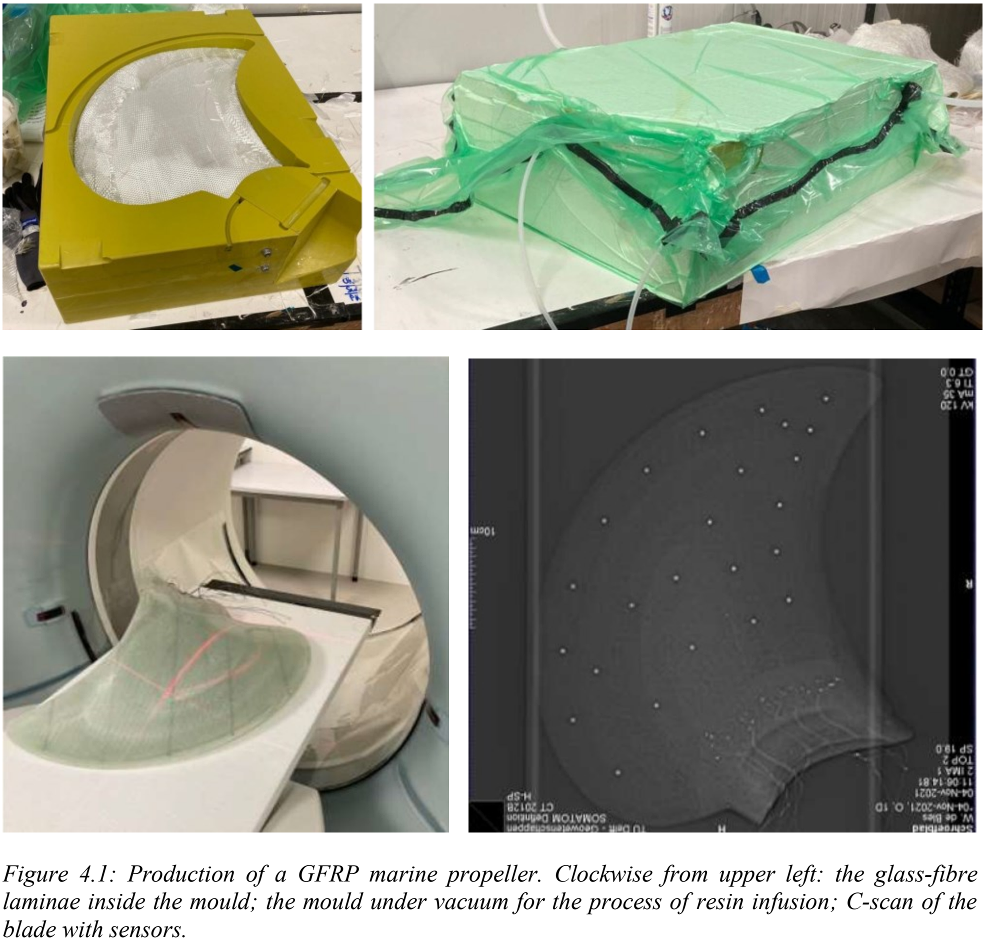

Figure 4.1: Production of a GFRP marine propeller. Clockwise from upper left: the glass-fibre laminae inside the mould; the mould under vacuum for the process of resin infusion; C-scan of the blade with sensors.

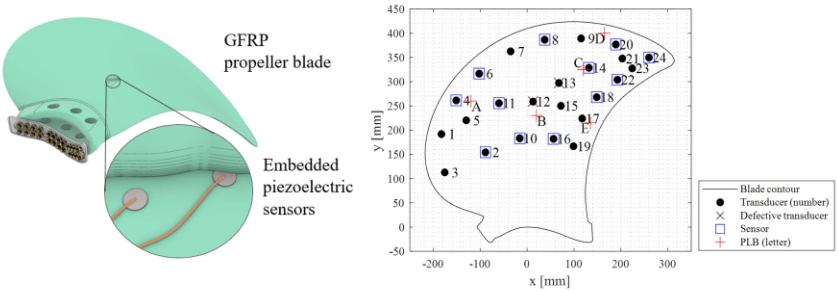

Figure 4.2: A GFRP marine propeller blade with embedded piezoelectric sensors: the general concept (left), and expanded view of the blade with transducer labelling and distribution (right).

A glass-fibre reinforced polymer blade was produced with embedded piezoelectric transducers. The production included vacuum-assisted resin transfer moulding within a closed mould. The mould contained the lay-up. This lay-up consists of woven fabrics at the outer layer, followed by alternately stitched unidirectional laminae and chopped strand mat (CSM) layers. In the middle of a laminate, multiple layers of CSM make up the core. In Figure 4.1 a general overview of the manufacturing and the quality control process using a CT-scanner are shown. The layup and material properties of the blade have been chosen following the design of Maljaars et al. [14].

A total of 24 transducers were embedded at a quarter of the thickness of the blade (ply 18-25, closest to suction side). The concept and transducer distribution can be seen in Figure 4.2. The transducers were of the PRYY+0398 type (PIC255, Ø5mm, t0.25mm). Wiring was through bifilar copper cables (Ø0.15mm). During lay-up of the laminae, the wiring was pulled through above laminae up to the core. Here the wiring was routed towards the hub end of the blade. After resin infusion and curing, two transducers were noted to be defective due to wiring breakage during embedding and demoulding. In total, 22 transducers were operational. This is a 92% survival rate, which at this stage of the program is considered more than adequate.

The experiment involved the exciting and measuring guided waves using embedded transducers in a submerged composite propeller blade. This enables assessment of the measurability and localisation of damage-related AE signals on the blade. A schematic and overview of the experimental setup are shown in Figure 4.3.

The experiments were performed in dry, fresh water (<1mS/cm) and salt water (53mS/cm, reference at 25˚C) conditions. In the submerged experiments, the blade was suspended into a water tank (600×600×600mm) with blade hub and connectors of the transducers remaining above the waterline. The connectors remained unsubmerged because they are not rated for underwater use. If, in the future an experiment would be deemed necessary with the blade fully submerged, the connectors would be exchanged for ones that are rated for underwater use, such as the LEMO 03 series [128].

The excitations were based on pencil lead breaks (PLB). Five locations on the blade were selected on the pressure side surface of the blade (A-E). The PLBs are denoted as red plusses in Figure 4.2. A standard Hsu-Nielsen source was used (Leads Ø0.35mm, 2H, extension 3.5 ±1mm). The PLBs were repeated at least five times.

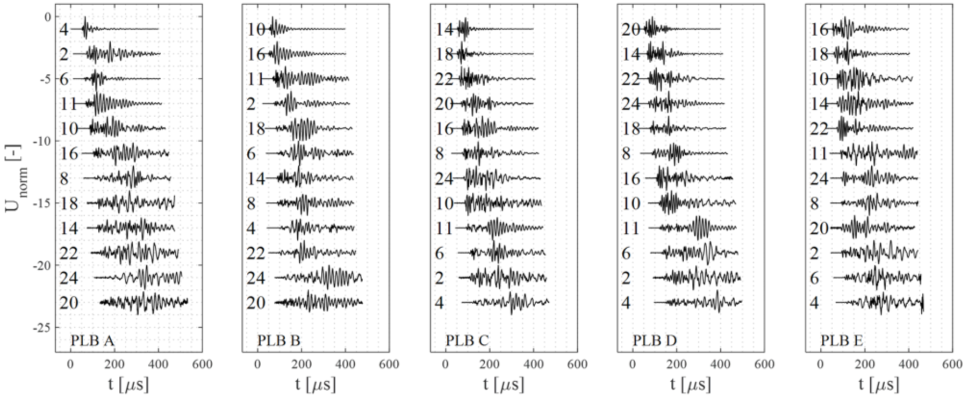

Figure 4.4: Measurements from a PLB at location A-E in salt water: note the general delay in arrival time and increase in dispersion from top to bottom waveform signals. The waveforms are normalised. The annotation numbers denote the sensor number.

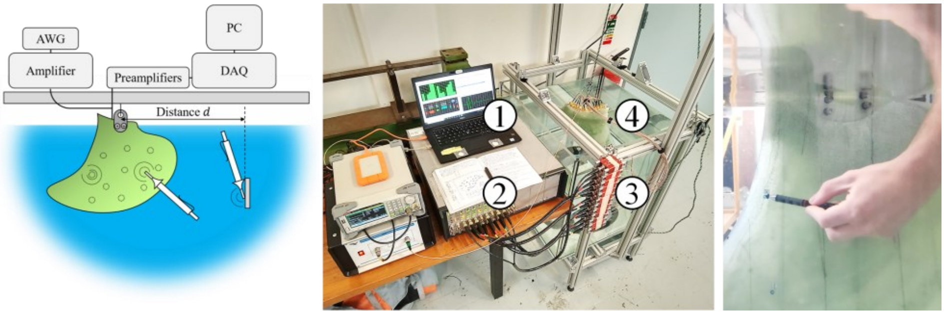

Figure 4.3: The experimental setup: on the left a schematic of the broader setup showing main devices and excitations (left). In the centre a photograph of the setup, where numbers 1 to 4 denote the measurement laptop, data acquisition system, preamplifiers and submerged propeller blade respectively. On the right photograph, the execution of an underwater pencil lead break (PLB) at position E is visible.

During each excitation, 12 out of 22 transducers were used as sensor. These can be seen in Figure 4.2 as blue squares. The sensors were connected to AEPH5 preamplifiers (40dB), and from there to an AMSY-6 data acquisition system. The data acquisition system was grounded to the water in the tank. The data acquisition system and preamplifiers are shown in Figure 4.3 as parts 2 and 3 respectively. The sampling frequency was 2.5MHz. The acquisition was hit-based and had a rearm and duration discretization time of 50µs, and a pre-trigger period of 50µs. A digital band-pass filter was applied ranging from 20kHz to 850kHz. In the dry and fresh water conditions, a detection threshold of 40dB (with reference to 1 µV) and a floating threshold (or threshold-to-noise ratio)[129] of 6dB were applied. In salt water, the detection threshold was lowered to 20dB.

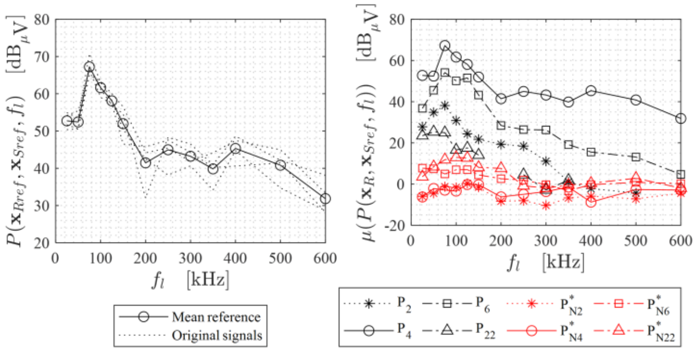

Figure 4.5: Amplitude spectra for measurements $P(\mathbf{x}_{Rref},\mathbf{x}_{Sref},\omega_l)$, $P(\mathbf{x}_R,\mathbf{x}_S,\omega_l)$ *and noise* $P_N^*(\mathbf{x}_R,\mathbf{x}_S,\omega_l)$. *Here source* $\mathbf{x}_S=\mathbf{x}_{Sref}$ *is at PLB location A. The left graph shows the variation in frequency content for reference measurements* $P(\mathbf{x}_{Rref},\mathbf{x}_{Sref},\omega_l)$ *and its mean. On the right graph, the mean values of* $P(\mathbf{x}_R,\mathbf{x}_S,\omega_l)$ *and noise* $P_N^*(\mathbf{x}_R,\mathbf{x}_S,\omega_l)$ *for different measurement locations are given. Note that the subscript denotes the sensor number as per Figure 2.*

4.3 RESULTS AND DISCUSSION

4.3.1 Measurements of pencil lead breaks

The PLBs from the five locations were detected by all sensors. An example of a measurement set from PLBs in salt water is shown in Figure 4.4. The signals are arranged from top to bottom with increasing arrival time. Note the sequence with respect to the source location.

For each of the signals, the amplitude is shown in Table 4.1. It is noticeable that the amplitudes drop when the measurement location is further away from the source location. The measurements of sensor 4 for source location A are considered as reference measurements $P(\mathbf{x}_{Rref},\mathbf{x}_{Sref},\omega_l)$. This is because the high amplitudes indicate low attenuation and it is known that the distance from source to sensor is small, around 30mm.

Table 4.1: Amplitudes belonging to the measurements of Figure 4.4. A grayscale is added to denote low to high amplitude values.

Sensor no.	PLB A [dB$_{\mu V}$]	PLB B [dB$_{\mu V}$]	PLB C [dB$_{\mu V}$]	PLB D [dB$_{\mu V}$]	PLB E [dB$_{\mu V}$]
2	60	68	41	41	51
4	92	62	53	54	54
6	81	60	55	53	57
8	55	58	60	66	59
10	57	86	47	47	54
11	71	63	54	56	52
14	48	56	77	70	56
16	54	77	57	51	66
18	47	60	75	64	67
20	49	53	64	81	57
22	45	55	65	66	64
24	50	49	56	68	57

4.3.2 Drop in amplitude spectra along the blade

From the measurements described above, the drop in amplitude for specific frequency content is assessed. This follows the method of Equation 4.3 described in Section 4.2. The amplitude spectra for both the signals and pre-trigger periods are obtained through a Fast Fourier Transform. For location A, mean values of the amplitude spectra of five pencil lead breaks are given in Figure 4.5. Note that for higher frequencies at sensors that are away from the source, values drop and approach noise levels. Individual values from measurements are only used when compliant with Equation 2.11, using an A_N of 3dB. Mean values $\mu(P(\mathbf{x}_R,\mathbf{x}_S,\omega_l))$ are deduced from these individual measurements and used in further analysis. For a more comprehensive assessment, a moving average with a span of 10kHz is used. Corresponding standard deviations are typically well below 5dB.

Since reference and assessment amplitude spectra, $\mu(P(\mathbf{x}_{Rref},\mathbf{x}_{Sref},\omega_l))$ and $\mu(P(\mathbf{x}_R,\mathbf{x}_S,\omega_l))$, are now defined, it is possible to determine amplitude drop $\bar{P}(\mathbf{x}_R,\mathbf{x}_S,\omega)$ through Equation 4.10. For pencil lead break locations A-E in salt water and frequencies 100kHz, 250kHz and 500kHz, contour graphs are made. These are shown in Figure 4.6. Here $\bar{P}(\mathbf{x}_R,\mathbf{x}_S,\omega)$ defines the isolines and colour.

From the Figure, several observations can be made:

Acoustic emissions are successfully measured by the embedded sensors when the blade is submerged.

The drop in amplitude over distance seems to be generally monotonic. Interesting exceptions to this are at sources B, C and E. Here sensors along the leading edge (4,6) have relatively large values compared to sensors deeper in the blade (11,14).

For 500kHz, there was a limitation in the distance that the amplitude drop can be quantified. This is due to the low signal-to-noise ratio at larger distances and higher frequencies. It is noticeable through the smaller domain that is covered by the sensors.

For 500kHz, attenuation is higher than for 100kHz and 250kHz. Besides shown in Figure 4.6, this is also illustrated in Table 4.2. Here, amplitude drop is normalised with the distance between source and sensor to provide an attenuation metric. Note that the values for 500kHz are influenced by point 3.

Table 4.2: Attenuation $\mu(\bar{P}(\mathbf{x}_R,\mathbf{x}_S,\omega))/\|\mathbf{x}_R-\mathbf{x}_S\|$ averaged over sensor location in terms of dB$_{\mu V}$/mm. A grayscale distinguishes low and high values of attenuation.

f_l [kHz]	PLB A [dB$_{\mu V}$/mm]	PLB B [dB$_{\mu V}$/mm]	PLB C [dB$_{\mu V}$/mm]	PLB D [dB$_{\mu V}$/mm]	PLB E [dB$_{\mu V}$/mm]
100	-0.18	-0.23	-0.28	-0.19	-0.23
250	-0.22	-0.18	-0.26	-0.21	-0.20
500	-0.28	-0.31	-0.33	-0.36	-0.28

From Table 4.2, further it can be seen that PLB C has relatively low attenuation values. This is mainly due to the measurement at sensor 14. This sensor is close to source C, yet has a comparatively low value.

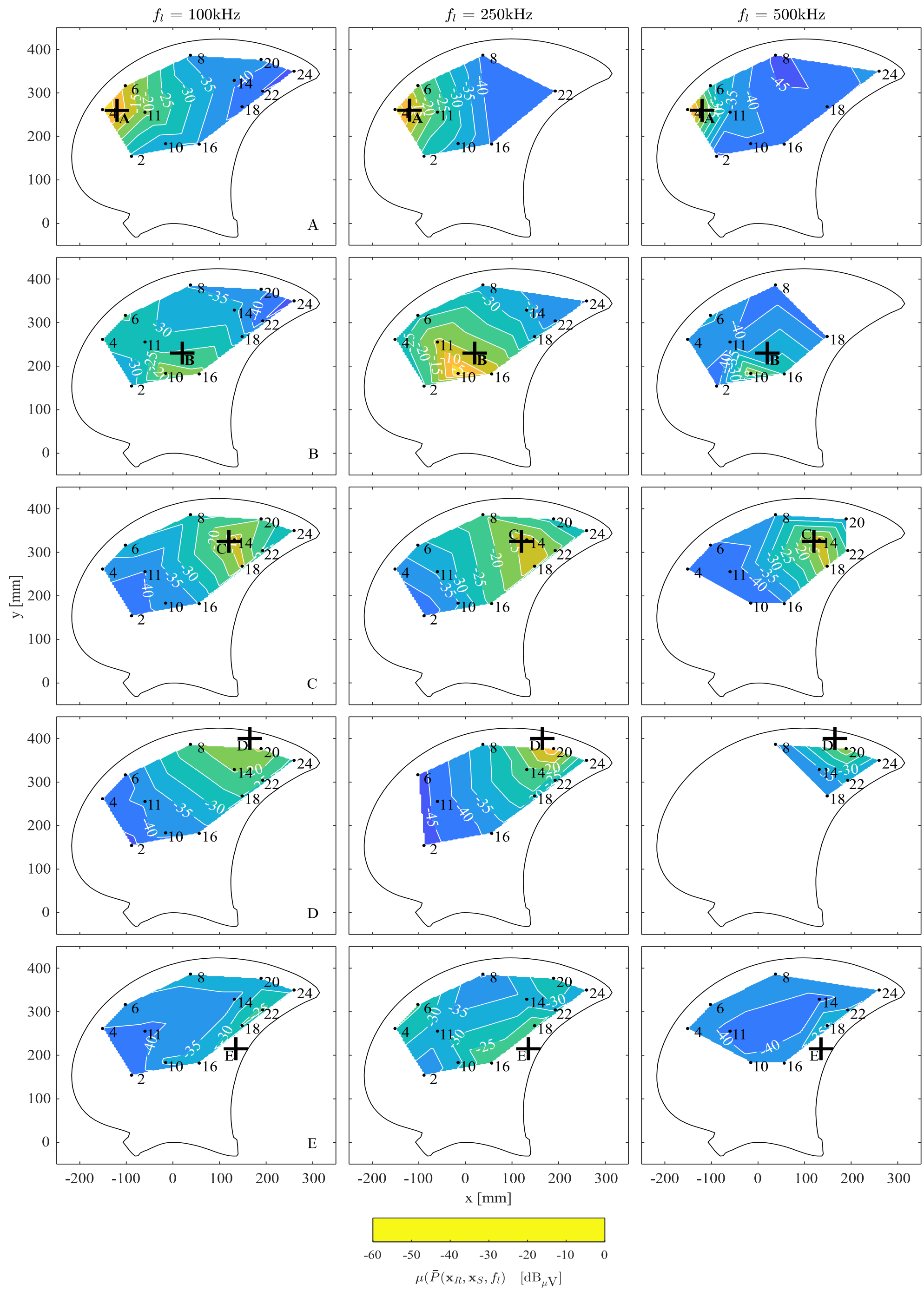

Figure 4.6: Mean drop in amplitude $\mu(\overline{P}(\mathbf{x}_R, \mathbf{x}_S, \omega_l))$ for pencil lead breaks at A-E for frequency components 100kHz, 250kHz and 500kHz. The location of the pencil lead break is denoted by the upright cross. Relevant sensor locations are labelled in black. The white labelling refers to the isolines.

For illustration, acoustic emissions can be assessed for an indication of their maximum measurable distance $\max\|\mathbf{x}_R - \mathbf{x}_S\|$. Here, specific trajectories are disregarded by averaging values of $\mu(\bar{P}(\mathbf{x}_R, \mathbf{x}_S, \omega)) / \|\mathbf{x}_R - \mathbf{x}_S\|$. Further, different values for the reference amplitude $P(\mathbf{x}_{Rref}, \mathbf{x}_{Sref}, \omega)$ and noise level $P_N(\mathbf{x}_R, \omega)$ are considered. An A_N of 3dB is taken into account. Values for $\max\|\mathbf{x}_R - \mathbf{x}_S\|$ are shown in Table 4.3.

Table 4.3: Indication of maximum measurable distance $\max\|\mathbf{x}_R - \mathbf{x}_S\|$ for acoustic emissions with reference amplitude $P(\mathbf{x}_{Rref}, \mathbf{x}_{Sref}, \omega)$, noise level $P_N(\mathbf{x}_R, \omega)$ and frequency component f_l.

$P(\mathbf{x}_{Rref}, \mathbf{x}_{Sref}, \omega)$ [dBµV]	90	70	50	90	70	50
$P_N(\mathbf{x}_R, \omega)$ [dBµV]	20	20	20	40	40	40
$\max\|\mathbf{x}_R - \mathbf{x}_S\|$ [mm] for $f_l = (100, 250)\text{kHz}$	307	216	124	216	124	32
$\max\|\mathbf{x}_R - \mathbf{x}_S\|$ [mm] for $f_l = 500\text{kHz}$	215	151	87	151	87	22

Table 4.3 illustrates that for both higher and lower frequency content and noise level, a distance of 85mm between source and sensor typically would be sufficient. However, for a high noise level and low signal amplitude, a shorter distance would be necessitated. It should be noted that these values are indicative in nature and that a sensor lay-out can be drastically optimised. This optimisation can take place when there is specification of:

1. The expected location and type of occurring damage.
2. The frequency content and amplitude of these damage mechanisms.
3. The expected noise level.

The results indicate that acoustic emissions can be measured in a submerged composite marine propeller blade using embedded piezoelectric sensors. Further, typical values for amplitude drop and attenuation are given. These can in later research be used to enhance sensor locations.

4.4 CONCLUSION

For the purpose of structural health monitoring, feasibility of measuring acoustic emissions was assessed for a composite marine propeller blade. In an experimental set-up, a blade with embedded piezoelectric sensors was submerged into salt water and excited with pencil lead breaks. It was noted that:

1. Embedded piezoelectric sensors can measure acoustic emissions on the blade when underwater.
2. Amplitude drop has a generally monotonic behaviour over the distance from the source along the blade.

3. There is more attenuation for higher frequency (500kHz) components of an acoustic emission than for lower frequency components (100kHz and 250kHz).
4. For typical source amplitudes and noise levels at 500kHz frequency, a lower limit of the maximum distance between source and sensor was approximated around 87mm. For frequencies between 100-250kHz, this is 124mm. In the case of high noise (40dB) and low amplitude (50dB) a shorter distance is required. It should be noted that the source-to-sensor distance can be much improved upon through anticipation of source location, type, amplitude and frequency content and noise level.

These observations highlight the feasibility of measuring acoustic emissions in composite marine propeller blades using embedded piezoelectric sensors. The presented results open up further research opportunities, such as optimisation of the sensor lay-out for different damage types, and damage localisation and characterisation methodologies for composite marine propeller blades.

5

ACOUSTIC EMISSION SIGNAL RECONSTRUCTION AND LOCALISATION IN THICK COMPOSITES

This chapter is based on the conference paper "Numerical and Experimental Study of Acoustic Emission Source Signal Reconstruction in Fibre-Reinforced Composite Panels" presented in 2022 in the European Workshop on Structural Health Monitoring and the conference paper "Acoustic Emission Source Localization in Fiber-Reinforced Composites based on Multimodal Dispersion Compensation of Guided Waves" presented in 2023 in the International Workshop on Structural Health Monitoring. The focus of this chapter is on answering research sub-questions 2 and 4.

5.1 INTRODUCTION

In plate-like structures, acoustic emission (AE) signals can propagate as guided waves. The velocity and attenuation behaviour in guided waves is dependent on material and geometrical properties as well as the frequency content of the AE. In the case of anisotropic plates, it is further dependent on the direction of propagation of the guided wave [130,131]. This behaviour implies that measurement of a single AE signal can be different at different measurement locations. As such, for both identification of damage mechanisms through AE evaluation and localisation of the damage, differences in measurement due to wave propagation effects need to be accounted for.

Wave propagation effects can be accounted for by reconstructing source AE signals at the source location from the measurement signals. Several methods have been proposed in the literature for signal reconstruction including dispersion compensation. Among them are Time Reversal (TR) and Fourier-domain dispersion compensation [132].

In active TR, the guided wave generated by transducer A is measured by transducer B, reversed in time, re-emitted from B and measured by A. In passive TR, the re-emission from B takes place in a simulation [133]. For AE signal reconstruction of pencil lead breaks and broadband signals, Falcetelli et al. [134,135] provided transfer functions in isotropic thin panels using active TR. In thin fibre-reinforced plastic (FRP) panels, signal reconstruction was performed by means of active [136] and passive [133] TR.

Fourier-domain dispersion compensation has conceptual similarities with passive TR [137,138]. The method typically makes use of a priori known wavenumber-frequency dispersion relations to analytically reconstruct a source waveform. Different approaches have been presented [132,139]. Fourier-domain signal processing has been applied in the active localisation of damage and phase reconstruction in isotropic materials [137,140,141] and FRPs [59,132].

Various methods for AE localization have been put forward for fibre-reinforced composite materials [142]. One of these methods is time-distance domain migration (TDDM). This method maps the full waveform to a distance domain and then back-propagates this to account for dispersion [139]. On fiber-reinforced composites, Caj et al. [143,144] used TDDM for processing active guided wave testing. Wilcox [145], Jiao et al. [146], de Marchi et al. [147] and Grabowski et al. [148] suggested a method to apply TDDM or similar for AE localization. These works performed back-propagation assuming the dispersion of a single dominant wave mode. In thicker composites, the AE can propagate in a multitude of wave modes, each having different dispersion characteristics and an unknown magnitude. This complicates AE localization as contributions of other wave modes will give an erroneous back-propagation. Xu et al. [149] and Wu & Wang [150] described multimodal back-propagation in thicker panels. They noted that back-propagation using a specific mode will compress and amplify the contribution of that mode in the measurement, streamlining further assessment.

The abovementioned research provide valuable insights into the potential use of back-propagation techniques for guided waves. What has not been sufficiently reported so far is the application of these methods for processing of AE in thick composites. This chapter further develops some of these concepts and paves the way for their application to composite marine propellers.

First, this chapter assesses the accuracy of a dispersion compensation technique based on Fourier-domain signal processing, for reconstruction of AE waveforms in FRP materials. The accuracy has been evaluated by comparison using measurement data. By considering numerical simulations through 3D transient Spectral Element Model (SEM) and experimental measurements, the error originating from the reconstruction method can be distinguished from the error due to uncertainties in the experimental setup and the assumed material properties.

Furthermore, this chapter experimentally investigates AE localization using TDDM when multiple wave modes are present in the measurement. To do so, artificial AE with varying frequency content has been excited in a 10.2mm thick glass-fiber reinforced plastic panel. This excitation has been measured by a sensor that was at a known distance from the source. Dispersion characteristics of multiple wave modes have been used in the assessment. Localizations using individual wave modes and combinations of wave modes have been compared.

The structure of the chapter is as follows: Firstly, the mathematical procedures are described for acoustic emission signal reconstruction and multimodal localisation. This is followed by an explanation of the performed experiments and simulations. Secondly, results from the measurements and assessments are presented. Lastly, conclusions and an outlook on future research are presented.

5.2 METHODOLOGY

The degradation of material is often accompanied by the generation of AE. These are typically measured at a location away from the location of material degradation. Hence, the measured AE is subject to wave propagation effects. In the case of plate-like structures, the AE propagates in the form of guided waves. In the frequency domain, the relation between AE source and measurement can be cast into Equation 5.1 [126]:

$$P(\mathbf{x}_R, \mathbf{x}_S, \omega) = \sum_{i=1}^{n} D_i(\mathbf{x}_R, \omega) W_i(\mathbf{x}_R, \mathbf{x}_S, \omega) \varsigma_i(\mathbf{x}_S) S(\mathbf{x}_S, \omega) + P_N(\mathbf{x}_R, \omega)$$

(5.1)

Here, the source location is denoted by $\mathbf{x}_S$, the measurement location by $\mathbf{x}_R$ and the angular frequency by ω. The AE source signal $\varsigma_i(\mathbf{x}_S)S(\mathbf{x}_S,\omega)$ is convolved with wave propagation $W_i(\mathbf{x}_R,\mathbf{x}_S,\omega)$ and sensor electromechanical transfer $D_i(\mathbf{x}_R,\omega)$. Remark that the source and transfer functions are generally dependent on the wave mode i. In thick panels a multitude of modes may be supported. Measurement noise is denoted by $P_N(\mathbf{x}_R,\omega)$. The outcome is measurement signal $P(\mathbf{x}_R,\mathbf{x}_S,\omega)$. In the current context, the noise level is considered negligible and the sensor transfer function is assumed constant over frequency and wave mode. Wave propagation transfer $W_i(\mathbf{x}_R,\mathbf{x}_S,\omega)$ in an anisotropic medium can be described as in Equation 5.2:

$$W_i(\mathbf{x}_R,\mathbf{x}_S,\omega) = \alpha_i(\mathbf{x}_R,\mathbf{x}_S,\omega)e^{jk_i(\mathbf{x}_R,\mathbf{x}_S,\omega)x} \tag{5.2}$$

In this equation, $\alpha_i(\mathbf{x}_R,\mathbf{x}_S,\omega)$ is a scaling factor that includes attenuation effects due to radiation, damping and skewing. Change in signal phase and arrival time is covered by the exponential term. Here, angular wavenumber $k_i(\mathbf{x}_R,\mathbf{x}_S,\omega)$ is direction-dependent, and defined for the direction of $(\mathbf{x}_R-\mathbf{x}_S)/\|\mathbf{x}_R-\mathbf{x}_S\|$. Through this direction-dependent wavenumber definition, material anisotropy is accounted for in this approach.

In the case of dispersion compensation assuming single wave mode i, for every frequency a phase correction is applied using $W_i^{-1}(\mathbf{x}_R,\mathbf{x}_S,\omega)$ given the corresponding distances from $\mathbf{x}_R$ to $\mathbf{x}_S$ and wavenumbers $k_i(\mathbf{x}_R,\mathbf{x}_S,\omega)$. The resulting corrected signal $R_i(\mathbf{x}_S,\mathbf{x}_R,\omega)$ is shown in Equation 5.3.

$$R_i(\mathbf{x}_S,\mathbf{x}_R,\omega) = W_i^{-1}(\mathbf{x}_R,\mathbf{x}_S,\omega)P(\mathbf{x}_R,\mathbf{x}_S,\omega) \tag{5.3}$$

Back in the time domain, dispersion corrected signals $r_i(\mathbf{x}_S,\mathbf{x}_R,t)$ are obtained (Equation 5.4).

$$r_i(\mathbf{x}_S,\mathbf{x}_R,t) = \frac{1}{2\pi}\int_{-\infty}^{\infty} R_i(\mathbf{x}_S,\mathbf{x}_R,\omega)e^{i\omega t}d\omega \tag{5.4}$$

5.2.1 Waveform Similarity

To evaluate the accuracy of the reconstruction, a comparison is made between reconstructions $r_i(\mathbf{x}_B,\mathbf{x}_S,\mathbf{x}_R,t)$ towards location $\mathbf{x}_B$ close to the emission source and the direct measurement at that location $p(\mathbf{x}_B,\mathbf{x}_S,t)$. It is recognised that in direct reconstruction from $\mathbf{x}_R$ to $\mathbf{x}_B$, a discrepancy in trajectory from measurement $\mathbf{x}_R$ to source $\mathbf{x}_S$ and to reference $\mathbf{x}_B$ would exist. This is addressed by performing a reconstruction towards $\mathbf{x}_S$ and using the same method to perform a forward reconstruction from $\mathbf{x}_S$ to $\mathbf{x}_B$. This is shown in Equation 5.5 and in Figure 5.1.

$$R_i(\mathbf{x}_B,\mathbf{x}_S,\mathbf{x}_R,\omega) = W_i(\mathbf{x}_B,\mathbf{x}_S,\omega)R_i(\mathbf{x}_S,\mathbf{x}_R,\omega) \tag{5.5}$$

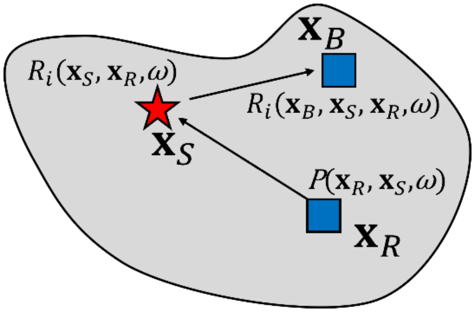

Figure 5.1. Illustration of the reconstruction procedure from measurement to source to reference measurement.

Comparison between $r_i(\mathbf{x}_B, \mathbf{x}_S, \mathbf{x}_R, t)$ and $p(\mathbf{x}_B, \mathbf{x}_S, t)$ is done via waveform similarity. Note that in the method of Equation 5.4, no correction for attenuation is considered. A normalised waveform similarity as described in Equation 5.6 is used for each single reconstructed signal $r_i(\mathbf{x}_B, \mathbf{x}_S, \mathbf{x}_R, t)$.

$$Similarity_i(\mathbf{x}_B, \mathbf{x}_S, \mathbf{x}_R, \omega) = \max\left(\frac{\left(r_i(\mathbf{x}_B, \mathbf{x}_S, \mathbf{x}_R, t) \star p(\mathbf{x}_B, \mathbf{x}_S, t)\right)(\tau)}{\sqrt{\left(r_i(\mathbf{x}_B, \mathbf{x}_S, \mathbf{x}_R, t) \star r_i(\mathbf{x}_B, \mathbf{x}_S, \mathbf{x}_R, t)\right)(\tau_0)\left(p(\mathbf{x}_B, \mathbf{x}_S, t) \star p(\mathbf{x}_B, \mathbf{x}_S, t)\right)(\tau_0)}}\right) \tag{5.6}$$

The five-pointed star ⋆ indicates cross-correlation and τ indicates lag (with τ_0=0). Time delay is defined as the argument of the maximum similarity value. This is then divided by the period related to the centre frequency of the input signal to get a normalised time delay. Note that the similarity values are relevant for waveform clustering, while time delay is an indication of localisation error.

5.2.2 Multimodal Acoustic Emission Localization

This research employs $W_i(\mathbf{x}_R, \mathbf{x}_S, \omega)$ to investigate the extent of multimodality in a measurement and to localize the source of the AE by accounting for this multimodality. The modal contribution, or extent of multimodality $\alpha_i(\mathbf{x}_R, \mathbf{x}_S, \omega)\varsigma_i(\mathbf{x}_S, \omega)$ can be assessed through comparison of $P(\mathbf{x}_R, \mathbf{x}_S, \omega)$ with $P^*(\mathbf{x}_R, \mathbf{x}_S, \omega)$ in Equation 5.7.

$$P^*(\mathbf{x}_R, \mathbf{x}_S, \omega) = \sum_{i=1}^{n} \alpha_i(\mathbf{x}_R, \mathbf{x}_S, \omega)\varsigma_i(\mathbf{x}_S) S(\mathbf{x}_S, \omega) e^{jk_i(\mathbf{x}_R, \mathbf{x}_S, \omega)x} \tag{5.7}$$

Here the source excitation $S(\mathbf{x}_S, \omega)$, measurement $P(\mathbf{x}_R, \mathbf{x}_S, \omega)$, dispersion relationship $k_i(\mathbf{x}_R, \mathbf{x}_S, \omega)$ and distance x are considered known. Single-mode localization is performed using TDDM as was described by Wilcox [139]. This involves back-propagation as per Equation 5.8:

$$R_i(\mathbf{x}_R, \mathbf{x}_S, \omega) = P(\mathbf{x}_R, \mathbf{x}_S, \omega)e^{-jk_i(\mathbf{x}_R, \mathbf{x}_S, \omega)x} \tag{5.8}$$

In order to evaluate Equation 4 in distance domain using the inverse Fourier transform, the right-hand side needs to be mapped from frequency domain to wavenumber domain. That is done using the group velocity $c_{gi}(\mathbf{x}_R, \mathbf{x}_S, \omega)$ as in Equation 5.9:

$$h_i(x) = \int_{-\infty}^{\infty} R_i(\mathbf{x}_R, \mathbf{x}_S, \omega(k_i(\mathbf{x}_R, \mathbf{x}_S)))d\omega(k_i(\mathbf{x}_R, \mathbf{x}_S)) =$$
$$\int_{-\infty}^{\infty} R_i(\mathbf{x}_R, \mathbf{x}_S, \omega(k_i(\mathbf{x}_R, \mathbf{x}_S)))c_{gi}(\mathbf{x}_R, \mathbf{x}_S, \omega(k_i(\mathbf{x}_R, \mathbf{x}_S)))dk_i(\mathbf{x}_R, \mathbf{x}_S)$$
(5.9)

Here, distance domain reconstruction $h_i(x)$ is a measure of the distance travelled by a signal from the starting time of the measurement to the time of registration of the signal. The back-propagation compensates for dispersion. This implies that the wave mode that is present in the signal appears in the distance domain as relatively compressed and with relative higher amplitude than in the time domain [149,150]. This is the feature that is used for localisation. It is remarked that for such localisation the starting or onset time of the measurement should relate to the peak time of the source signal. In the case of measuring AE, this peak time of the source signal is unknown. Grabowski et al. [148] solved this by iteratively searching for the starting time that gave the most compressed back-propagation. In the current work, the starting time is not investigated and is considered known.

It is considered that a measurement signal contains contributions of a multitude of modes. The reconstruction using wave mode i will compress and amplify the contribution of that wave mode at the source location. However, the contributions of the other wave modes $j \neq i$ are also affected by the back-propagation. This means that artificial peaks can exist at locations that are different than the source location.

The multimodal localisation approach presented in this section proposes to improve localisation by summation of reconstructions from a multitude of wave modes. Hilbert transform envelopes are used to largely exclude phase differences between the reconstructions. The summation can mitigate the severity of artificial peaks. This is because the contribution of mode i using reconstruction $h_i(x)$ will be at the same location for $i = 1..n$ whereas the artificial peaks are unlikely to be at the same location for $i = 1..n$. The approach is schematically visualised in Figure 5.2.

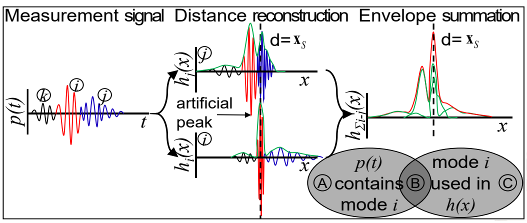

Figure 5.2: Schematic representation of localization using multimodal TDDM.

In the choice of wave modes to consider for localization, three options exist: The wave mode is present in the measurement, but not used for localization (A); The wave mode is present in the measurement, and used for localization (B); The wave mode is not present in the measurement, but is used for localization (C). The three options can be summarized in the Venn-diagram of Figure 5.2. All options are assessed.

5.2.3 Reconstruction simulation using 3D SEM

In order to assess the reconstruction method without experiment-related biases, a simulated measurement dataset was generated. The simulation came in the form of a transient linear elastic spectral element analysis (SEM). SEM is frequently used in time domain guided wave simulations [151]. In SEM, field variables are approximated using higher-order polynomial basis functions. These basis functions allow for a higher convergence rate compared to traditional finite element methods [152]. In the case of Legendre-Gauss-Lobatto-Lagrange (LGL) polynomials the mass matrix becomes diagonal, reducing the number of operations in the time integration process [133,152].

The simulation was performed on a model that has close similarities to the experiment described in the following section. The SEM was developed in-house as a set of MATLAB codes and functions [133]. The domain considered in the simulation is a GFRP unidirectional laminate with anisotropic properties given in Table 5.1. The domain had length, width and thickness dimensions of 600mm, 600mm and 10.2mm. The domain consisted of 900 elements with 20mm length and width and fourth-order LGL polynomials. In the thickness direction, the elements had a size of 10.2mm and were of fourth-order as well. These values are based on a mesh convergence study. A 1N amplitude five-cycle Hanning-windowed pulse with a centre frequency of 40kHz was excited at a location 250mm away from the edges of the domain. This location and the waveform is in agreement with the experiment. Regarding the amplitude, the simulation uses linear elasticity, resulting in the force amplitude being essentially a scaling factor. 1N was chosen for its generality and simplicity. The excitation was given in the out-of-plane direction. The propagated wave was measured on a grid of 100×100mm, with a spacing of 20mm. In Figure 5.3, the domain and a snapshot of the propagating wave can be seen.

Table 5.1. Lamina material properties used in the 3D SEM simulation and for reconstruction of the experimental data.

E_x (GPa)	E_y=E_z (GPa)	G_{xy}=G_{xz} (GPa)	G_{yz} (GPa)	ν_{xy}=ν_{xz} (GPa)	ν_{yz} (GPa)	ρ (kg/m^3)
46.2	13.1	4.1	5.1	0.29	0.28	1872

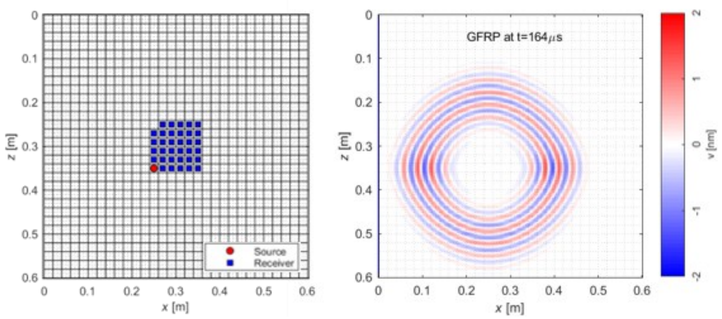

Figure 5.3: Discretisation of a GFRP plate. The left Figure shows the domain, with mesh and integration points given in black lines and dots. The right Figure shows the vertical motion of the simulated unidirectional GFRP plate that has been excited in the out-of-plane direction with a five cycle burst with 40kHz centre frequency.

5.2.4 Experimental procedure for *waveform similarity assessment*

To test the signal reconstruction method in a more realistic environment, experiments have been performed in a manner similar to the simulation. In this situation, the reconstruction is additionally subject to discrepancies such as variation in material properties over location and damping effects. The experiment as such can be seen as a measure of robustness in a reasonably realistic context.

The setup is shown in Figure 5.4 and follows the subsequent order: an actuator (denoted by ‘a’ and of the type VS600-Z1) emits an artificial signal that is generated by an arbitrary waveform generator (1, Siglent SDG10251) and that is amplified (2, Falco WMA-300) with 34dB. This signal propagates as a guided wave through a thick GFRP panel (3) and is measured by both a reference sensor (b) and a measurement sensor (c). Both measurements are amplified (5, Vallen AEP5H) with 40dB and recorded by a data acquisition system (6, Vallen AMSY-6). The signals are then stored on a measurement laptop (7).

The GFRP panel is made from E-glass fibres with a vinyl ester resin. The panel has anisotropic properties, with a $[0_5,90_5]_s$ laminate layup and has a total thickness of 10.2mm [153]. Material properties that are used for reconstruction are stated in Table 5.1. The resin infusion manufacturing process is generally less precise than for example the use of prepreg, hence deviation of material properties, such as local stiffness due to difference in fibre volume fraction or voids may be expected.

The actuator and reference sensor (a & b) are coupled to the panel by means of hot-melt adhesive. This ensures that the transmission of the emitted signal is not altered over time. Measurement sensor (c) is positioned and repositioned on a grid of 100mm×100mm, with a spacing of 20mm. Using the same sensor for each location prevents variation in measurements due to variation in sensor properties. As a coupling agent, medical ultrasonic gel is applied between the test panel and the measurement sensor. Constant pressure on the measurement sensor is provided by a weight (4).

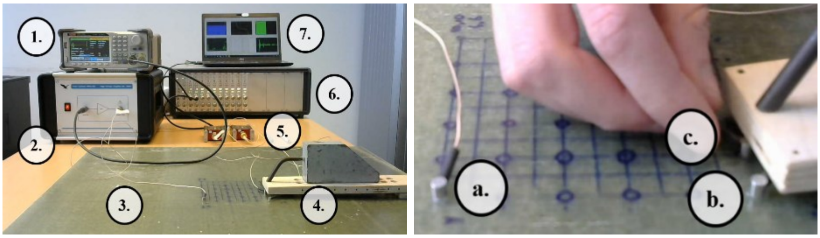

Figure 5.4: Experimental setup: The left Figure shows a general overview and the right Figure is a close-up. Numbers 1-7 relate to the Siglent SDG10251 waveform generator, Falco WMA-300 amplifier, test specimen, measurement sensor fixture, Vallen AEP5H preamplifiers, Vallen AMSY-6 data acquisition system and measurement laptop, respectively. Letters a-c denote the actuator, reference sensor and measurement sensor. All transducers are of the VS600-Z1 type.

The source signal *S* emitted by the waveform generator is a five-cycle Hanning-windowed sine wave with a centroid frequency of 40kHz. The signal is shown in Figure 5.5 in time and frequency domains. The limited amount of cycles and associated short duration of the signal allows for measurements to be minimally influenced by interference patterns. Further, a band of frequencies is excited that will introduce dispersive effects in the measurements. As the measurement sensor is repositioned during the experiments, the source signal is emitted repeatedly.

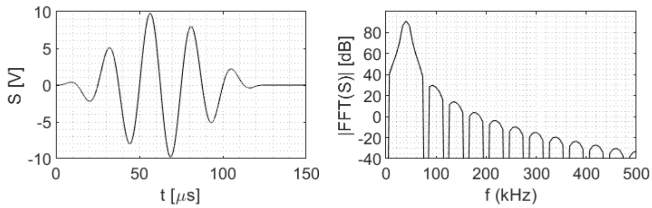

Figure 5.5: Source signal S in time domain (left Figure) and frequency domain (right Figure).

The measurement by the reference and measurement sensors is based on full-waveform capture. The signals were recorded using hit definition, keeping a 50dB threshold. Sampling frequency for the waveform was 5MHz. A digital band-pass filter was applied, ranging from 25kHz to 850kHz. Total duration of the recording of the waveform was 1638.4µs, including 200µs pretrigger time. Rearm time (hit lockout time) and duration discrimination time (hit definition time) were chosen to be 250µs.

5.2.5 Experimental procedure for multimodal localisation assessment

Furthermore, in order to investigate the feasibility of the multimodal localization approach, experiments have been performed on a thick glass-fiber reinforced polymer (GFRP) panel. The panel was instrumented with an actuator that generated a simulated AE signal, and a sensor that recorded the propagated AE. The actuator and sensor were both of the type VS600-Z1. They were coupled to the panel using ultrasonic gel and held in place using spline weights. The actuation signal was generated by an arbitrary waveform generator (Siglent SDG10251). This signal was directed to a power amplifier (Falco WMA-300, 34dB amplification) and to the data acquisition system (Vallen AMSY-6). The latter enabled direct assessment of the source signal peak time. From the power amplifier, the signal was conducted to the actuator. The sensor signal was amplified (Vallen AEPH5H, 40dB amplification) and recorded by the data acquisition system. A photograph of the set-up is shown with annotations in Figure 5.6.

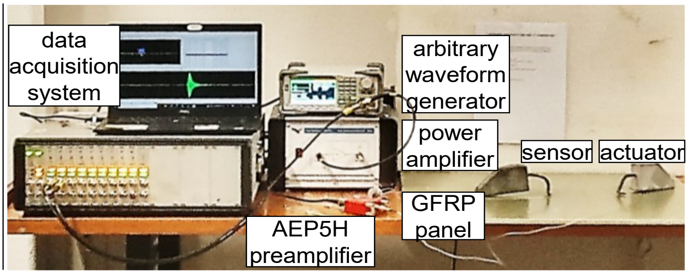

Figure 5.6: Schematic representation of localization using multimodal TDDM.

Property	Value
Modulus E_1, E_2= E_3 [GPa]	35.7, 10
Modulus G_{21} [Gpa]	2.8
Poisson's ratio ν_{21}, ν_{12}, ν_{32} [-]	0.325, 0.091, 0.35
Density ρ [kg/m^3]	1800

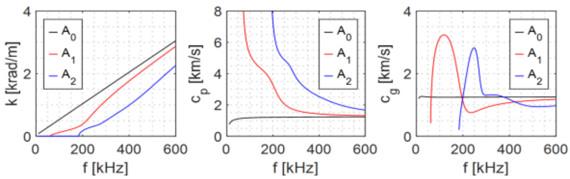

Figure 5.7: Material properties [154] *and selected antisymmetric dispersion curves.*

The GFRP panel had a 600mm length and width, was 10.2mm thick and had a $[0_5\ 90_5]_s$ lay-up, making it a panel with anisotropic properties. It was made of 640g/m^2 U-E glass from Saertex with an Atlac E-nova MA 6215 vinyl ester resin. Ambient-temperature vacuum-assisted resin transfer moulding was used. The panel was considered to have material properties similar to those used by Samaitis and Mažeika [154], and are shown in Figure 5.7. From these properties, dispersion curves have been calculated using a semi-analytical finite element method. In the localization procedure only antisymmetric modes (A_0, A_1, A_2) are used. This is because the actuator is placed on the surface of the panel. This promotes antisymmetric motion. The dispersion curves can be seen in Figure 5.7 for the 0˚ direction.

The data acquisition system recorded the signals in a hit-based manner, saving full waveforms with a 20MHz sampling frequency. A static threshold of 45dB was applied, based on the ambient noise level. This was complemented with a digital filter ranging from 20kHz to 960kHz. Rearm time and duration discretization time were set at 400µs and the pretrigger time at 500µs.

For actuation, a Hann-windowed sine function was used. Two signals were tested: one with 200kHz center frequency and four cycles, and one with 300kHz center frequency and six cycles. The actuator was placed in the center of the panel and the sensor was placed at distances of 75mm and 150mm away from the actuator in the 0˚ direction.

5.3 RESULTS AND DISCUSSION

5.3.1 AE signal source reconstruction results

Based on the simulation and mathematical procedure described in Section 5.2.1 and Section 5.2.3, similarity is assessed between the measurements at location (20,80)mm close to the source and reconstructions based on measurements at the other locations. In the simulation, the prescribed motion was in out-of-plane direction. Based on this, the reconstruction procedure adopted a dispersion curve related to the antisymmetric wavemode. In Figure 5.8, the similarity index described in Equation 5.6 is shown on the left. The normalised time lag is given on the right. In Figure 5.9, a comparison over time is made between the measurement at (20,80)mm and reconstructions at selected other locations.

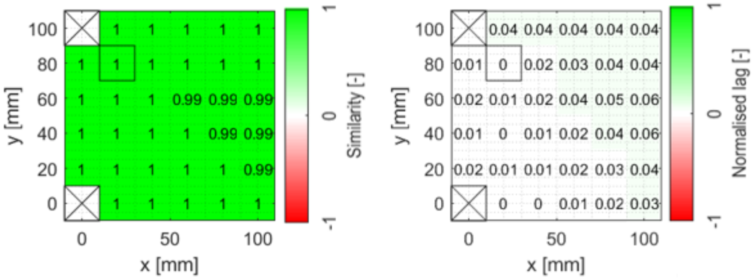

Figure 5.8: Comparison between simulated response in out-of-plane direction v[nm] at location (20,80)mm and reconstructions from measurements at other locations towards this location. The left Figure shows the Similarity index between the measurement and the reconstructions. The right Figure shows the lag relative to a period in the signal (1/(40kHz)).

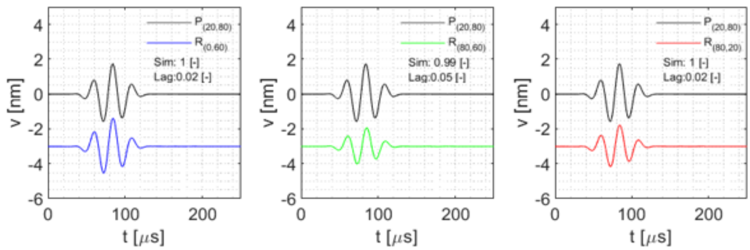

Figure 5.9: Three graphs with comparison between a measurement P and individual reconstruction R. The similarity index is denoted by 'Sim' and the normalised lag by 'Lag'.

The Figures present that the original measurement and reconstructions are near identical in shape and time delay. The minor deviations are considered to be coming from contributions from other wavemodes or from effects related to differences between SEM through-thickness discretisation and the semi-analytical reconstruction. In general, the results demonstrate that the reconstruction procedure can give viable outcomes.

After assessment of the similarity in simulation, experimental results on reconstruction and similarity are given, based on Section 5.2.4. The experiment makes use of the repositioning of the measurement sensor. Actuation therefore is repeated over time. Similarity-based time picking on the measurements of the reference sensor has been used to correct for the different location of the measurement sensor. This ascertains that the measurements are assessed with a correct time delay with respect to the source. In Figure 5.10, corrected measurements are shown for four emission repetitions per sensor position.

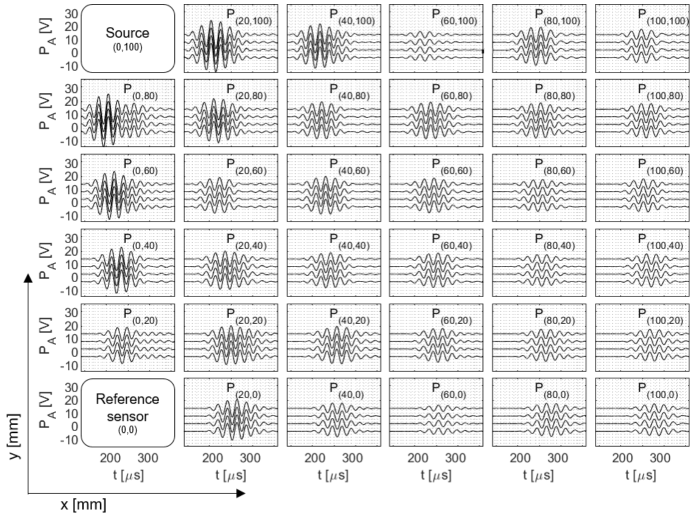

Figure 5.10: Waveforms P(i,j) in voltage over time measured by the sensor at location (x,y)=(i,j) from the reference. Note the monotonic delay in time away from the source and the phase of the signal varying over location.

The graphs show that the measurements are repeatable and that the time delay is consistent. In the experiment, the excitation was applied only on the top face of the panel. For that reason, antisymmetric wave motion is considered in the reconstruction. Similar to the assessment of the simulated data, comparison is made between the measurement at location (20,80)mm and reconstructions from other locations towards this location. The comparison is visualised in Figure 5.11 and Figure 5.12.

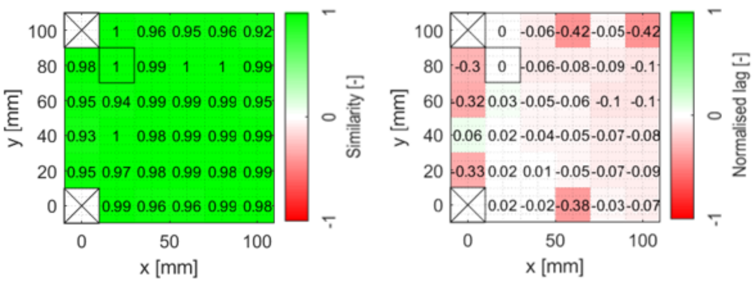

Figure 5.11: Comparison between experimental measurement in voltage amplitude PA [V] at location (20,80)mm and reconstructions from measurements at other locations towards this location. The left Figure shows the Similarity index between the measurement and the reconstructions. The right Figure shows the lag relative to a period in the signal (1/(40kHz)).

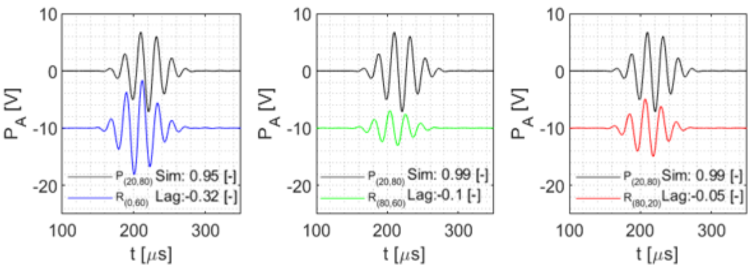

Figure 5.12: Three graphs with comparison between a measurement P and individual reconstruction R. The similarity index is denoted by 'Sim' and the normalised lag by 'Lag'.

From the results it appears that the reconstruction has slightly lower similarity values compared to the results from the simulation. The dissimilarity is generally less than 5%, therefore it is not expected to hinder the ability of the method for narrow-band source signal reconstruction. Further, the normalised lags show deviation in time delay between the reconstructions and the measurement. For the current reconstruction and future characterisation this is not problematic. It is expected that a discrepancy in dispersion curves is the main cause and for improved assessment a more thorough assessment of geometry and material properties is advised. It is recognised that this research should be extended towards a variation of source signals, covering different frequency ranges and bandwidth for mimicking AE [103]. Furthermore, the assessment has been performed with known onset time and single assumed wave mode. In the next section, results for a related localisation methodology are presented that does not assume a single wave mode. Also a related method for onset time picking is given.

5.3.2 Localisation Results

For the localisation results, based on Section 5.2.2 and Section 5.2.5, the experimental data is analysed in the following manner: Firstly, each measurement signal of the receiver sensor is assessed for their content in wave modes. This gives improved insight when discussing the localization results. Secondly, the signals are reconstructed in the distance domain representation for each wave mode separately. The distance value at the peak of the envelope of these reconstructions are estimates of the source location when considering a single mode. Thirdly, the envelopes are combined for a multimodal localization. Different combinations are assessed. Fourthly, localization errors are provided and assessed.

The contribution of the different wave modes present in the receiver sensor measurement signal is investigated. To do so, the emitted source $s(\mathbf{x}_S,t)$ was extrapolated forward in time using Equation 5.7. The results are propagated signals for the individual wave modes towards the location of measurement. The dispersion curves for the first three antisymmetric modes (Figure 5.6) were used. For a 300kHz center frequency signal at a distance of 150mm, the results are visualized in the first two graphs in Figure 5.13.

After the extrapolated signals $p_i^*(\mathbf{x}_R,\mathbf{x}_S,t)$ for the individual wave modes have been obtained, it was now possible to relate these to the signal that was actually measured ($p(\mathbf{x}_R,\mathbf{x}_S,t)$).This was done through assigning a contribution factor $\alpha_i\varsigma_i$ to each extrapolation and then summing the extrapolations ($\sum_i \alpha_i \varsigma_i p_i^*(\mathbf{x}_R, \mathbf{x}_S, t)$). Values for $\alpha_i \varsigma_i$ were approximated through matching the amplitudes between $\sum_i \alpha_i \varsigma_i p_i^*(\mathbf{x}_R, \mathbf{x}_S, t)$ and $p(\mathbf{x}_R, \mathbf{x}_S, t)$. The results are pictured in the right graphs of Figure 5.13. Table 5.2 provides the values for each source-receiver distance and center frequency. In the table, it may be seen that for the 200kHz center frequency cases, there appears to be no contribution of mode A_2. This enables assessment of localization in the case of situation 3 defined in the Venn diagram in Figure 5.2 (i.e. a mode is used in the reconstruction that is not present in the original signal). In the other measurements, it is apparent that there is a more balanced contribution of each mode. Note that in the current measurement frequency range, mode A_0 is relatively non-dispersive and has the largest contribution in terms of amplitude. This is especially the case with the 200kHz center frequency measurements.

The signals measured by the receiver sensor were reconstructed through TDDM as per Equation 5.9. The starting time of the excitation was considered known and was calculated directly from the excitation signal. In Figure 5.14, the distance domain results per individual mode $h_i(\mathbf{x}_R, \mathbf{x}_S, x)$ are shown together with their respective envelopes. The fourth graph visualizes the summation of the three reconstructions $\sum_i h_i(\mathbf{x}_R, \mathbf{x}_S, x)$ and the summation of the individual envelopes. From the Figure, it may be seen that the envelopes of the individual reconstructions show several peaks. In the cases of wave mode A_0 and A_2, the largest peaks are around the source location (x=150mm) while in A_1, the largest peak is at a smaller distance. Smaller secondary peaks are present as well. The locations of these peaks can be explained through the dispersion curves in Figure 5.6. Mode A_0 around 300kHz is almost nondispersive. Hence the reconstruction is similar to the measurement signal. The largest amplitude of the signal is provided by A_0, and therefore the localization peak for A_0 is at the source location. For A_1, the group velocity is lower than that of A_0. Also it is not very dispersive. This implies that when reconstructing with A_1, the peak in the signal that corresponds to A_0 is localized at a shorter distance than the source location distance. Note also that this peak is higher and the reconstruction contains less lobes than when reconstructing with A_0. This implies that reconstruction of the A_0 component using A_1 dispersion creates artificial focusing. However, there is furthermore a secondary peak, relating to the A_1 contribution, that is correctly localizing around the source location. Wave mode A_2 has strong dispersive characteristics around 300kHz. In the reconstruction for A_2 this becomes visible as a strong 'tail' between 200mm and 400mm.

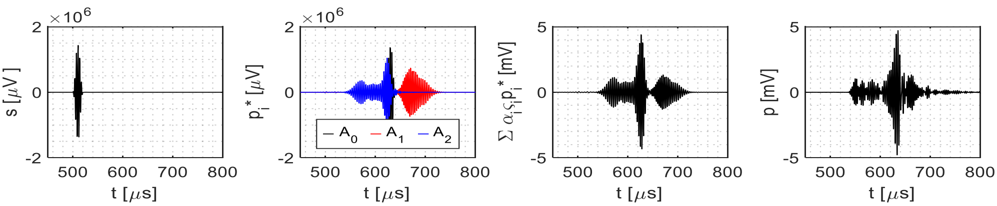

Figure 5.13: Measurement of a wave excitation and evaluation of multimodality.

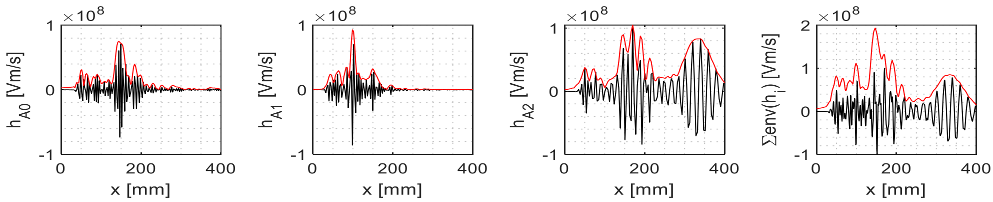

Figure 5.14: Distance domain reconstructions per individual mode and the summation.

Table 5.2: Time-distance domain localisation error

$\|\|\alpha_i\varsigma_i\|\|$ [%]					εd_i [mm]					$\varepsilon d_{\Sigma i}$ [mm]				
x [mm]	75		150			75		150			75		150	
f_c [kHz]	200	300	200	300		200	300	200	300		200	300	200	300
$\|\|\alpha_0\varsigma_0\|\|$	55	48	59	23	εd_0	6	3	2	-6	$\varepsilon d_{\Sigma 01}$	-22	-3	-53	-1
$\|\|\alpha_1\varsigma_1\|\|$	45	30	41	28	εd_1	-24	-27	-51	-51	$\varepsilon d_{\Sigma 12}$	94*	-3^{+}	176*	-3^{+}
$\|\|\alpha_2\varsigma_2\|\|$	0	22	0	49	εd_2	91*	33	178*	20	$\varepsilon d_{\Sigma 012}$	25*	-4	173*	-3

This tail is likely coming from the contribution of A_0 that is now strongly (inversely) dispersed. Note that for A_2, the maximum peak is around the source location. This is indicative of correct reconstruction of the A_2 contribution. The combination of reconstructions, shown in the bottom right graph, appears to not give a satisfactory reconstruction of the source signal. This is mainly attributed to slight variations between the used dispersion curves and the actual material. This causes phases to be slightly misaligned. The combination of envelopes nevertheless is not adversely affected by this issue and the peak at the source location stands out.

Values of the envelope peak location have been assessed for a 200kHz and a 300kHz signal, measured at 75mm and 150mm. The errors between the estimated and true location are given in Table 5.2. In Table 5.2, εd_i denotes envelope peak location error using wave mode i. Similarly $\varepsilon d_{\Sigma ijk}$ describes peak location error for the combination of envelopes for wave modes i, j and k. Values with an asterisk (*) relate to the third region in the Venn diagram of Figure 5.2, while plusses (+) relate to the first region.

In all cases, reconstruction with A_0 gives a low error εd_0 amounting to 1.3% to 8% of the distance. This is considered reasonable, because the A_0 has the largest amplitude component and is nondispersive. Reconstruction with A_1 in all situation gives an erroneous result. This is due to the lower contribution of A_1 and that the dispersion curve for A_1 tends to artificially focus the A_0 contribution. For reconstruction with A_2, the 200kHz signal is not properly localized. This is because there is no A_2 component in the original signal (the third region in the Venn-diagram of Figure 5.2). At 300kHz, the localization is improved, but still with low precision. This may partly be attributed to small variations between modelled and actual material properties.

For combined results $\varepsilon d_{\Sigma i\text{-}k}$ it is clear that the 200kHz reconstruction remains biased by the reconstructions of εd_1 and εd_2 (29% to 125% error). For the 300kHz signal peak locations are close to the source location (2% to 5.3% error). The availability of the A_2 mode, and different dispersion behaviour of A_1, are the cause of this. In this respect, the case of $\varepsilon d_{\Sigma 12}$ is particularly interesting. Here localisation was performed without taking into account the accurate A_0 reconstruction (+ values, first region of Figure 5.2). Notwithstanding, the peak location has a small error with the source location. This implies that multimodal reconstructions can be better in localisation than using a single mode reconstruction.

For future research it is recommended to add the determination of onset time, as per for example Grabowski [148], since this will likely be affected by the multimodality.

5.4 CONCLUSIONS

This chapter assessed the use of dispersion compensation for AE source signal reconstruction and localisation.
Regarding signal reconstruction, simulations and experiments are performed involving thick GFRP laminates. The signal reconstruction on the simulated data, considering a narrow-band pulse, is reasonably similar to the simulated measurement. In the experimental case, similarity slightly drops. Deviation in arrival time between original measurement and reconstruction is attributed to a discrepancy in material properties in reality versus the properties used in the reconstruction.

Distance domain reconstruction is studied for multimodal localization of acoustic emissions in a GFRP panel. It has been found that in the situation of a known dominant wave mode, single mode reconstruction can give results with a reasonably small error (1.3% to 8%). Multimodal localization can give results with a small error (2% to 5.3%) when there is a balanced contribution of multiple wave modes. However it is prone to a larger error (29% to 125%) when there are few wave modes contributing to the received signal and one wave mode is dominant.

It is recommended for the future research to further investigate the influence of deviation in the material properties on the accuracy of the source reconstruction method. The effect of multimodality of guided waves on the quality of arrival time picking of the AE signals is to be investigated. Extension of the implementation from plates to more complex geometries will be a necessary next step.

Although the tests were performed on flat panels of anisotropic material, the methodologies that were tested have been developed for use in doubly curved thick composite surfaces. This is a first step where thickness and anisotropy were isolated from other complications such as curvature. In order to investigate their working in a preliminary sense, a simplified structure, with contact transducers, has been used that has representative thickness and anisotropy. The experiments can be seen as a verification study for the methodology, before testing on doubly-curved surfaces such as the propeller blade. Assessment on the propeller blade is underway, with extended methodology such as a wavenumber-frequency relation that is not only direction dependent, but also location dependent, to account for variations in thickness and lay-up.

6

CONCLUSIONS & RECOMMENDATIONS

6.1 CONCLUSIONS

In this thesis, research was performed regarding the embedding of piezoelectric sensors in composite marine propeller blades, for the purpose of structural health monitoring. This includes the measurement and assessment of acoustic emissions and low-frequency dynamic strains. A research question, to envelop the main investigations, was posed in the introduction and is repeated below:

How can a structural health monitoring system with embedded piezoelectric sensors be developed for composite marine propeller blades?

The research question has been subdivided into sub-questions. The conclusions in this chapter are structured such that they answer these sub-questions and thereby answer the main question.

The first research sub-question addressed the feasibility of embedding and measuring with piezoelectric sensors in composite marine propeller blades. An assortment of conclusions can be made for Chapters 2 to 4, relating to this sub-question. Carbon-fibre prepreg coupon specimens were manufactured with embedded piezoelectric sensors. They were loaded until failure using a four-point bending setup. During loading, it became clear that the embedded piezoelectric sensors could successfully measure acoustic emissions from composite degradation. Furthermore, finite element simulations were performed on the low-frequency (10-50Hz) strains of a composite marine propeller blade in the design operational conditions. It was shown that the embedded sensors can measure these strains, assuming typical values for electrical noise (0.1V) and measurement system impedance (1GΩ). In Chapter 4, a glass fibre composite propeller blade was manufactured with 24 embedded piezoelectric sensors, with 22 of these satisfactorily measuring acoustic emissions.

In practice, these measurements are subject to underwater radiated noise (URN). For the lower frequencies, the URN is associated with the blade passing motion. In that sense, the measurement of low-frequency strains is not expected to be hampered by the URN, as both URN and strains come predominantly from the same source. The URN shows a decreasing trend in amplitude (-6dB/octave) for higher frequencies [75]. At these higher frequencies, the noise is mostly related to cavitation implosion events. In theory, if measured, these URN events do not necessarily limit the measurement of damage-related acoustic emissions. This is under the premise that the waveform and localisation of the URN event is sufficiently distinct from those of damage-related acoustic emissions. Under this condition it may be concluded that it is feasible to perform structural health measurements in composite marine propeller blades using embedded piezoelectric sensors.

The second sub-question related to the extent of measuring acoustic emissions and low-frequency strains. Statements were made for the results of Chapters 2 to 4, building on the conclusions from the first sub-question. It was shown that the dynamic strains on the blade were sufficiently high on 92% of the blade area for measurement using embedded piezoelectric sensors. The four-point bending results show that the sensors embedded in carbon-fibre prepreg coupons can record acoustic emissions from types of failure such as matrix cracking, delamination and fibre breakage. These failure mechanisms were observed visually as well at the end of the experiments. The testing additionally showed that the sensors generally survived until near final failure of the specimens (maximum strain of the specimen was 15-20mε). Sensitivity to sensor geometry was assessed, with a 7mm diameter sensor showing higher amplitudes for frequencies above 300kHz compared to larger 20mm sensors. For the full-scale propeller blade, the measurable distance between acoustic emission source and sensor location was evaluated. The blade was suspended in salt water and at several locations acoustic emissions were simulated using pencil lead breaks. These were measured by the embedded sensors. It was found that in the case of acoustic emissions with 90dB amplitude, 100-250kHz centre frequency and a noise level of 40dB the measurable distance for the used embedded piezoelectric sensors was around 216mm. In the cases with lower source amplitude, higher frequencies, and more noise, the measurable distance dropped. These investigations have given insight into the extent and limitations of measuring acoustic emissions and low-frequency strains using embedded piezoelectric sensors in composite marine propeller blades.

The third research sub-question dealt with the influence of the embedded sensors on the structural integrity of the blade in Chapter 2. This influence was investigated for the carbon-prepreg coupon specimens using the four-point bending test till failure. Comparison was made between specimens with embedded sensors (7mm and 20mm diameter) and specimens without sensors. Furthermore, placement of the sensor in the coupon was assessed, with part of the specimens having the sensor region loaded under tension, and the other specimens loaded under compression. The influence on structural integrity was defined as the change in strength, maximum strain, and toughness. It was found that there was a limited influence of the embedded sensors on the maximum strain and toughness. In the test where the sensors were loaded compressively, the reduction in maximum strain and toughness had ranges between 9.3-20% and 19-34% respectively. For the specimens with the sensors on the tensile side, these values on average were 3.3% and 8.1% respectively.

The aforementioned results were performed on coupon scale, where the embedded sensor filled a non-negligible volume within the coupon. Regarding a full-scale propeller, this effect may be less pronounced due to the smaller sensor volume compared to blade volume. The results suggest that locations with stress concentrations should preferably be exempted from sensor embedment due to the adverse effects on structural integrity.

The fourth research sub-question related to analysis of acoustic emission measurement for the purpose of identification and localisation of damage. In the coupon experiments, the acoustic emission waveforms as measured through reference surface-mounted sensors were compared between specimens with embedded sensor to those without. Classification through waveform similarity gave clusters of waveforms that were broadly shared within specimens that had an embedded sensor, but not so in specimens without sensor. The proposed method may be used to distinguish between different sources of failure.

Both waveform similarity analysis and damage localisation procedures for acoustic emissions are influenced by distortions due to wave propagation effects. In Chapter 5, methodologies have been assessed that involve compensation of wave propagation effects. Firstly, assessment was made on an acoustic emission source signal reconstruction technique. This was done through excitation and measurement of acoustic emissions on a glass fibre composite plate. It was found that for narrow-band pulses (a 5-cycle Hann-windowed signal at 40kHz), signal reconstruction can give reasonable results, but there was also some inconsistency between the observed and reconstructed emission timing, likely caused by deviations between simulated and actual material properties of the glass fibre panel. Secondly, a localisation scheme was conceptualised and developed for wide-band acoustic emissions that have been measured after wave propagation through multiple guided wave modes. The method was assessed by excitation of acoustic emissions (200kHz and 300kHz centre frequency) on a thick glass fibre composite panel. Comparison was made between single wave mode localisation and the localisation using multiple modes, both making use of dispersion compensation. It was found that for localisation using multiple wave modes, localisation error was between 2% and 5.3% in the case that the measurement contained an even distribution of the considered wave modes (300kHz signal). In the case that a single wave mode was prevalent in the measurement (A0 mode for the 200kHz signal), multi-mode localisation gave erroneous results (29% to 125% error). This was due to the reconstruction of the dominant wave mode using another wave mode. Regarding single-mode localisation, when correctly assuming a prevalent wave mode, error was between 1.3% to 8%. These investigations highlight the potential and intricacies of using dispersion compensation for reconstruction and localisation of acoustic emissions.

The conclusions to the sub-questions above can be seen as an answer to the main question. Responding to the "*How*" in the main question, details were given on the way sensors are embedded, the methods used for analysis as well as confirmation and limitations of the working and analyses through experimental and numerical assessment.

6.2 FUTURE OUTLOOK AND RECOMMENDATIONS

The conclusions drawn above leave room for improvement and elaboration in future research. Recommendations include improvements on the presented methodologies, development of additional methodologies, and performing experiments that successively become closer to the envisioned real-world application.

Relating to the performance of experiments, the full-scale fatigue evaluation of a composite marine propeller blade is considered. An impression of this is given in Figure 6.1. This will provide insights into the fatigue life of the blade, and how it can be better assessed using measurements of acoustic emissions and low-frequency strains. Furthermore, degradation near sensor locations can be assessed. The information that may be obtained can be used for valorisation of the methods presented in this thesis. Next to this, with satisfactory results, the fatigue testing can serve as a stepping stone for the assessment of a composite propeller in sea trials. In preparation for these sea trials, engineering challenges will be tackled, such as data transmission through the rotating propeller, and the use of watertight connectors. During sea trials, there is further potential to measure and assess the amount of underwater radiated noise.

In order to use the sensors to their full potential, the methods for analysis need to be further developed. Details on the recommended developments were provided in the chapters above, but are also summarised here. Regarding the measurement of dynamic strains, a procedure needs to be developed for the reconstruction and extrapolation of the strain field using sensor voltage data. Initial investigations were conducted [74], but not completed. For the measurement of acoustic emissions, a method has been developed to localise sources of damage in thick composites. A composite marine propeller blade has a shape with varying geometry. This was not directly taken into account in the provided method. For future work, it is considered to include geometry changes in the localisation and verify its feasibility. The measurement of acoustic emissions and dynamic strains may be used as input for assessment of the propeller remaining lifetime. This can be combined with fatigue analyses such as those performed by Zhang [9], van Herwerden [12] and Patsantzopoulos [155]. Along these lines, it will be valuable to explore the development of a methodology for the relation between acoustic emissions and accumulated damage in the blade.

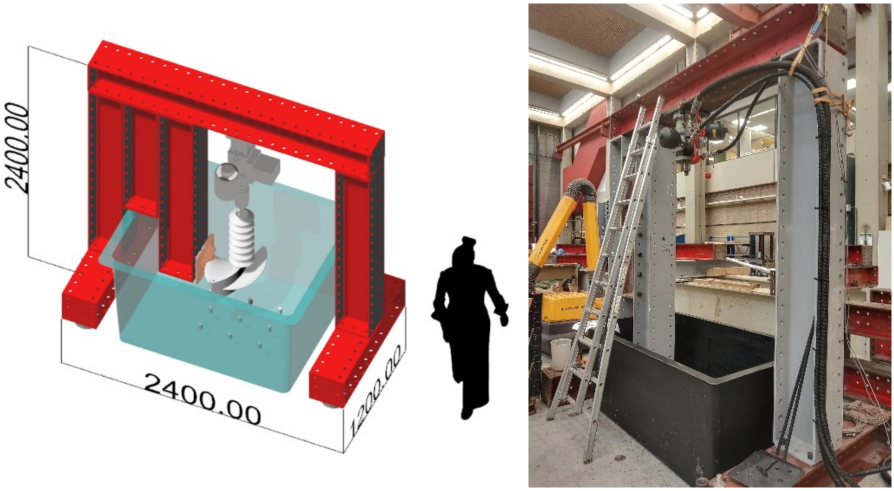

Figure 6.1: Full-scale fatigue testing of a composite marine propeller. On the left, an impression of the setup, with frame pieces in red, the actuator and blade in white and a water tank in blue. On the right, current status of the setup.

7

ACKNOWLEDGEMENTS

There are a number of people I'd like to acknowledge and/or show my gratitude to. They are listed below in an order that is roughly conventional for this type of work. Probably I am forgetting a few people, I hope it is not you that I am forgetting. If I forgot to acknowledge you, and you feel forgotten, please take this ❀ (flower) as a token of acknowledgement.

First and foremost, I'd like to acknowledge my supervisors, Pooria Pahlavan and Christos Kassapoglou. I feel deeply honoured to have been supervised by you. Next to the relevant professional discussions we had, I'd like to thank you both for the supportive and caring atmosphere you created. In this context I want to mention the conversations Pooria and I had on professional and personal matters. These allowed me to grow as a person in unforeseen directions.

Also I am grateful to the project partners of ECoProp and ViCS. With your keen eyesight and interesting points of view, you have helped me go further with the research.

The master students that I supervised have had me experience their personalities, working style and have been a general enrichment to my professional life. I have learned a lot from you and I thank you for that, and for accompanying me in this journey.

The research would not have been possible without the expertise and kind goodwill of the technicians of the various labs of TU Delft. Especially I'd like to mention Dave Ruijtenbeek and Victor Horbowiec of DASML, Fred Schilperoort and Jaap Elstgeest of Stevinlab, and Jasper, Ton, Frits and Pascal of the MTT towing tank.

My direct colleagues of the research group, Xiaobo, Bart, Sarjoon, Filippo, Sajad, Maarten, Cecilia and Romain, you have been vital in various ways. Thank you for that. You provided me with feedback, camaraderie, occasional food, support and interesting discussions. By the way, the same goes for many other colleagues and friends and friends from before, who I am not going to name all. Regarding my PhD time, I'd like to specifically mention Manuel and Wei Jun, for our adventures in sport and leisure, and also my paranymphs Menno and Pascal, for your support in tougher times and your considerate and critical thinking.

A special place is dedicated to Selina, who although recently entered my life, has been already an incredible lasting positive impact, and I hope to be so in her life as well.

Friends of my family, Tanja and Peter, I do not see or speak you often, but your advise and comfort has been decidedly important. Thank you for that.

At last I want to acknowledge my family. You provide the framework in which I have been able to thrive, be it in the form of advise, help, distraction, consolation, fun and rest.

8

REFERENCES

[1] Young Y L, Motley M R, Barber R, Chae E J and Garg N 2016 Adaptive composite marine propulsors and turbines: Progress and challenges *Appl. Mech. Rev.* **68**

[2] Maljaars P J, Grasso N, den Besten J H and Kaminski M L 2020 BEM–FEM coupling for the analysis of flexible propellers in non-uniform flows and validation with full-scale measurements *J. Fluids Struct.* **95**

[3] Young Y L, Chang J C, Smith S M, Venning J A, Pearce B W and Brandner P A 2022 The influence of fluid-structure interaction on cloud cavitation about a rigid and a flexible hydrofoil. Part 3 *J. Fluid Mech.* **934**

[4] Koko T S, Shahin K O, Akpan U O and Norwood M E 2012 Review of Composite Propeller Developments and Strategy for Modeling Composite Propellers using PVAST *Defece reshearch Dev. Canada* 1–46

[5] Maljaars P J 2019 *Hydro-elastic analysis of flexible marine propellers* (Delft University of Technology)

[6] van der Vliet J 2016 Model of a Propeller, c. 1855 - c. 1860

[7] Le Guen-Geffroy A, Le Gac P Y, Habert B and Davies P 2019 Long-term seawater ageing effect on fatigue crack growth of cfrp for marine propellers *ICCM International Conferences on Composite Materials* vol 2019-August (International Committee on Composite Materials)

[8] Vijayanandh R, Venkatesan K, Kumar M S, Kumar G R, Jagadeeshwaran P and Kumar R R 2020 Comparative fatigue life estimations of Marine Propeller by using FSI *Journal of Physics: Conference Series* vol 1473 (Institute of Physics Publishing)

[9] Zhang X 2021 *Short-term Structural Perfomance of Self-monitoring Composite Marine Propellers*

[10] Shamsuddoha M, Prusty G B, Maung P T, Phillips A W and St John N A 2022 Smart monitoring of a full-scale composite hydrofoil manufactured using automated fibre placement under high cycle fatigue *Smart Mater. Struct.* **31**

[11] Finnegan W, Jiang Y, Meier P, Hung L C, Fagan E, Wallace F, Glennon C, Flanagan M, Flanagan T and Goggins J 2022 Numerical modelling, manufacture and structural testing of a full-scale 1 MW tidal turbine blade *Ocean Eng.* **266** 112717

[12] Van Herwerden T 2023 *Fatigue Life Prediction of Composite Marine Propellers* (Delft)

[13] Garg N, Pearce B W, Brandner P A, Phillips A W, Martins J R R A and Young Y L 2019 Experimental investigation of a hydrofoil designed via hydrostructural optimization *J. Fluids Struct.* **84** 243–62

[14] Maljaars P, Bronswijk L, Windt J, Grasso N and Kaminski M 2018 Experimental Validation of Fluid–Structure Interaction Computations of Flexible Composite Propellers in Open Water Conditions Using BEM-FEM and RANS-FEM Methods *J. Mar. Sci. Eng.* **6**

[15] Giurgiutiu V 2008 *Structural Health Monitoring with Piezoelectric Wafer Active Sensors* (Academic Press)

[16] Frieden J, Cugnoni J, Botsis J, Gmür T and Corić D 2010 High-speed internal strain measurements in composite structures under dynamic load using embedded FBG sensors *Compos. Struct.* **92** 1905–12

[17] Mieloszyk M, Majewska K and Ostachowicz W 2021 Application of embedded fibre Bragg grating sensors for structural health monitoring of complex composite structures for marine applications *Mar. Struct.* **76** 102903

[18] Mall S, Dosedel S B and Holl M W 1996 The performance of graphite-epoxy composite with embedded optical fibers under compression *Smart Mater. Struct.* **5** 209–15

[19] Seaver M, Trickey S T and Nichols J M 2006 Strain measurements from FBGs embedded in rotating composite propeller blades *Optics InfoBase Conference Papers* (Optical Society of America (OSA)) p ThD2

[20] Javdani S, Fabian M, Carlton J S, Sun T and Grattan K T V 2016 Underwater Free-Vibration Analysis of Full-Scale Marine Propeller Using a Fiber Bragg Grating-Based Sensor System *IEEE Sens. J.* **16** 946–53

[21] Zetterlind V E, Watkins S E and Spoltman M W 2003 Fatigue testing of a composite propeller blade using fiber-optic strain sensors *IEEE Sens. J.* **3** 393–9

[22] Guo Z-S, Zhang J, Hu H and Guo X 2007 Structural health monitoring of composite wind blades by fiber bragg grating *Int. Conf. Smart Mater. Nanotechnol. Eng.* **6423** 64230I

[23] Tian J, Croaker P, Zhang Z and Hua H 2016 Dynamic strain measurements of marine propellers under non-uniform inflow *Journal of Physics: Conference Series* vol 744 (Institute of Physics Publishing) p 012094

[24] Ding G, Yan X, Gao X, Zhang Y and Jiang S 2022 Reconstruction of propeller deformation based on FBG sensor network *Ocean Eng.* **249**

[25] Maung P T, Prusty B G, Rajan G, Li E, Phillips A W and St John N A 2017 Distributed strain measurement using fibre optics in a high performance composite hydrofoil *ICCM International Conferences on Composite Materials* vol 2017-August (International Committee on Composite Materials)

[26] Seaver M, Trickey S T and Nichols J M Water tunnel tests of a composite propeller with embedded FBG *Conference Proceedings of the Society for Experimental Mechanics Series*

[27] Kirkby E, de Oliveira R, Michaud V and Månson J A 2011 Impact localisation with FBG for a self-healing carbon fibre composite structure *Compos. Struct.* **94** 8–14

[28] Ueda K and Umeda A 1998 Dynamic response of strain gages up to 300 kHz *Exp. Mech.* **38** 93–8

[29] Song G, Li H, Gajic B, Zhou W, Chen P and Gu H 2013 Wind turbine blade health monitoring with piezoceramic-based wireless sensor network *Int. J. Smart Nano Mater.* **4** 150–66

[30] Sullivan C J and Mueller T J 1999 Polyvinylidene fluoride film sensors for measurement of unsteady pressures on aerodynamic surfaces. Part I: Design, fabrication, calibration and demonstration *Exp. Fluids*

[31] Sullivan C J and Mueller T J 1999 Polyvinylidene fluoride film sensors for measurement of unsteady pressures on aerodynamic surfaces. Part II: Application to a small-scale marine propeller in spatially distorted mean flow *Exp. Fluids*

[32] Hamada R, Ogura T, Fujita S, Murayama H, Yamatogi T, Inoue T, Hayashi K, Takahara M, Goto K and Furukawa K 2023 Structural Health Monitoring of CFRP Propellers by Piezoelectric Line Sensors *Structural Health Monitoring* ed S Farhangdoust, A Guemes and F-K Chang (Stanford: DEStech Pub li ca tions, Inc. 439 North Duke Street Lan cas ter, Penn syl va nia 17602 U.S.A.) pp 408–16

[33] Shin S, Zamorano B and Elvin N 2016 Comparison of the electromechanical properties of embedded and surface-mounted piezoelectric transducers *J. Intell. Mater. Syst. Struct.* **27** 2837–50

[34] Lin B and Giurgiutiu V 2006 Modeling and testing of PZT and PVDF piezoelectric wafer active sensors *Smart Mater. Struct.* **15** 1085–93

[35] Gopalakrishnan S, Ruzzene M and Hanagud S 2011 *Computational Techniques for Structural Health Monitoring* (Springer London)

[36] Erturk A and Inman D J 2011 *Piezoelectric Energy Harvesting* (Wiley)

[37] Carrión J G, Frövel M, Pintado J M and Cabrerizo F 2008 Extensive characterization of the intrusiveness of fibre bragg grating sensors embedded in a carbon fibre reinforced polymer *Proc. 4th Eur. Work. Struct. Heal. Monit.* 810–7

[38] Masmoudi S, El Mahi A and Turki S 2016 Fatigue behaviour and structural health monitoring by acoustic emission of E-glass/epoxy laminates with piezoelectric implant *Appl. Acoust.* **108** 50–8

[39] Masmoudi S, El Mahi A, Turki S and El Guerjouma R 2012 Structural Health Monitoring of Smart Composite Material by Acoustic Emission *Acoustics 2012* ed S F d'Acoustique (Nantes, France)

[40] Dziendzikowski M, Kurnyta A, Dragan K, Klysz S and Leski A 2016 In situ Barely Visible Impact Damage detection and localization for composite structures using surface mounted and embedded PZT transducers: A comparative study *Mech. Syst. Signal Process.* **78** 91–106

[41] Yang B, Xuan F-Z, Jin P, Hu C, Xiao B, Li D, Xiang Y and Lei H 2018 Damage Localization in Composite Laminates by Building in PZT Wafer Transducers: A Comparative Study with Surface-Bonded PZT Strategy *Adv. Eng. Mater.* **21** 1801040

[42] Zamorano-Senderos B and Elvin N 2014 High-speed impact location detection on anisotropic composite panels using embedded piezoelectric sensors *J. Intell. Mater. Syst. Struct.* **25** 1921–36

[43] Osmont D L, Dupont M, Gouyon R, Lemistre M B and Balageas D L 2000 Piezoelectric transducer network for dual-mode (active/passive) detection, localization, and evaluation of impact damages in carbon/epoxy composite plates *Fifth European Conference on Smart Structures and Materials* ed P F Gobin and C M Friend (SPIE)

[44] Tang H Y, Winkelmann C, Lestari W and La Saponara V 2011 Composite structural health monitoring through use of embedded PZT sensors *J. Intell. Mater. Syst. Struct.* **22** 739–55

[45] Andreades C, Mahmoodi P and Ciampa F 2018 Characterisation of smart CFRP composites with embedded PZT transducers for nonlinear ultrasonic applications *Compos. Struct.* **206** 456–66

[46] Chilles J S, Croxford A and Bond I P 2015 Design of an embedded sensor, for improved structural performance *Smart Mater. Struct.* **24**

[47] Ghasemi-Nejhad M N, Russ R and Pourjalali S 2005 Manufacturing and Testing of Active Composite Panels with Embedded Piezoelectric Sensors and Actuators *J. Intell. Mater. Syst. Struct.* **16** 319–33

[48] Mall S 2002 Integrity of graphite/epoxy laminate embedded with piezoelectric sensor/actuator under monotonic and fatigue loads *Smart Mater. Struct.* **11** 527–33

[49] Mall S and Coleman J M 1998 Monotonic and fatigue loading behavior of quasi-isotropic graphite/epoxy laminate embedded with piezoelectric sensor *Smart Mater. Struct.* **7** 822–32

[50] Qing X P, Beard S J, Kumar A, Ooi T K and Chang F-K 2006 Built-in Sensor Network for Structural Health Monitoring of Composite Structure *J. Intell. Mater. Syst. Struct.* **18** 39–49

[51] Schulze R, Streit P, Fischer T, Tsapkolenko A, Heinrich M, Sborikas M, Kroll L, Gessner T and Wegener M Fiber-reinforced composite structures with embedded piezoelectric sensors *Proceedings of IEEE Sensors* vol 2014-Decem pp 1563–6

[52] Lampani L, Sarasini F, Tirillò J and Gaudenzi P 2018 Analysis of damage in composite laminates with embedded piezoelectric patches subjected to bending action *Compos. Struct.* **202** 935–42

[53] De Marchi L, Marzani A and Miniaci M 2013 A dispersion compensation procedure to extend pulse-echo defects location to irregular waveguides *NDT E Int.* **54** 115–22

[54] Zhao X, Gao H, Zhang G, Ayhan B, Yan F, Kwan C and Rose J L 2007 Active health monitoring of an aircraft wing with embedded piezoelectric sensor/actuator network: I. Defect detection, localization and growth monitoring *Smart Mater.*

Struct. **16** 1208–17

[55] Mei H and Giurgiutiu V 2019 Guided wave excitation and propagation in damped composite plates *Struct. Heal. Monit.* **18** 690–714

[56] Monnier T, Dia S, Godin N and Zhang F 2012 Primary Calibration of Acoustic Emission Sensors by the Method of Reciprocity , Exploitation *J. Acoust. Emiss.* **30** 152–66

[57] Scheeren B, Kaminski M L and Pahlavan L 2023 Acoustic emission monitoring of naturally developed damage in large-scale low-speed roller bearings *Struct. Heal. Monit.*

[58] Alkhateeb S, Riccioli F, Morales F L and Pahlavan L 2022 Non-Contact Acoustic Emission Monitoring of Corrosion under Marine Growth *Sensors* **23** 161

[59] Nazmdar Shahri M, Yousefi J, Fotouhi M and Ahmadi Najfabadi M 2016 Damage evaluation of composite materials using acoustic emission features and Hilbert transform *J. Compos. Mater.* **50** 1897–907

[60] Alimirzaei S, Ahmadi Najafabadi M, Bani Mohammad Ali A and Pahlavan L 2024 Buckling assessment of GFRP and carbon fiber-reinforced plastic filament-wound tubes using an acoustic emission-based methodology *J. Reinf. Plast. Compos.* **43** 897–911

[61] Michał S, Szymon D, Paweł Z and Paweł S 2025 Damage characterisation of GFRP composites based on clustering acoustic emission events utilizing single-failure-cause tests as reference *Compos. Struct.* **351**

[62] Chen J, Hallett S and Wisnom M R 2010 Modelling complex geometry using solid finite element meshes with correct composite material orientations *Comput. Struct.* **88** 602–9

[63] Maljaars P J, Kaminski M L and den Besten J H 2017 Finite element modelling and model updating of small scale composite propellers *Compos. Struct.* **176** 154–63

[64] Anon 1988 IEEE Standard on Piezoelectricity *ANSI/IEEE Std 176-1987* 0_1-

[65] Gautschi G 2006 *Piezoelectric Sensorics: Force Strain Pressure Acceleration and Acoustic Emission Sensors Materials and Amplifiers* (Springer Berlin Heidelberg)

[66] Meggit 2017 Data for modelling

[67] Huijer A, Kassapoglou C and Pahlavan L 2021 Acoustic emission monitoring of carbon fibre reinforced composites with embedded sensors for in-situ damage identification *Sensors* **21**

[68] Huijer A 2019 *Load and damage measurements on fibre-reinforced composites with embedded piezoelectric sensors*

[69] Hexcel corporation 2016 HexPly 8552 Epoxy matrix (180C/356F curing matrix)

[70] Sala G, Olivier M, Bettini P and Sciacovelli D 2004 Embedded piezoelectric sensors and actuators for control of active composite structures *Mech. Therm. Eng. Dep. Carlo Gavazzi Sp. ESTEC, Eur. Sp. Agency*

[71] Anon 2014 Kyowa Strain Gages KFGS-5-120-C1-11

[72] Young W C, Budynas R G and Sadegh A M 2011 *Roark's Formulas for Stress and Strain, 8th Edition* (McGraw-Hill Education)

[73] Wheeler A J, Ganji A R and Krishnan V V 2010 *Introduction to engineering experimentation. LK - https://tudelft.on.worldcat.org/oclc/840427711* (Upper Saddle River SE - 480 blz. ; .. cm.: Pearson)

[74] de Bles W 2022 Dynamic response reconstruction of an FRC blade with embedded piezoelectric sensors

[75] Bretschneider, Herbert, Bosschers J, Hwan Choi G, Ciappi E, Farabee T, Kawakita C and Tang D 2014 Specialist committee on hydrodynamic noise." Final report and recommendations to the 27th ITTC. *Proc. 27th ITTC* **2** 639–79

[76] Anon User manual PICAS

[77] Zhang X, Huijer A, Kassapoglou C and Pahlavan L Influence of Embedding Piezoelectric Wafer Sensors on The Mechanical Behaviour of Composite Laminates *[Unpublished results]*

[78] Huntsman 2012 Araldite LY 5052 / Aradur 5052 COLD CURING EPOXY SYSTEMS

[79] Meggit 2019 Electronic correspondence with Karl Elkjaer [Personal communciation]

[80] Horowitz S B, Mathias A D, Fox J R, Cortes J P, Sanghadasa M and Ashley P 2012 Effects of scaling and geometry on the performance of piezoelectric microphones *Sensors Actuators, A Phys.* **185** 24–32

[81] Zhang L, Ozevin D, He D, Hardman W and Timmons A 2017 A Method to Decompose the Streamed Acoustic Emission Signals for Detecting Embedded Fatigue Crack Signals *Appl. Sci.* **8** 7

[82] Tani G, Viviani M, Felli M, Lafeber F H, Lloyd T, Aktas B, Atlar M, Turkmen S, Seol H, Hallander J and Sakamoto N 2020 Noise measurements of a cavitating propeller in different facilities: Results of the round robin test programme *Ocean Eng.* **213** 107599

[83] D6272-17 A 2017 *Standard Test Method for Flexural Properties of Unreinforced and Reinforced Plastics and Electrical Insulating Materials by Four-Point Bending*

[84] Ruan J, Michael Ho S C, Patil D, Li M and Song G 2014 Wind turbine blade damage detection using an active sensing approach *Smart Mater. Struct.* **23**

[85] Crawley E F and De Luis J 1987 Use of piezoelectric actuators as elements of intelligent structures *AIAA J.* **25** 1373–85

[86] Tuloup C, Harizi W, Aboura Z and Meyer Y 2020 Structural health monitoring of polymer-matrix composite using embedded piezoelectric ceramic transducers during several four-points bending tests *Smart Mater. Struct.* **29**

[87] Tzou H S and Tseng C I 1990 Distributed piezoelectric sensor/actuator design for dynamic measurement/control of distributed parameter systems: A piezoelectric finite element approach *J. Sound Vib.* **138** 17–34

[88] Paget C 2001 Active health monitoring of aerospace composite structures by embedded piezoceramic transducers 44

[89] Feng T, Bekas D and Ferri Aliabadi M H 2020 Active health monitoring of thick composite structures by embedded and surface-mounted piezo diagnostic layer *Sensors (Switzerland)* **20** 1–19

[90] Ferri Aliabadi M H and Khodaei Z S 2017 *Structural health monitoring for advanced composite structures* (World Scientific Publishing Co. Pte. Ltd.)

[91] Dziendzikowski M, Niedbala P, Kurnyta A, Kowalczyk K and Dragan K 2018 Structural health monitoring of a composite panel based on PZT sensors and a transfer impedance framework *Sensors (Switzerland)* **18**

[92] Sause M G R 2016 *In Situ Monitoring of Fiber-Reinforced Composites: Theory, Basic Concepts, Methods, and Applications*

[93] Kim H S, Ghoshal A, Chattopadhyay A and Prosser W H 2004 Development of embedded sensor models in composite laminates for structural health monitoring *J. Reinf. Plast. Compos.* **23** 1207–40

[94] Zappino E and Carrera E 2020 Advanced modeling of embedded piezo-electric transducers for the health-monitoring of layered structures *Int. J. Smart Nano Mater.* **11** 325–42

[95] Nanda N 2020 Spectral finite element method for wave propagation analysis in smart composite beams containing delamination *Aircr. Eng. Aerosp. Technol.* **92** 440–51

[96] Lin M and Chang F K 2002 The manufacture of composite structures with a built-in network of piezoceramics *Compos. Sci. Technol.* **62** 919–39

[97] Shukla D R and Vizzini A J 1996 Interlacing for improved performance of laminates with embedded devices *Smart Mater. Struct.* **5** 225–9

[98] Huang Y, Ghezzo F and Nemat-Nasser S 2009 Onset of resin micro-cracks in unidirectional glass fiber laminates with integrated SHM sensors: Numerical analysis *Struct. Heal. Monit.* **8** 493–507

[99] Ghezzo F, Starr A F and Smith D R 2010 Integration of networks of sensors and

electronics for structural health monitoring of composite materials *Adv. Civ. Eng.* **2010** 598458

[100] Xiao Y, Qiao W, Fukuda H and Hatta H 2016 The effect of embedded devices on structural integrity of composite laminates *Compos. Struct.* **153** 21–9

[101] Li L, Lomov S V., Yan X and Carvelli V 2014 Cluster analysis of acoustic emission signals for 2D and 3D woven glass/epoxy composites *Compos. Struct.* **116** 286–99

[102] Friedrich L, Colpo A, Maggi A, Becker T, Lacidogna G and Iturrioz I 2021 Damage process in glass fiber reinforced polymer specimens using acoustic emission technique with low frequency acquisition *Compos. Struct.* **256** 113105

[103] Saeedifar M and Zarouchas D 2020 Damage characterization of laminated composites using acoustic emission: A review *Compos. Part B Eng.* **195** 108039

[104] Kurz J H, Finck F, Grosse C U and Reinhardt H 2004 Similarity matrices as a new feature for acoustic emission analysis of concrete *Ewgae* 769–75

[105] Van Steen C, Pahlavan L, Wevers M and Verstrynge E 2019 Localisation and characterisation of corrosion damage in reinforced concrete by means of acoustic emission and X-ray computed tomography *Constr. Build. Mater.* **197** 21–9

[106] van Steen C 2019 Clustering of acoustic emission signals for fracture monitoring during accelerated corrosion of reinforced concrete prisms

[107] Trugman D T, Ross Z E and Johnson P A 2020 Imaging Stress and Faulting Complexity Through Earthquake Waveform Similarity *Geophys. Res. Lett.* **47** 1–8

[108] Akaike H 1974 Markovian representation of stochastic processes and its application to the analysis of autoregressive moving average processes *Ann. Inst. Stat. Math.* **26** 363–87

[109] Bai F, Gagar D, Foote P and Zhao Y 2017 Comparison of alternatives to amplitude thresholding for onset detection of acoustic emission signals *Mech. Syst. Signal Process.* **84** 717–30

[110] Scheeren B 2017 *On the Development of a Volumetric Acoustic Emission Fatigue Crack Monitoring System*

[111] MISTRAS 2015 R15I-AST Sensor **46** 252040

[112] Perls T A 1952 Electrical noise from instrument cables subjected to shock and vibration *J. Appl. Phys.* **23** 674–80

[113] International Maritime Organization 2023 2023 IMO Strategy on Reduction of GHG Emissions from Ships, Resolution MEPC.377(80) **4** 88–100

[114] International Maritime Organization 2014 Guidelines for the Reduction of Underwater Noise From Commercial Shipping to Address Adverse Impacts on Marine Life, MEPC.1/Circ.833 **44**

[115] Maung P T, Prusty B G, Donough M J, Oromiehie E, Phillips A W and St John N A 2023 Automated manufacture of optimised shape-adaptive compsite hydrofoils with curvilinear fibre paths for improved bend-twist performance *Mar. Struct.* **87** 103327

[116] Ng G W, Martins J R R A and Young Y L 2022 Optimizing steady and dynamic hydroelastic performance of composite foils with low-order models *Compos. Struct.* **301**

[117] Hussain M, Abdel-Nasser Y, Banawan A and Ahmed Y M 2021 Effect of hydrodynamic twisting moment on design and selection of flexible composite marine propellers *Ocean Eng.* **220** 108399

[118] Choi Y S, Joe B J, Jang W S, Hong S Y, Song J H and Kwon H W 2022 Numerical investigation of BPF noise for flexible submarine propeller design including inertial force coupling *J. Mar. Sci. Technol.* **27** 648–64

[119] Su Z, Pan J, Zhang S, Wu S, Yu Q and Zhang D 2022 Characterizing dynamic deformation of marine propeller blades with stroboscopic stereo digital image correlation *Mech. Syst. Signal Process.* **162**

[120] Shiraishi K, Sawada Y and Arakawa D 2023 Deformed shape estimation for flexible composite marine propellers by image registration *J. Mar. Sci. Technol.* **28** 221–33

[121] Kluczyk M, Grządziela A and Batur T 2022 Design and Operational Diagnostics of Marine Propellers Made of Polymer Materials *Polish Marit. Res.* **29** 115–22

[122] Huijer A, Zhang X, Kassapoglou C and Pahlavan L 2022 Feasibility evaluation for development of composite propellers with embedded piezoelectric sensors *Mar. Struct.* **84** 103231

[123] Alimirzaei S, Najafabadi M A and Khodaei A 2022 Characterization of The Damage Mechanism of Glass/Epoxy Composite Tubes Under Quasi-Static Axial Loading Using Acoustic Emission Monitoring *Appl. Compos. Mater.* **29** 1911–36

[124] Vidakovic M, Armakolas I, Sun T, Carlton J and Grattan K T V 2016 Fibre Bragg Grating-Based Acoustic Sensor Array for Improved Condition Monitoring of Marine Lifting Surfaces *J. Light. Technol.* **34** 4336–42

[125] Davies P, Dumergue N, Arhant M, Nicolas E, Paboeuf S and Mayorga P 2022 Material and structural testing to improve composite tidal turbine blade reliability *Int. Mar. Energy J.* **5** 57–65

[126] Pahlavan L, Mota M M and Blacquière G 2016 Influence of asphalt on fatigue crack monitoring in steel bridge decks using guided waves *Constr. Build. Mater.* **120** 593–604

[127] Gopalakrishnan S, Ruzzene M and Hanagud S 2011 *Computational Techniques for Structural Health Monitoring*

[128] LEMO SA 2018 High pressure connectors 03 series

[129] Vallen Systeme GMBH 2020 AMSY-6 Software Operation Manual

[130] Rose J L 2014 *Ultrasonic guided waves in solid media* vol 9781107048

[131] Karmazin A 2012 *Time-efficient Simulation of Surface-excited Guided Lamb Wave Propagation in Composites*

[132] Cai J, Yuan S, Qing X P, Chang F K, Shi L and Qiu L 2015 Linearly dispersive signal construction of Lamb waves with measured relative wavenumber curves *Sensors Actuators, A Phys.* **221** 41–52

[133] Pahlavan L 2012 *Wave Propagation in Thin-walled Composite Structures: Application to Structural Health Monitoring*

[134] Falcetelli F, Venturini N, Romero M B, Martinez M J, Pant S and Troiani E 2021 Broadband signal reconstruction for SHM: An experimental and numerical time reversal methodology *J. Intell. Mater. Syst. Struct.* **32** 1043–58

[135] Falcetelli F, Romero M B, Pant S, Troiani E and Martinez M 2018 Modelling of pencil-lead break acoustic emission sources using the time reversal technique *9th Eur. Work. Struct. Heal. Monit. EWSHM 2018*

[136] Park H W, Sohn H, Law K H and Farrar C R 2007 Time reversal active sensing for health monitoring of a composite plate *J. Sound Vib.* **302** 50–66

[137] Xu B, Yu L and Giurgiutiu V 2009 Lamb wave dispersion compensation in piezoelectric wafer active sensor phased-array applications *Heal. Monit. Struct. Biol. Syst. 2009* **7295** 729516

[138] Pahlavan L and Blacquière G 2016 Fatigue crack sizing in steel bridge decks using ultrasonic guided waves *NDT E Int.* **77** 49–62

[139] Wilcox P D 2003 A rapid signal processing technique to remove the effect of dispersion from guided wave signals *IEEE Trans. Ultrason. Ferroelectr. Freq. Control* **50** 419–27

[140] Hall J S and Michaels J E 2012 Adaptive dispersion compensation for guided wave imaging *AIP Conf. Proc.* **1430** 623–30

[141] Qiu J, Li F, Abbas S and Zhu Y 2019 A baseline-free damage detection approach based on distance compensation of guided waves *J. Low Freq. Noise Vib. Act. Control* **38** 1132–48

[142] Hassan F, Mahmood A K Bin, Yahya N, Saboor A, Abbas M Z, Khan Z and Rimsan M 2021 State-of-the-Art Review on the Acoustic Emission Source Localization Techniques *IEEE Access* **9** 101246–66

[143] Cai J, Shi L and Qing X P 2013 Erratum: A time-distance domain transform method for Lamb wave dispersion compensation considering signal waveform correction (Smart Materials and Structures (2013) 22) *Smart Mater. Struct.* **22**

[144] Cai J, Wang X and Zhou Z 2019 A signal domain transform method for spatial resolution improvement of Lamb wave signals with synthetically measured relative wavenumber curves *Struct. Heal. Monit.* **18** 1633–51

[145] Wilcox P 2005 Application of guided wave signal processing to acoustic emission data *AIP Conference Proceedings* vol 760 pp 1809–16

[146] Jiao J, He C, Wu B and Fei R 2004 A new technique for modal acoustic emission pipeline leak location with one sensor *Insight Non-Destructive Test. Cond. Monit.* **46** 392–5

[147] De Marchi L, Marzani A, Speciale N and Viola E 2011 A passive monitoring technique based on dispersion compensation to locate impacts in plate-like structures *Smart Mater. Struct.* **20**

[148] Grabowski K, Gawronski M, Baran I, Spychalski W, Staszewski W J, Uhl T, Kundu T and Packo P 2016 Time-distance domain transformation for Acoustic Emission source localization in thin metallic plates *Ultrasonics* **68** 142–9

[149] Xu K, Ta D, Moilanen P and Wang W 2012 Mode separation of Lamb waves based on dispersion compensation method *J. Acoust. Soc. Am.* **131** 2714–22

[150] Wu W and Wang Y 2019 A Simplified Dispersion Compensation Algorithm for the Interpretation of Guided Wave Signals *J. Press. Vessel Technol. Trans. ASME* **141**

[151] Palacz M 2018 Spectral methods for modelling ofwave propagation in structures in terms of damage detection-A review *Appl. Sci.* **8** 1124

[152] Kim Y, Ha S and Chang F K 2008 Time-domain spectral element method for built-in piezoelectric-actuator- induced lamb wave propagation analysis *AIAA J.* **46** 591–600

[153] Zaal A 2021 Feasibility evaluation of a non- tures using ultrasonic guided rial properties of FRC struc- destructive estimation of mate- waves 6

[154] Samaitis V and Mažeika L 2017 Influence of the spatial dimensions of ultrasonic transducers on the frequency spectrum of guided waves *Sensors (Switzerland)* **17**

[155] Patsantzopoulos G Fatigue Assessment of Composite Propellers

CURRICULUM VITAE

Personal Data

Place and date of birth:	Hendrik-Ido-Ambacht, the Netherlands, 03-03-1995

Prior Education

July 2013	Diploma in pre-university education (VWO)
	Utrechts Stedelijk Gymnasium
August 2014	Propaedeutics in Marine Technology
	Delft University of Technology
August 2016	Bachelor of Science in Marine Technology
	Delft University of Technology
November 2019	Master of Science in Marine Technology
	Delft University of Technology

Work Experience

Summers 2014-2017	Intern/Summer job at Oceanco Yachts
January 2018	Student assistant at Delft University of Technology
Feb 2020-Oct 2020	Junior researcher at Delft University of Technology
Nov 2020-Jan 2025	PhD candidate at Delft University of Technology
Jun 2024-Dec 2024	Technical consultant at Sinteg Systems b.v.
Jan 2025-present	Researcher at Delft University of Technology

Scientific Publications

Journal papers:

Huijer A, Kassapoglou C, Pahlavan L 2021 Acoustic emission monitoring of carbon fibre reinforced composites with embedded sensors for in-situ damage identification *Sensors (Switzerland)*

Huijer A, Zhang X, Kassapoglou C, Pahlavan L 2022 Feasibility evaluation for development of composite propellers with embedded piezoelectric sensors *Marine Structures*

Riccioli F, Huijer A, Grasso N, Rizzo C, Pahlavan L 2023 Development of a retrofit layer with an embedded array of piezoelectric sensors for transient pressure measurement in maritime applications *Marine Structures*

Adams M, Huijer A, Kassapoglou C, Vaders J, Pahlavan L 2024 In situ non-destructive stiffness assessment of fibre reinforced composite plates using ultrasonic guided waves *Sensors (Switzerland)*

Huijer A, Kassapoglou C, Pahlavan L 2024 Acoustic emission monitoring of composite marine propellers in submerged conditions using embedded piezoelectric sensors *Smart Materials and Structures*

Conference papers

Huijer A, Kassapoglou C, Pahlavan L 2022 Numerical and experimental study of acoustic emission source signal reconstruction in fibre-reinforced composite panels *European Workshop on Structural Health Monitoring 2022*

Huijer A, Kassapoglou C, Pahlavan L 2023 Acoustic emission source localisation in fibre-reinforced composites based on multimodal dispersion compensation of guided waves *International Workshop on Structural Health Monitoring 2023*

Huijer A, Kassapoglou C, Pahlavan L 2024 Acoustic emission monitoring of composite marine propeller blades using embedded piezoelectric sensors and hydrophones *European Workshop on Structural Health Monitoring 2024*